UC Riverside
UC Riverside Electronic Theses and Dissertations

Title
Computational Insights into Porous Materials for Gas Separation

Permalink
https://escholarship.org/uc/item/7bs349kc

Author
Wang, Song

Publication Date
2020

Peer reviewed|Thesis/dissertation

eScholarship.org Powered by the California Digital Library
University of California

UNIVERSITY OF CALIFORNIA
RIVERSIDE

Computational Insights into Porous Materials for Gas Separation

A Dissertation submitted in partial satisfaction
of the requirements for the degree of

Doctor of Philosophy

in

Chemistry

by

Song Wang

June 2020

Dissertation Committee:

Dr. De-en Jiang, Chairperson
Dr. Gregory Beran
Dr. Leonard Mueller

Copyright by
Song Wang
2020

The Dissertation of Song Wang is approved:

Committee Chairperson

University of California, Riverside

COPYRIGHT ACKNOWLEDGEMENT

The text and figures in Chapter 3, in part or full, are reproduced from "Optimal Size of a Cylindrical Pore for Post-Combustion CO_2 Capture", *J Phys. Chem. C* 2017, *121* (40), 22025-22030. The coauthor (Dr. De-en Jiang) directed and supervised this research.

The text and figures in Chapter 4, in part or full, are reproduced from "Effect of Pore Density on Gas Permeation through Nanoporous Graphene Membranes", *Nanoscale* 2018, *10* (30), 14660-14666. The coauthor (Dr. De-en Jiang) directed and supervised this research.

The text and figures in Chapter 5, in part or full, are reproduced from "Continuously Tunable Pore Size for Gas Separation via A Bilayer Nanoporous Graphene Membrane", *ACS Appl. Nano Mater.* 2018, *2* (1), 379-384. The coauthor (Dr. De-en Jiang) directed and supervised this research.

The text and figures in Chapter 6, in part or full, are reproduced from "Entropic Selectivity in Air Separation via a Bilayer Nanoporous Graphene Membrane", *Phys. Chem. Chem. Phys.* 2019, *21* (29), 16310-16315. The coauthor (Dr. De-en Jiang) directed and supervised this research.

The text and figures in Chapter 8, in part or full, are reproduced from "Insights into CO_2/N_2 Selectivity in Porous Carbons from Deep Learning", *ACS Mater. Lett.* 2019, *1* (5), 558-563. The coauthor (Dr. De-en Jiang) directed and supervised this research.

The text and figures in Chapter 9, in part or full, are reproduced from "Prediction of CO_2/N_2 Selectivity in Porous Carbons from N_2 Adsorption Isotherm at 77 K via Convolutional Neural Networks", invited manuscript to *Angew. Chem.* 2020. The coauthor (Dr. De-en Jiang) directed and supervised this research.

ACKNOWLEDGEMENTS

First of all, I would like to thank my research advisor Dr. De-en Jiang for his support and helpful guidance during my Ph.D. career. He is not only a responsible supervisor, but also a good friend. I have a great time during many group activities, including weekly coffee break, parties, and group travel in cruise to Mexico.

I would also like to thank my dissertation committee members Dr. Gregory Beran and Dr. Leonard Mueller and oral qualifying exam committee members Dr. Haofei Zhang and Dr. Bryan M. Wong, for their useful comments and suggestions.

Then, I thank my research collaborators: Dr. Sheng Dai, Dr. Zhenzhen Yang, and Dr. Hao Chen at the University of Tennessee Knoxville for 2D porous membrane study, Dr. Zihao Zhang at the University of Tennessee Knoxville for suggestions of machine learning works. I also thank all my group colleagues, especially Dr. Ziqi Tian and Dr. Bo Li, for their help in solving many problems in my research.

Finally, I am highly grateful to my wife Jiemin Zhao, for her permanent accompany, her excellent care, and strong support of my research. We will support each other in the future career and life.

This work was supported by the U.S. Department of Energy, Office of Science, Office of Basic Energy Sciences, Chemical Sciences, Geosciences, and Biosciences Division. This research used resources of the National Energy Research Scientific

Computing Center, a DOE Office of Science User Facility supported by the Office of Science of the U.S. Department of Energy under Contract No. DE-AC02-05CH11231.

ABSTRACT OF THE DISSERTATION

Computational Insights into Porous Materials for Gas Separation

by

Song Wang

Doctor of Philosophy, Graduate Program in Chemistry
University of California, Riverside, June 2020
Dr. De-en Jiang, Chairperson

Membrane-based materials are an important branch in the field of gas separation. There are increasing number of membrane materials which are synthesized in recent years. Among them, the novel ultrathin membranes with uniform pores like nanoporous graphene attracted attention of many researchers, because their excellent gas separation ability based on molecular sieving effect. Several factors might influence the performance of ultrathin membranes, including pore size, pore shape, pore density, etc. However, the theoretical understanding of these factors has not been clearly addressed. In this dissertation, we firstly investigated the optimal pore size by first-principles density functional theory and simulated the pore-size effect for post-combustion carbon capture by grand canonical Monte Carlo. Next, we used molecular dynamics simulations to study the effect of pore density on the nanoporous graphene membrane. Then, we proposed a bilayer design of

nanoporous graphene membrane with continuously tunable effective pore size for gas separations, such as CO_2/CH_4, N_2/CH_4, O_2/N_2. Meanwhile, we studied the effect of entropic selectivity by tracking the trajectories of gas-permeance events. After that, we proposed other design of graphene/ionic-liquid composites with tunable slit pore size. Finally, to satisfy the requirement of exploring huge material database for gas separation, we applied machine learning to predict the selectivity of porous carbon materials. We further used convolutional neural networks to search the optimal porous carbon material from an ultimate input feature. The same approach was also used for prediction of hydrogen locations in copper clusters, which are potential materials for hydrogen storage. The works in this dissertation aims to find and design ultrathin nanoporous materials for gas separation by different computational approaches.

Table of Contents

List of Tables

List of Figures

Chapter 1. Introduction

1.1 Basics of gas separation

Separation is a process that converts a mixture or solution of chemical substances into two or more distinct product mixtures or fully divide the mixture into pure constituents. How to separate chemical mixtures into pure or purer forms is the goal of many industrial chemists. About 10-15% of the world's energy consumption comes from separation process. If the US petroleum, chemical and paper manufacturing factories use more energy efficient separation methods, they will save 100 million tonnes of CO_2 emissions and $4 billion per year in energy costs.[1]

Nowadays, there are nine major separation technologies: distillation, evaporation, drying, extraction, absorption, adsorption, membrane, crystallization, and physical property-based operations (such as floatation and screening) (Figure 1-1). The first three methods are the most widely used in industry, which respectively account for 49%, 20%, and 11% of the industrial separations energy consumption.[2] The rest methods are energy efficient separation methods, which could lower global energy usage, greenhouse gases emissions, and environment pollution.

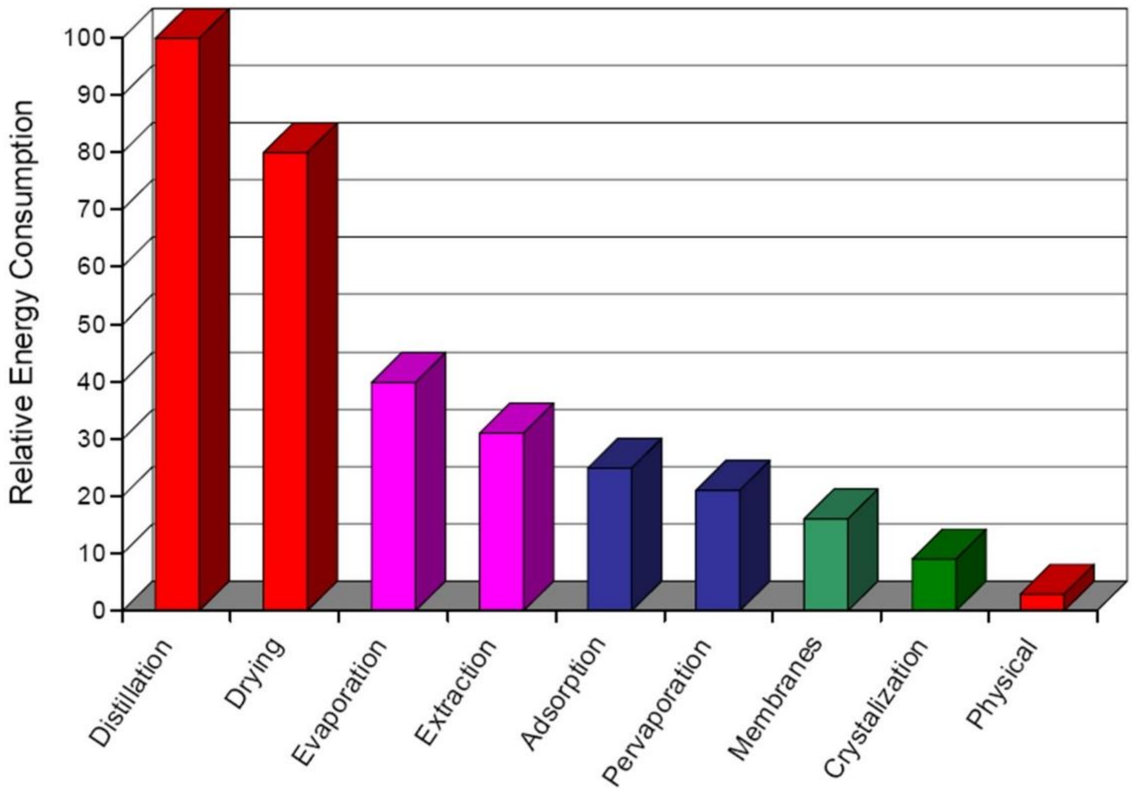

Figure 1-1. Relative energy use by various separation technologies.[2]

Gas separation is an important branch of chemical separation, including air separation, natural gas purification, hydrogen production, carbon dioxide capture, and et al. Air separation is a process that mainly divides air into nitrogen and oxygen. Pure nitrogen and oxygen both have many applications in medical, chemical, and industrial aspects. Natural gas purification is a process that remove water, carbon dioxide, and hydrogen sulfide from raw natural gas. Natural gas is already one of the most important energy resources for power generation, domestic use, transportation, and so on. Hydrogen production is the method for generating hydrogen gas. Nearly 95% hydrogen is produced from fossil fuels by steam reforming of natural gas, partial oxidation of methane, and coal gasification.[3] So, before use of hydrogen, rest components such as water, methane, carbon oxide, and carbon dioxide have to be removed. Carbon capture and storage (CCS) is the process for reducing CO_2 emission from burning fossil fuels and weakening the greenhouse effect.[4,5] There are mainly three different CO_2 capture approaches: post-combustion, pre-combustion, and oxyfuel combustion. In post-combustion approach, CO_2 is removed from flue gas after fossil fuel combustion.[6] In pre-combustion approach, fossil fuel is partially oxidized and transferred into H_2 and CO_2, which is easy to be captured from a relatively pure exhaust stream.[7] In oxyfuel combustion approach, pure oxygen instead of air is used to react with fossil fuel. After condensation of water vapor through cooling, the flue gas is almost pure CO_2.[8] Among above three capture approaches, post-combustion carbon capture is most popular in research because it is most easily compatible with existing fossil fuel power plants.

1.2 Gas separation technologies and materials

Besides traditional distillation method, which is based on different boiling point of gases, there are two common types of extensively studied gas separation technology, which are separately based on sorbents and membranes.

1.2.1 Sorbent-based separation technology

Sorbent-based separation technology uses solid or liquid sorbents for gas capture and storage. Common sorbent materials include but not limit to zeolites, metal organic frameworks (MOFs), porous carbons, porous organic polymers (POPs), polymeric materials, et al.[9-12] According to the binding energy, adsorption process is classified as chemisorption and physisorption.[13] In chemical adsorption, gas molecules are bound to the sorbents by covalent bond. In physical adsorption, gas molecules are bound to the sorbents by weak van der Waals forces or electrostatic attraction.

Gas adsorption process has two popular models (mechanisms): monolayer model (Langmuir theory) and multilayer model (Brunauer–Emmett–Teller (BET) theory). The former was proposed by Langmuir in 1918,[14] which is the most common adsorption theory because of its simplicity and its ability to fit a variety of adsorption data. This theory assumes that only a monolayer is formed on the sorbent surface at the maximum adsorption. Langmuir theory gives us an adsorption expression:

$$\frac{1}{v} = \frac{1}{Kv_{mon}} \cdot \frac{1}{P} + \frac{1}{v_{mon}}$$

where v is volume of adsorbate, v_{mon} is volume of adsorbate required to form a monolayer on the adsorbent, K is adsorption-desorption equilibrium constant, P is partial pressure of the gas. In 1938, Stephen Brunauer, Paul Emmett, and Edward Teller developed a new model for multilayers adsorption.[15] The adsorption expression was also modified as follow:

$$\frac{1}{v(1-x)} = \frac{1}{v_{mon}c} + \frac{x(c-1)}{v_{mon}c}$$

where x is the pressure divided by vapor pressure ($x = P/P_0$), c is equilibrium constant multiplied by vapor pressure ($x = K \cdot P$).

1.2.2 Membrane-based separation technology

Membrane materials include polymers, carbon molecular sieves (CMS), MOFs, perovskites, etc.[16-18] The solution-diffusion mechanism is the most widely used theory for gas separation through polymeric and liquid membrane.[19] There are three steps in this mechanism: a) gas molecule adsorbs onto the feed side of membrane; b) gas molecule diffuses through the membrane; c) gas molecule desorbs from the permeate side of membrane. According to this mechanism, the permeability (P) is a product of diffusivity (D) and solubility (S), expressed by: $P = D \cdot S$. There is a trade-off between selectivity and permeability called Robeson upper bound (Figure 1-2a),[20-22] which can be shown by following equation:

$$\alpha_{i,j} = P_i/P_j = \beta_{i,j} \cdot P_i^{-\lambda_{i,j}}$$

where P_i and P_j are permeabilities, $\alpha_{i,j}$ is selectivity, $\beta_{i,j}$ and $\lambda_{i,j}$ are parameters depending on the gas pair. $\lambda_{i,j}$ can be calculated by the ratio of gas molecule size:

$$\lambda_{i,j} = (d_j/d_i)^2 - 1$$

where d_i and d_j are the kinetic diameters of larger and smaller gas molecules. $\beta_{i,j}$ is relevant to $\lambda_{i,j}$, gas solubility, and average distance between polymer chains and chain stiffness.

Although the trade-off constrains the separation performance of membrane materials, people also often use permeance to describe membrane productivity. Because permeance is equal to permeability divided by membrane thickness, if the permeability is a constant, when the thickness decreases, the permeance will increases. Therefore, ultrathin membranes even one-atom-thin membranes will have the highest permeance. If they also possess a serial of nanoscale pores with uniform size between the kinetic diameters of the gas pair, they can achieve high selectivity by molecular-sieving separation process at the same time.[23]

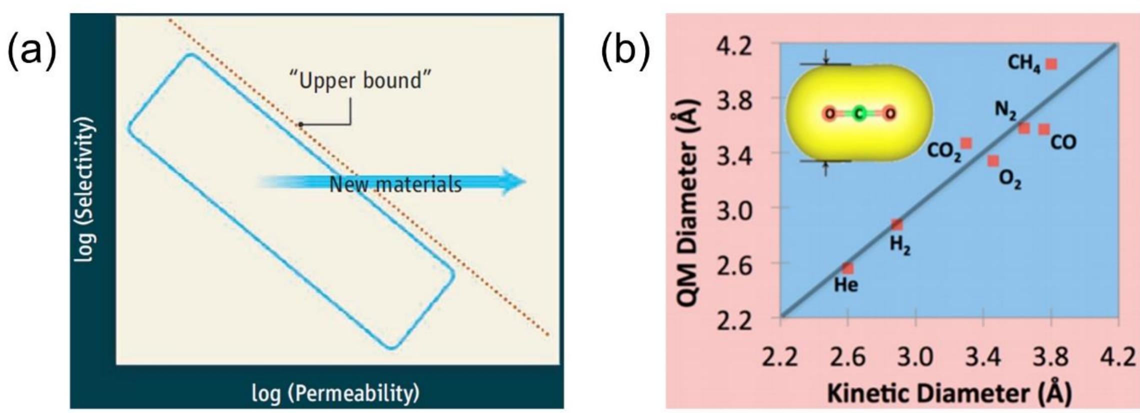

Figure 1-2. Robeson upper bound and molecular diameters. (a) The trade-off between selectivity and permeability called Robeson upper bound.[22] (b) Comparation between the QM diameters with the experimental kinetic diameters.[24]

From above introduction, we can know that, for membrane-based separation technology, kinetic diameter of gas molecules is an essential parameter. It can be determined by quantum mechanical (QM) calculation. Figure 1-2b shows the QM diameter values calculated by the iso-electronic density surfaces and compares the QM diameters with the experimental kinetic diameters.[24]

1.3 Recent theoretical research on ultrathin membranes for gas separation

1.3.1 Porous graphene

Graphene is a two-dimensional sheet of sp2-hybridized carbon atoms with hexagonal lattice, named by Hanns-Peter Boehm, who originally observed graphene in electron microscopes in 1962.[25] But the breakthrough discovery occurred in 2004 by Andre Geim and Konstantin Novoselov, who rediscovered, isolated, and characterized graphene.[26] They won Nobel Prize in Physics in 2010 for this work. There are increasing numbers of research on graphene because of its excellent chemical stability, unique electrical conductivity, and great potential applications, including catalysis, electronics, and energy storage.[27] The global market for graphene will reach $151.4 million by 2021.[28] However, the perfect graphene sheet is impermeable to any gas molecules. To use it for gas separation, people have to introduce sub-nanometer pores into the pristine graphene sheet. In 2009, Dr. Jiang and coworkers firstly proposed the porous graphene for gas separation in theoretical study.[29] They designed two types of pore shown in Figure 1-3 and calculated interaction energy between H_2 or CH_4 and the porous graphene to estimate the high H_2/CH_4 selectivity. Three years later, the porous graphene was produced in experiment by using ultraviolet-induced oxidative etching technology and showed great gas separation ability.[30]

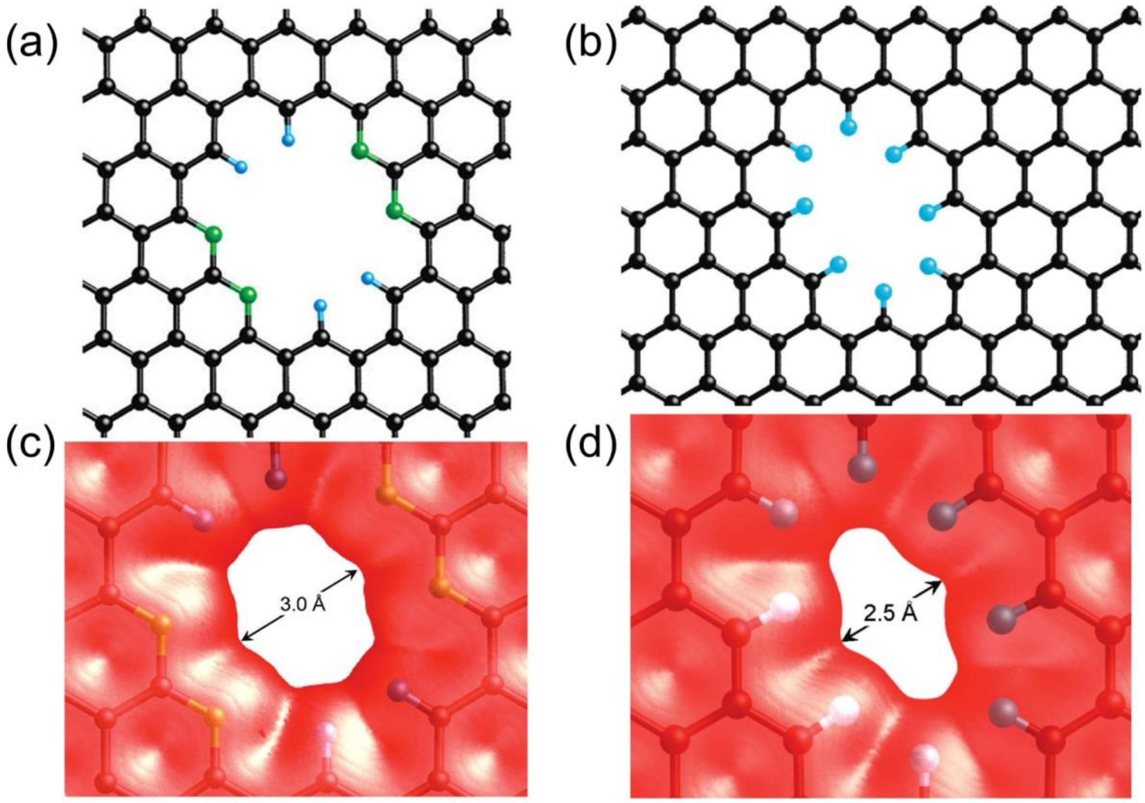

Figure 1-3. Two types of nanopores in graphene sheet. (a) all-hydrogen saturated pore; (b) nitrogen-functionalized pore. (c) and (d) are their electron density isosurface.[29]

Later on, several works further studied the permeance and selectivity of more gas molecules by classical molecular dynamics (CMD).[31-33] Figure 1-4a shows the simulation model, which is divided into two chambers by the porous graphene membrane. Gas molecules are allowed to permeate from high pressure chamber (feed side) to the vacuum chamber (permeate side). Figure 1-4b shows the H_2 permeance at different feed pressures.[31]

Similarly, the result of CO_2 and N_2 permeation through nitrogen-functionalized nanopore (4N4H) are shown in Figure 1-4c.[32] With an initial pressure of 10 atom, CO_2 permeance reached to 2.9×10^5 GPU (1 GPU = 3.35×10^{-10} $mol\cdot m^{-2}\cdot s^{-1}\cdot Pa^{-1}$) and nearly no N_2 molecule can pass through the pore. Then, various gas molecules were simulated and the trend of permeate flux is that $H_2 > CO_2 > \ > N_2 > Ar > CH_4$, generally agreement the sequence of their kinetic diameters.[33]

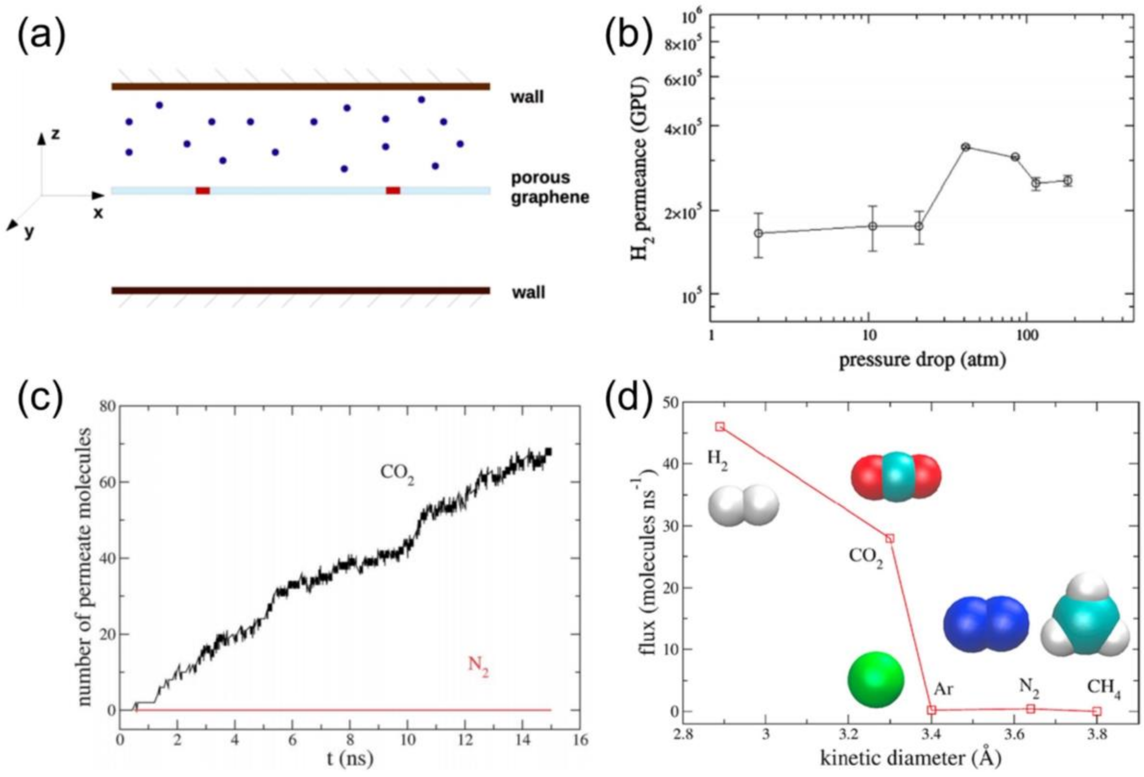

Figure 1-4. Examples of CMD simulations for gas separation. (a) The bi-chamber simulation model.[31] (b) H_2 permeance through the porous graphene at different pressure.[31] (c) CO_2 and N_2 permeation through nitrogen-functionalized nanopore (4N4H).[32] (d) Fluxes of several gas molecules through 4N4H nanoporous graphene by CMD simulations.[33]

Because precisely control the pore size down to 3-5 Å is difficult in experiment, and larger pore size could significantly decrease the permeability selectivity, how to utilize nonselective large pores for gas separation is a challenge. A strategy proposed in 2017 applied a composite membrane comprising a monolayer (less than 5 Å) of ionic liquid-coated porous graphene with pore diameter of 6.0 Å (Figure 1-5a).[34] The [emim][BF4] ionic liquid was chosen because of its wettability on graphene.[35]

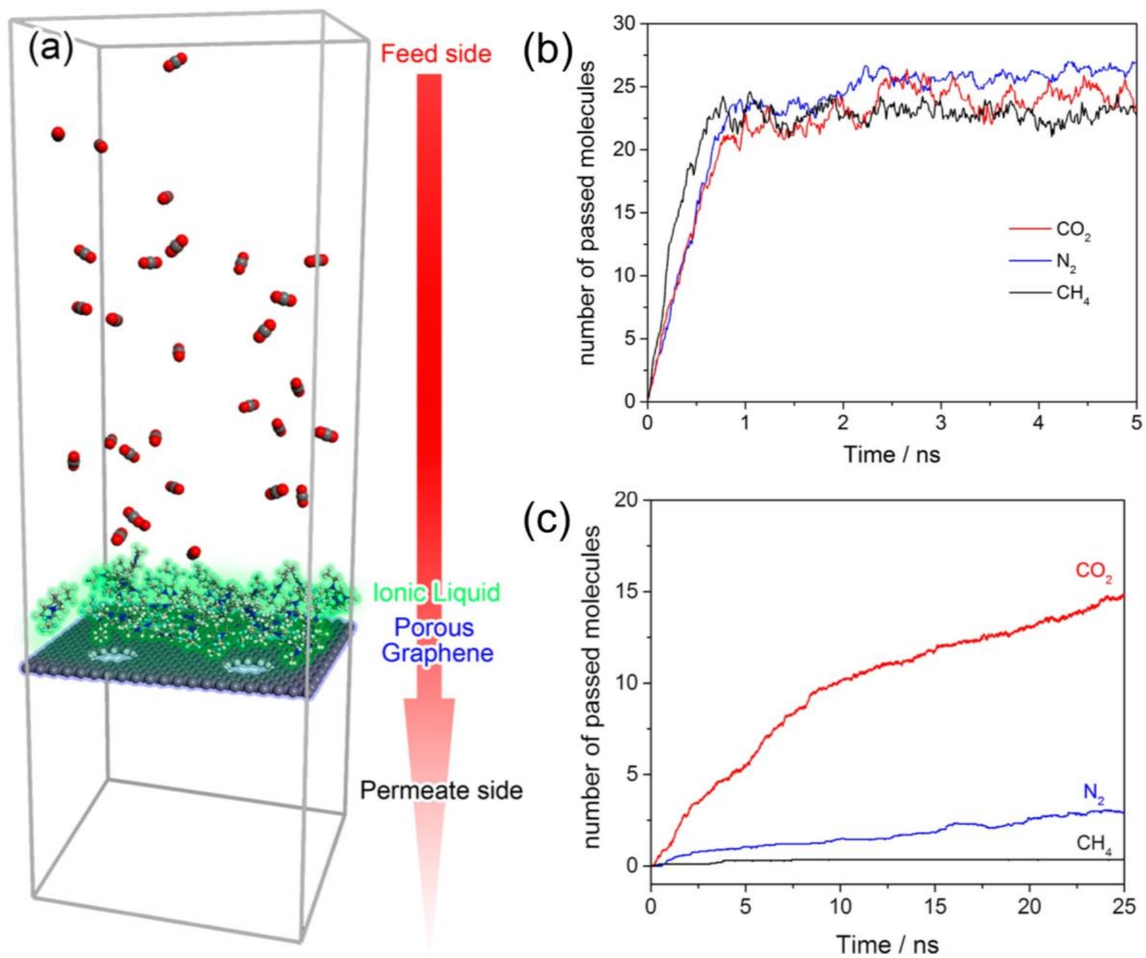

Figure 1-5. Porous graphene with one IL layer. (a) The simulation model of gas permeance through the porous graphene with one IL layer. Pure gas permeation through porous graphene membrane (b) without and (c) with IL layer.[34]

Because the pore size is much greater than the kinetic diameters of CO_2 (3.30 Å), N_2 (3.64 Å), and CH_4 (3.80 Å), without the IL layer, all three gases could pass through the porous graphene membrane without any hindrance and achieve equilibriums quickly (Figure 1-5b). However, with the IL layer, one can see that the membrane is highly selective for CO_2 permeation, while CH_4 permeation is reduced the most (Figure 1-5c). Based on linear regression, a high CO_2 permeance value of 1.39×10^5 GPU and an impressive pure-gas selectivity of 42 for CO_2/CH_4 are achieved.[34]

1.3.2 Porous carbon nanotube

Carbon nanotube is another allotrope of carbon, intermediate between fullerene and graphene. Naturally, the idea of rolling porous graphene into porous carbon nanotube for gas separation was came up with. Figure 1-6 shows a model containing two coaxial single-wall carbon nanotubes.[36] There are several 4N4H pores on the inner nanotube. Initially, the gas molecules are inside the inner nanotube. Then, they are allowed to pass through the pores and enter the interspace between two nanotubes. By CMD simulations, Figure 1-6c shows the number of permeate gas molecules. One can see that no CH_4 molecule can cross through the pore, resulting in high CO_2/CH_4 selectivity. Similar studies have also been done for estimate the H_2/CH_4 selectivity of porous carbon nanotubes.[37]

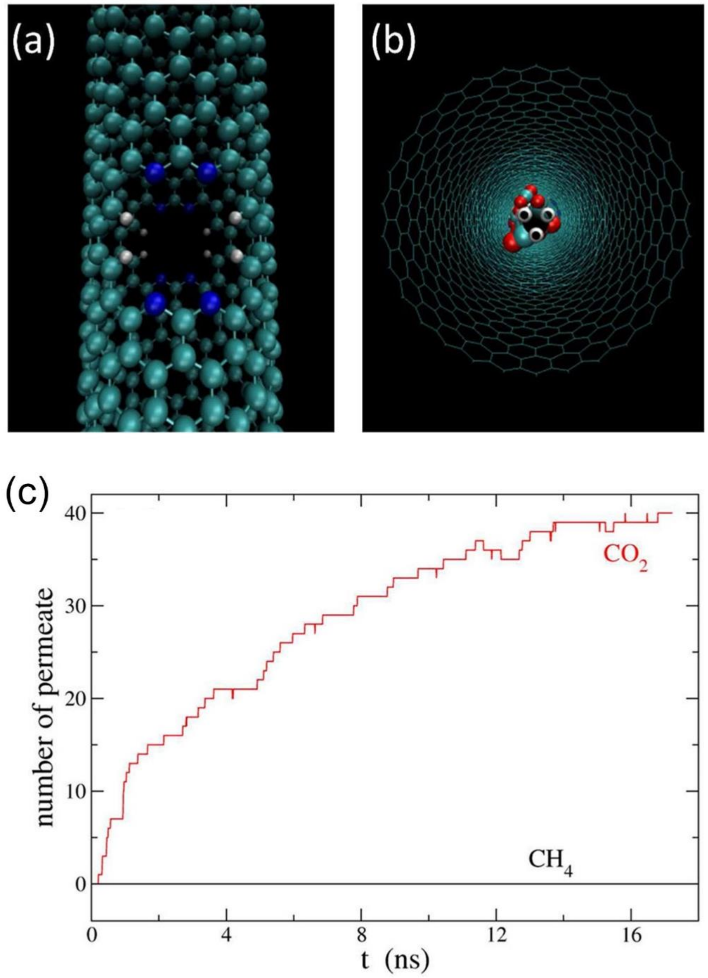

Figure 1-6. Porous carbon nanotube. (a) 4N4H pore on the carbon nanotube wall. (b) initial configuration of CMD simulation. (c) number of permeate molecules with time.[36]

1.3.3 2D organic membrane

Beside porous graphene and porous carbon nanotube, which use the top-down approach to obtain the pore, there is another pathway called bottom-up approach. Many 2D organic membranes natively have pores in nanoscale. With suitable design, the pore size could fit the separation requirement of target gas pairs.

The poly-phenylene membrane, as one of graphene-derived 2D membranes, was explored by Zhou et al.[38] Its native pore with a width of 2.48 Å, which is close to the kinetic diameter of H_2 and much less than the size of CO_2, CO, and CH_4. So, this membrane was expected to have high selective H_2 permeability for hydrogen purification application. Graphyne and graphdiyne are also graphene derivatives.[39] The pore size of the later is about 3.8 Å, which is between the diameters of H_2 and CH_4. So, it is also an ideal choice for H_2 separation.[40,41]

Graphene oxide is obtained by treating graphite with strong oxidizer. The ultrathin porous graphene oxide usually has a few layers. Both pores and interlayer channels have effect of gas separation. Besides carbon atom, graphene oxide might also include oxygen, nitrogen, and hydrogen. These functional groups also influence the gas mixture selectivity.[42,43]

The number of 2D porous organic polymers is increasing. Their structures usually include a serial of phenyl rings linked by various planar groups like ethenyl, phenyl, biphenyl, etc.[44-46] The length of these linker groups controls the pore size of final structures. And the pore size determines the membranes will be used for which gas pair systems and what the selectivity will be. Porphyrin derivatives are another class of 2D porous materials, which have been studied for CO_2/N_2 separation by computation study.[47]

1.4 Scientific questions in computational aspect

Although many works have been done, there are still some challenges in using membranes especially ultrathin membranes for gas separation. Here, we list four of them: 1) First challenge is how to precisely control the pore size. In experiment, pore size of membrane by top-down approach is too large to have high selectivity. 2) The second challenge is how to continuously tune the pore size, because for both experiment and simulation studies, the molecular construction forms the pore that varies non-continuously. 3) The third challenge is how to separate adsorption and diffusion selectivities. The permselectivity is the combination of adsorption selectivity and diffusion selectivity. Finding the contribution of both of selectivities is a challenge. 4) The last challenge is how to handle the increasing number of new membrane materials. Traditional simulation methods like DFT and CMD are always time-consuming to screen the huge material databases and pick out the required materials for required purpose. And they have poor ability to quickly make prediction and explore the unknown materials space.

In view of the above challenges, this dissertation presents our several works related to the effects of pore size and pore density, the new methods of continuously tuning pore size, the applications of entropy selectivity mechanism, and the applications of machine learning on prediction and screening materials space.

References

(1) Sholl, D. S.; Lively, R. P. Seven chemical separations to change the world. *Nature* **2016**, *532*, 435-437.

(2) BCS, I., and Oak Ridge National Laboratory Materials for separation technologies: Energy and emission reduction opportunities. Report prepared for the u.S. Doe, industrial technologies program. **2005**.

(3) Liu, K.; Song, C.; Subramani, V. *Hydrogen and syngas production and purification technologies*; John Wiley & Sons, 2010.

(4) D'Alessandro, D. M.; Smit, B.; Long, J. R. Carbon dioxide capture: Prospects for new materials. *Angew. Chem. Int. Ed.* **2010**, *49*, 6058-6082.

(5) Zhang, X.; Zhang, X.; Dong, H.; Zhao, Z.; Zhang, S.; Huang, Y. Carbon capture with ionic liquids: Overview and progress. *Energ. Environ. Sci.* **2012**, *5*, 6668-6681.

(6) Samanta, A.; Zhao, A.; Shimizu, G. K.; Sarkar, P.; Gupta, R. Post-combustion CO_2 capture using solid sorbents: A review. *Ind. Eng. Chem. Res.* **2012**, *51*, 1438-1463.

(7) Theo, W. L.; Lim, J. S.; Hashim, H.; Mustaffa, A. A.; Ho, W. S. Review of pre-combustion capture and ionic liquid in carbon capture and storage. *Appl. Energy* **2016**, *183*, 1633-1663.

(8) Habib, M.; Badr, H.; Ahmed, S.; Ben-Mansour, R.; Mezghani, K.; Imashuku, S.; la O', G.; Shao-Horn, Y.; Mancini, N.; Mitsos, A. A review of recent developments in carbon capture utilizing oxy-fuel combustion in conventional and ion transport membrane systems. *Int. J. Energ. Res.* **2011**, *35*, 741-764.

(9) Choi, S.; Drese, J. H.; Jones, C. W. Adsorbent materials for carbon dioxide capture from large anthropogenic point sources. *Chemsuschem* **2009**, *2*, 796-854.

(10) Sumida, K.; Rogow, D. L.; Mason, J. A.; McDonald, T. M.; Bloch, E. D.; Herm, Z. R.; Bae, T.-H.; Long, J. R. Carbon dioxide capture in metal–organic frameworks. *Chem. Rev.* **2012**, *112*, 724-781.

(11) Zeng, Y.; Zou, R.; Zhao, Y. Covalent organic frameworks for CO_2 capture. *Adv. Mater.* **2016**, *28*, 2855-2873.

(12) Wang, W.; Zhou, M.; Yuan, D. Carbon dioxide capture in amorphous porous organic polymers. *J. Mater. Chem. A* **2017**, *5*, 1334-1347.

(13) Haszeldine, R. S. Carbon capture and storage: How green can black be? *Science* **2009**, *325*, 1647-1652.

(14) Langmuir, I. The adsorption of gases on plane surfaces of glass, mica and platinum. *J. Am. Chem. Soc.* **1918**, *40*, 1361-1403.

(15) Brunauer, S.; Emmett, P. H.; Teller, E. Adsorption of gases in multimolecular layers. *J. Am. Chem. Soc.* **1938**, *60*, 309-319.

(16) Yong, W. F.; Li, F. Y.; Xiao, Y. C.; Chung, T. S.; Tong, Y. W. High performance pim-1/matrimid hollow fiber membranes for CO_2/CH_4, O_2/N_2 and CO_2/N_2 separation. *J. Membr. Sci.* **2013**, *443*, 156-169.

(17) Reid, C.; O'koy, I.; Thomas, K. Adsorption of gases on carbon molecular sieves used for air separation. Spherical adsorptives as probes for kinetic selectivity. *Langmuir* **1998**, *14*, 2415-2425.

(18) Koros, W. J.; Zhang, C. Materials for next-generation molecularly selective synthetic membranes. *Nature materials* **2017**, *16*, 289-297.

(19) George, S. C.; Thomas, S. Transport phenomena through polymeric systems. *Prog. Polym. Sci.* **2001**, *26*, 985-1017.

(20) Robeson, L. M. The upper bound revisited. *J. Membr. Sci.* **2008**, *320*, 390-400.

(21) Park, H. B.; Kamcev, J.; Robeson, L. M.; Elimelech, M.; Freeman, B. D. Maximizing the right stuff: The trade-off between membrane permeability and selectivity. *Science* **2017**, *356*, eaab0530.

(22) Gin, D. L.; Noble, R. D. Designing the next generation of chemical separation membranes. *Science* **2011**, *332*, 674-676.

(23) Tian, Z.; Dai, S.; Jiang, D. e. What can molecular simulation do for global warming? *WIRES Comput. Mol. Sci.* **2016**, *6*, 173-197.

(24) Mehio, N.; Dai, S.; Jiang, D.-e. Quantum mechanical basis for kinetic diameters of small gaseous molecules. *J. Phys. Chem. A* **2014**, *118*, 1150-1154.

(25) Boehm, H.-P.; Clauss, A.; Fischer, G.; Hofmann, U. Das adsorptionsverhalten sehr dünner kohlenstoff-folien. *Z. Anorg. Allg. Chem.* **1962**, *316*, 119-127.

(26) Novoselov, K. S.; Geim, A. K.; Morozov, S. V.; Jiang, D.; Zhang, Y.; Dubonos, S. V.; Grigorieva, I. V.; Firsov, A. A. Electric field effect in atomically thin carbon films. *Science* **2004**, *306*, 666-669.

(27) Mahmood, N.; Zhang, C.; Yin, H.; Hou, Y. Graphene-based nanocomposites for energy storage and conversion in lithium batteries, supercapacitors and fuel cells. *J. Mater. Chem. A* **2014**, *2*, 15-32.

(28) Global graphene market size is expected to reach $151.4 million and register a cagr of 47.7% by 2021, market trends, growth & forecast - valuates report. *PR Newswire* **2020**.

(29) Jiang, D.-e.; Cooper, V. R.; Dai, S. Porous graphene as the ultimate membrane for gas separation. *Nano Lett.* **2009**, *9*, 4019-4024.

(30) Koenig, S. P.; Wang, L.; Pellegrino, J.; Bunch, J. S. Selective molecular sieving through porous graphene. *Nat. Nanotechnol.* **2012**, *7*, 728.

(31) Liu, H.; Dai, S.; Jiang, D.-e. Permeance of h2 through porous graphene from molecular dynamics. *Solid State Commun.* **2013**, *175*, 101-105.

(32) Liu, H.; Dai, S.; Jiang, D.-e. Insights into CO_2/N_2 separation through nanoporous graphene from molecular dynamics. *Nanoscale* **2013**, *5*, 9984-9987.

(33) Liu, H.; Chen, Z.; Dai, S.; Jiang, D.-e. Selectivity trend of gas separation through nanoporous graphene. *J. Solid State Chem.* **2015**, *224*, 2-6.

(34) Tian, Z.; Mahurin, S. M.; Dai, S.; Jiang, D.-e. Ion-gated gas separation through porous graphene. *Nano Lett.* **2017**, *17*, 1802-1807.

(35) Herrera, C.; García, G.; Atilhan, M.; Aparicio, S. Nanowetting of graphene by ionic liquid droplets. *J. Phys. Chem. C* **2015**, *119*, 24529-24537.

(36) Liu, H.; Cooper, V. R.; Dai, S.; Jiang, D.-e. Windowed carbon nanotubes for efficient CO_2 removal from natural gas. *J. Phys. Chem. Lett.* **2012**, *3*, 3343-3347.

(37) Bucior, B. J.; Chen, D.-L.; Liu, J.; Johnson, J. K. Porous carbon nanotube membranes for separation of H_2/CH_4 and CO_2/CH_4 mixtures. *J. Phys. Chem. C* **2012**, *116*, 25904-25910.

(38) Li, Y.; Zhou, Z.; Shen, P.; Chen, Z. Two-dimensional polyphenylene: Experimentally available porous graphene as a hydrogen purification membrane. *Chem. Commun.* **2010**, *46*, 3672-3674.

(39) Inagaki, M.; Kang, F. Graphene derivatives: Graphane, fluorographene, graphene oxide, graphyne and graphdiyne. *J. Mater. Chem. A* **2014**, *2*, 13193-13206.

(40) Jiao, Y.; Du, A.; Hankel, M.; Zhu, Z.; Rudolph, V.; Smith, S. C. Graphdiyne: A versatile nanomaterial for electronics and hydrogen purification. *Chem. Commun.* **2011**, *47*, 11843-11845.

(41) Cranford, S. W.; Buehler, M. J. Selective hydrogen purification through graphdiyne under ambient temperature and pressure. *Nanoscale* **2012**, *4*, 4587-4593.

(42) Wang, P.; Li, W.; Du, C.; Zheng, X.; Sun, X.; Yan, Y.; Zhang, J. CO_2/N_2 separation via multilayer nanoslit graphene oxide membranes: Molecular dynamics simulation study. *Comp. Meter. Sci.* **2017**, *140*, 284-289.

(43) Li, W.; Zheng, X.; Dong, Z.; Li, C.; Wang, W.; Yan, Y.; Zhang, J. Molecular dynamics simulations of CO_2/N_2 separation through two-dimensional graphene oxide membranes. *J. Phys. Chem. C* **2016**, *120*, 26061-26066.

(44) Schrier, J. Carbon dioxide separation with a two-dimensional polymer membrane. *ACS Appl. Mater. Inter.* **2012**, *4*, 3745-3752.

(45) Brockway, A. M.; Schrier, J. Noble gas separation using pg-es x (x= 1, 2, 3) nanoporous two-dimensional polymers. *J. Phys. Chem. C* **2013**, *117*, 393-402.

(46) Solvik, K.; Weaver, J. A.; Brockway, A. M.; Schrier, J. Entropy-driven molecular separations in 2d-nanoporous materials, with application to high-performance paraffin/olefin membrane separations. *J. Phys. Chem. C* **2013**, *117*, 17050-17057.

(47) Tian, Z.; Dai, S.; Jiang, D.-e. Expanded porphyrins as two-dimensional porous membranes for CO_2 separation. *ACS Appl. Mater. Inter.* **2015**, *7*, 13073-13079.

Chapter 2. Computational Methods

This chapter will briefly introduce the computational methods used in this thesis and figure out the main purposes of using these methods. The details of specific computational methods used in each work will be discussed in each following chapter.

2.1 Density functional theory (DFT)

Many porous materials capture gas molecules by physisorption such as van der Waals (vdW) interaction.[1] To accurately calculate the interaction energy, we could use many methods, including Hartree-Fock (HF) method, Møller-Plesset perturbation calculation (MP2) method, and DFT methods.[2] Among them, DFT methods are widely used because they can not only calculate small molecular systems, but also simulate large and periodic systems.

2D membrane materials are extended unlimitedly in x and y directions. In simulations, we usually pick one or more unit cells as our simulation systems. The cell parameters and material structures need to be optimized by DFT methods firstly before doing further simulations. Then, gas molecules are added into the systems. Further optimization by DFT can help us find the adsorption bonding sites and calculate the bonding energies by following equation:

$$\Delta E = E_{total} - E_s - E_g$$

where ΔE is bonding energy, E_s is sorbent energy, E_g is gas molecule energy, and E_{total} is total energy after gas molecule has been bonded with sorbent material. The bonding energy differences between different gas molecules can help us estimate their Boltzmann factor or ideal pure-gas selectivity by Arrhenius equation.

2.2 Grand canonical Monte Carlo (GCMC)

GCMC is the most popular method to calculate gas molecule uptakes and simulate adsorption isotherms of porous materials.[3] In grand canonical (μVT) ensemble, chemical potential, temperature, and volume are fixed, while the total energy and total number of particles can be changed in all possible states of the system. Firstly, an initial N-particle system is established randomly. Then, a random trial move including insertion, deletion, or displacement is attempted. This trial move is accepted or rejected according to the Monte Carlo lottery. If it is accepted, a new microstate is obtained. After hundreds of hundreds of thousands of trials, many microstates are accepted. The ensemble average of them can tell us the properties of this system, such as the adsorption capacity. GCMC method is usually used for the study of sorbent-base materials.

2.3 Classical molecular dynamics (CMD)

CMD is a powerful computational method to study and analyze dynamics of gas molecules in sorbent-based or membrane-based materials. It determined dynamic trajectories of gas molecule by solving Newton's equations of motion. Instead of solving

Schrodinger equation base on quantum mechanics, the force considered in CMD come from classical interatomic potentials or so-called force field energy functions, which are a sum of terms with analytical formula and empirical parameters. There are two parts in total energy (E_{total}) of a system:

$$E_{total} = E_{bonded} + E_{nonbonded}$$

where E_{bonded} is covalent bonded energy terms, $E_{nonbonded}$ is nonbonded energy terms. The E_{bonded} is a sum of four parts: bond interaction between pairs of atoms (E_{bond}), angle interaction between triplets of atoms (E_{angle}), dihedral interaction between quadruplets of atoms ($E_{dihedral}$), and improper interaction between quadruplets of atoms ($E_{improper}$). In this thesis, they are expressed by following formulas:

$$E_{bond} = K_{bond}(r - r_0)^2$$

$$E_{angle} = K_{angle}(\theta - \theta_0)^2$$

$$E_{dihedral} = K_{dihedral}[1 + d_1 \cdot \cos(n_1\phi_1)]$$

$$E_{improper} = K_{improper}[1 + d_2 \cdot \cos(n_2\phi_2)]$$

where all K parameters are pre-factors, r and r_0 are actual and equilibrium bond distances, θ and θ_0 are actual and equilibrium angle values, d_1 and d_2 are equal to +1 or -1, d_1 and d_2 are non-negative integers, ϕ_1 and ϕ_2 are dihedral and improper dihedral angles.

The $E_{nonbonded}$ is a sum of two parts: van der Waals interaction ($E_{van\ der\ Waals}$) and electrostatic interaction ($E_{electrostatic}$). In this thesis, the former is described by standard 12/6 Lennard-Jones potential,[4] given by:

$$E_{van\ der\ Waals} = 4\varepsilon\left[\left(\frac{\sigma}{r}\right)^{12} - \left(\frac{\sigma}{r}\right)^{12}\right] \quad r < r_c$$

where ε is the depth of the potential well, σ is the finite distance at which the inter-particle potential is zero, r is the distance between the particles, r_c is the LJ cutoff distance. The is calculated by Coulomb's equation:

$$E_{electrostatic} = \frac{Cq_iq_j}{\varepsilon r} \quad r < r_c$$

where C is energy-conversion constant, q_i and q_j are the charges on the atoms, ε is the dielectric constant, r is the distance between the particles, r_c is the Coulombic cutoff distance.

The timestep used for CMD simulations is set to 1 fs. The simulations are usually on a time scale of 1-100 nanoseconds. Every fixed interval, the positions and distributions of gas molecules are recorded for further analyzing of properties, such as adsorption, diffusivity, permeability, and free energy.

2.4 Machine learning

Machine learning is a powerful tool to build a mathematical model based on sample data. It can find the relationship between different variables and make predictions or decisions. Machine learning is a very hot topic in recent years. Increasing numbers of algorithm are put forward. In this thesis, we will not discuss all of them. Instead, we pay attention to the artificial neural networks (ANNs).[5] More specifically, we mainly use feedforward neural network with backpropagation learning technique.[6,7] Typically, there are three types of layer: input layer, output layer, and hidden layer. Linear combination and nonlinear activation functions are applied to transfer the values. Suitable optimizers, such as stochastic gradient descent with momentum (SGDM) optimizer[8] and Adam optimizer,[9] are selected to search the optimal parameters in the best models. Once we obtain a well-trained model, we can use it to rapidly make prediction and explore the material databases. For the traditional theorical methods, such a huge amount of work is extremely time-consuming and unimaginable. This is one of the most important benefits for machine learning methods. In this thesis, we will use machine learning to study the porous carbon materials for selective CO_2 capture and make a little attempt at hydrogen storage metal clusters for determining hydrogen locations in them.

References

(1) Tian, Z.; Saito, T.; Jiang, D.-e. Ab initio screening of CO_2-philic groups. *J. Phys. Chem. A* **2015**, *119*, 3848-3852.

(2) Tian, Z.; Dai, S.; Jiang, D. e. What can molecular simulation do for global warming? *WIRES Comput. Mol. Sci.* **2016**, *6*, 173-197.

(3) Smit, B. Grand canonical monte carlo simulations of chain molecules: Adsorption isotherms of alkanes in zeolites. *Mol. Phys.* **1995**, *85*, 153-172.

(4) Jones, J. E. On the determination of molecular fields.—ii. From the equation of state of a gas. *Proceedings of the Royal Society of London. Series A, Containing Papers of a Mathematical and Physical Character* **1924**, *106*, 463-477.

(5) Chen, Y.-Y.; Lin, Y.-H.; Kung, C.-C.; Chung, M.-H.; Yen, I. Design and implementation of cloud analytics-assisted smart power meters considering advanced artificial intelligence as edge analytics in demand-side management for smart homes. *Sensors* **2019**, *19*, 2047.

(6) Zell, A. *Simulation neuronaler netze*; Addison-Wesley Bonn, 1994; Vol. 1.

(7) Rumelhart, D. E.; Hinton, G. E.; Williams, R. J. Learning representations by back-propagating errors. *Nature* **1986**, *323*, 533-536.

(8) Qian, N. On the momentum term in gradient descent learning algorithms. *Neural networks* **1999**, *12*, 145-151.

(9) Kingma, D. P.; Ba, J. Adam: A method for stochastic optimization. *arXiv preprint arXiv:1412.6980* **2014**

Chapter 3. Optimal Size of a Cylindrical Pore for Post-Combustion CO_2 Capture

3.1 Abstract

Pore size is an essential factor in controlling gas sorption in porous separation media. Overlap of the potential energy surface (PES) of CO_2 interacting with a cylindrical pore wall can be used to tune gas sorption inside a porous material, but how such overlap can benefit post-combustion CO_2 capture has not been fully addressed from a computational perspective. Here we use van der Waals density functional (vdW-DF) theory to assess the overlap of PES of CO_2 inside cylindrical pores as represented by carbon nanotubes (CNTs) of different diameters. Then we employ grand canonical Monte Carlo simulations to obtain the adsorption capacity and selectivity of a CO_2/N_2 mixture with a CO_2 partial pressure of 0.15 atm at room temperature. We find that the maximum PES overlap and maximum amount of CO_2 adsorbed are both achieved at a CNT diameter or cylindrical pore size of 7.8 Å, which corresponds to an accessible pore size of 4.4 Å. Further investigation of N_2 adsorption corroborates the idea of PES overlap. GCMC simulations reveal that a maximum CO_2/N_2 selectivity of ~33 is reached at a CNT diameter of 7.05 Å for the gas mixture. This work suggests that a cylindrical pore size between 7 and 8 Å would be most beneficial for post-combustion CO_2 capture from overlap of PES.

3.2 Introduction

With increasing emission of CO_2, global warming becomes one of the most critical environmental issues. Thus, CO_2 capture and storage (CCS) from large point sources of emission is important for reducing the global atmospheric concentration of CO_2.[1-2] Post-combustion CO_2 capture from flue gas is a crucial choice to reduce CO_2 emission.[3-4] Both chemisorption and physisorption can be used for CO_2 separation from flue gas.[5-7] Several recent articles have reported a diverse range of promising porous materials for CO_2 capture.[1, 8-12]

Zeolites and activated carbons are traditional porous materials for gas adsorption.[13] Metal organic frameworks (MOFs) have shown great potential for CO_2 adsorption, due to their chemical diversity, intrinsic porosity, and abundant functionality.[14-23] The MOF-74 family with high density of open metal sites has excellent performance of CO_2 adsorption.[24-26] Covalent organic frameworks (COFs) can also serve as promising CO_2 sorbents.[27-31] Researchers have successfully developed strategies for converting a conventional 2D COF into an outstanding CO_2 capture scaffold through channel-wall functionalization.[28]

Optimizing pore size is an another important strategy for CO_2 adsorption.[32-36] Zaworotko et al. reported a MOF comprised of hexafluorosilicate.[37-39] The pore sizes within these "SIFSIX" materials can be controlled by changing the length of the organic linkers, the metal node, and framework interpenetration. They found that SIFSIX-3-Zn with a pore size of 3.84 Å had outstanding CO_2 uptake and selectivity. They further studied SIFSIX-3-Cu with a smaller pore size of 3.5 Å which showed higher CO_2 uptake. Recently, Jung et al. reported the optimal slit pore size for CO_2 capture by using the bilayer graphene,[40] while simulation of gas adsorption and separation by ordered carbon nanotube arrays mainly focused on double-walled tubes with a rather large and fixed inner-tube diameter of 3.0 nm with varying intertube distances[41-42] and relatively high pressure conditions.[43]

Although there are many previous studies of porous materials for CO_2 adsorption, the fundamental question of an optimal cylindrical pore size for post combustion CO_2 capture has not been clearly addressed. Especially, one can envision that when the cylindrical pore size is very small (< 1 nm), significant overlap of potential energy surface between CO_2 and the pore walls. To address this question, herein we use first-principles van der Waals density functional theory (vdW-DFT) to map out the potential energy surfaces of CO_2 in cylindrical pores, which are modeled by carbon nanotubes (CNTs); compared with the empirical Lennard-Jones potentials, vdW-DFT as an electronic-structure method is free of empirical parameters and able to describe the polarization of charge density due to the CO_2-CNT interaction. Then we study the overlap of potential energy surfaces by adjusting the pore size (the CNT diameter). Next, we perform the grand canonical Monte Carlo simulation to obtain the optimal pore size for adsorbing CO_2 and reveal the relationship between the PES overlap and adsorption performance of the cylindrical pore for post-combustion CO_2 capture.

3.3 Computational Method

The van der Waals corrected density functional (vdW-DF) calculations[44] were performed by using the Vienna ab initio simulation package (VASP).[45-47] The Perdew–Burke–Ernzerhof (PBE) form of the generalized-gradient approximation (GGA) was used for electron exchange and correlation.[48] The projector-augmented-wave (PAW) method was used to describe the electron-core interaction.[49] The plane waves cutoff energy of 450 eV was used. A supercell with cell parameters of a = b = 20.0 Å, c = 21.3 Å, $\alpha = \beta = \gamma = 90^\circ$ was used for calculation of CO_2 in nanotube system. A CO_2 molecule was put in the center of CNTs in the axial direction. A 1 × 1 × 1 Monkhorst Pack k-point grid was chosen for sampling the Brillouin zone. The convergence threshold for geometry optimization was set to be 0.025 eV/Å in force, and the thicknesses of the vacuum layer were all set to be larger than 10 Å. The CNTs were kept fixed during all the calculations. For CO_2, carbon atom was fixed, and oxygen atoms were allowed to relax in all directions. For N_2, nitrogen atoms were only allowed to relax in nitrogen-nitrogen bond direction. The potential energy (E_{pot}) was defined by $E_{pot} = E_{CNT+CO_2} - (E_{CNT} + E_{CO_2})$ or $E_{pot} = E_{graphene+N_2} - (E_{graphene} + E_{N_2})$.

In order to simulate the adsorption of CO_2 and selectivity of CO_2/N_2 at close to the experimental conditions, the grand canonical Monte Carlo (GCMC) simulation at constant chemical potential μ, volume V and temperature T was used. The CNTs were arranged on a hexagonal bundle structure with minimal intertube distance. The force-field parameters from previous studies were used for the CNTs[42], CO_2,[50] and N_2.[50] The vdW interactions between different atoms were calculated by the Lorentz-Berthelot Rules. The cutoff for the interatomic interactions was 12.8 Å. The temperature was fixed at 298K. All GCMC simulations ran 10^7 steps.

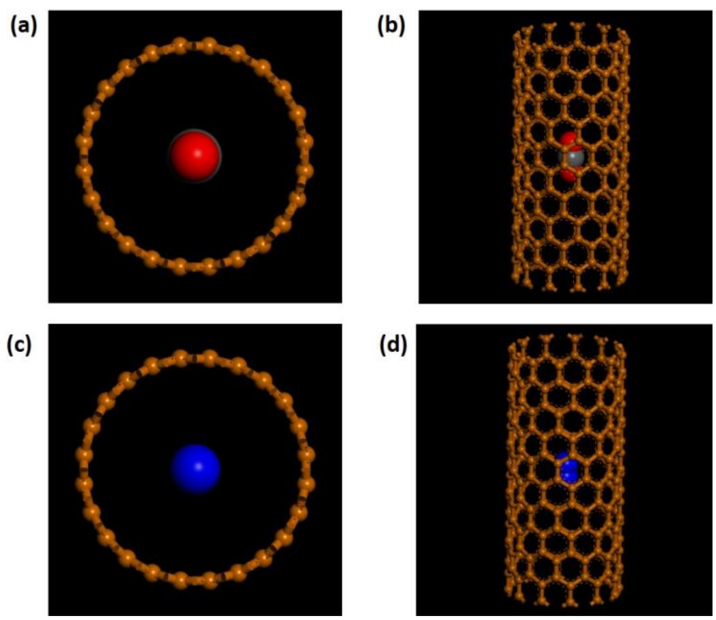

Figure 3-1. Structure of CO_2 (a and b) and N_2 (c and d) inside the carbon nanotube in our DFT modeling.

3.4 Results and discussion

3.4.1 Potential energy surface of CO_2 and N_2 in carbon nanotubes.

Besides slit pores, the cylindrical pores are often used to simulate porous materials. Here we used carbon nanotubes (CNTs) to model a cylindrical pore. Figure 3-1 shows that we placed CO_2 or N_2 inside the CNTs along the axis. The radial position of the CNT axis was set at zero and the diameters of the CNTs were adjusted by the indices [n, 0]. Then for a given CNT, we computed the energy of the whole system as we changed the radial position of CO_2 or N_2 along a random direction in both ways to generate the potential energy surface (PES) curve.

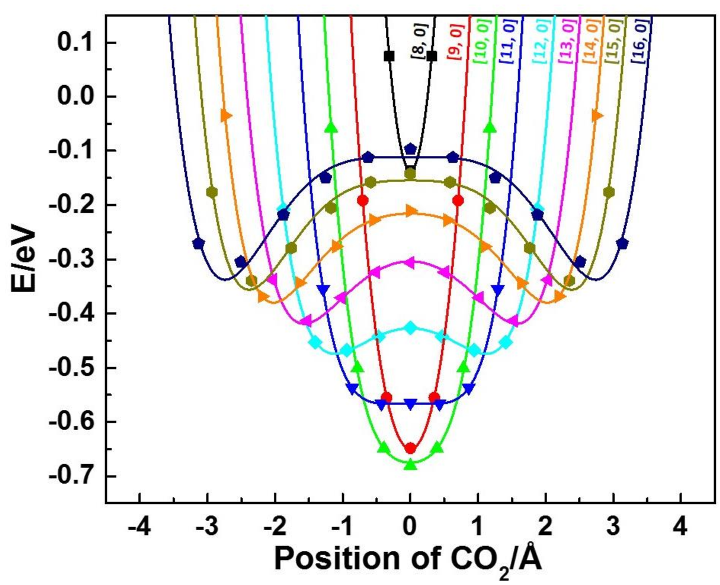

Figure 3-2. Potential energy surface of CO_2 in the CNTs calculated by the vdW-DF method.

As shown in Figure 3-2, we started with a relatively large nanotube CNT [16, 0] and then decreased it to CNT [8, 0]. We can see that all the potential energy surfaces are symmetric. For CNT [16, 0], there are two minima where both the maximum binding energy are 0.34 eV. With the decrease of the diameter, the overlap effect becomes increasingly strong and the maximum bonding energy becomes larger. For CNT [11, 0], the double-well shape of the PES changes to a flat-bottom, single-well form, where the maximum binding energy is 0.56 eV and the width of this potential energy bottom is about 1.4 Å. Apparently, this is the size where the two peaks in the PES curve begin to merge into one. When the diameter or cylindrical pore size decreases further, the PES changes to a parabola shape with an increasingly sharper bottom. The lowest bottom is reached by CNT [10, 0] with a diameter of 7.8 Å, corresponding to the strongest binding of CO_2 at 0.675 eV. At this pore size, optimal overlap of PES is achieved. Further narrower CNTs such as CNT [9, 0] and [8, 0] have a weakened interaction with CO_2 because of repulsion against the wall, especially in CNT [8, 0]. Here, we used a simple definition of the CNT diameter as the pore size. The accessible pore size often used in the literature would correspond to the CNT diameter minus the vdW diameter of the carbon atom (3.4 Å; that is, the wall thickness), so a diameter of 7.8 Å would correspond to an accessible pore size of 4.4 Å.

The PES curves of N_2 in the CNTs were also obtained in the same way (Figure 3-3). The shapes of all curves are similar to those of CO_2 in Figure 3-2. However, the bonding energies of N_2 with CNTs are always weaker when those of CO_2. The maximum interaction is also reached by CNT [10, 0] for N_2 with a binding energy of 0.523 eV.

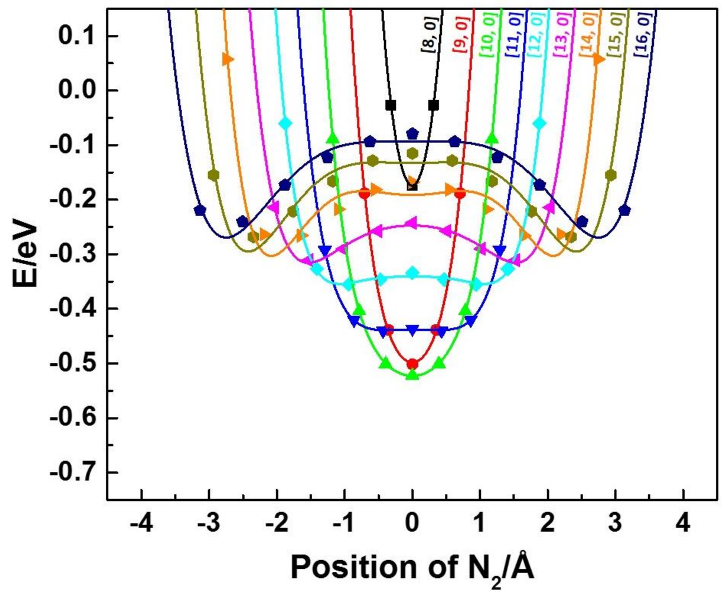

Figure 3-3. Potential energy surface of N_2 in the CNTs calculated by the vdW-DF method.

3.4.2 Optimal pore size from the potential energy surface.

To shed light on the optimal cylindrical pore size, Figure 3-4 plots the PES minimum versus the diameter of the CNT. We can see that the strongest binding is achieved at about 7.8 Å with a minimum of -0.675 eV for CO_2. This value of CO_2 binding is much stronger than the optimal value in the case of the graphene bilayer slit pore,[40] indicating that the curvature increases CO_2 binding. This can be explained by the fact that the CNT wraps around the linear, rod-like CO_2 so that there are more carbon atoms from the CNT can be in close contact with CO_2 than those from the two planar graphene sheets. In addition, Figure 3-4 shows that the bonding of N_2 is weaker than that of CO_2 by about 15% to 25% for the same CNT.

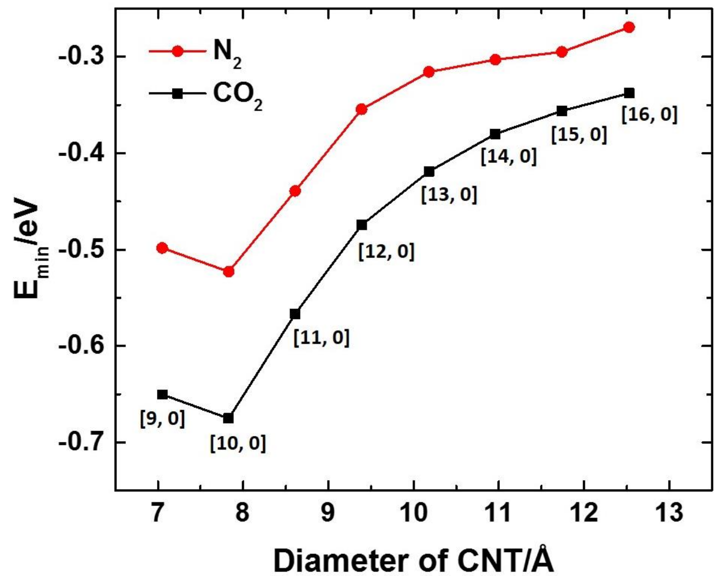

Figure 3-4. The minimum values of potential energy for different diameters of CNTs.

Figure 3-5 shows the difference in the potential energy between N_2 and CO_2 for different diameters of CNTs, which is an indication of the CO_2/N_2 selectivity; in other words, the more positive the difference, the higher the CO_2/N_2 selectivity. One can see that the selectivity can be best achieved by a cylindrical pore size of 7 Å to 8 Å; the 0.15 eV energy difference yields a Boltzmann factor or ideal pure-gas selectivity of 372 at room temperature (298.15 K) for CO_2/N_2 separation. The selectivity is expected to decrease with the increase of CNT diameter.

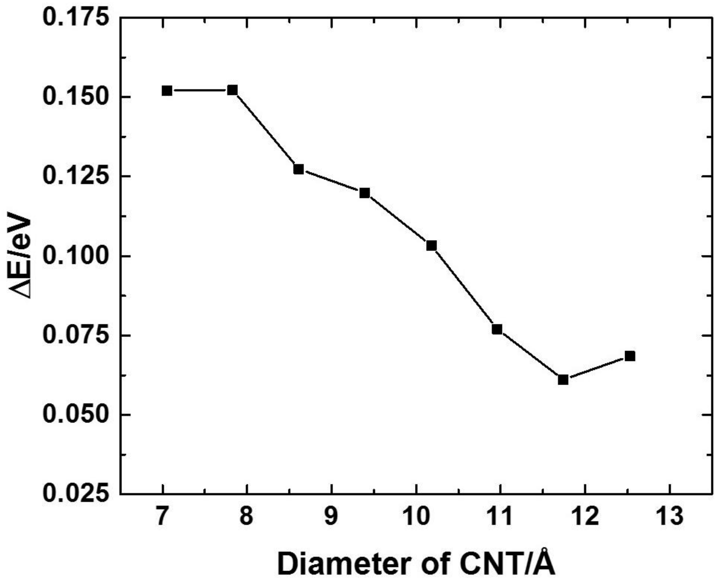

Figure 3-5. The difference in the potential energy between N_2 and CO_2 for different diameters of CNTs.

3.4.3 GCMC simulations of pure-gas CO_2 and N_2 uptakes inside the CNTs.

The PES overlap and the optimal size for selectivity from the first principles vdW-DF results above best represent the low to ambient pressure conditions where the strong adsorption sizes are populated. To test these predictions, we employed GCMC to simulate CO_2 and N_2 uptakes inside the CNTs at ambient conditions that are relevant to post-combustion CO_2 capture. First, we simulated the isotherms up to 1 atm at 298 K (Figure 3-6). One can see that at 0.1 atm, CNT [9, 0] (d = 7.05 Å), CNT [10, 0] (d = 7.83 Å), and CNT [11, 0] (d = 8.61 Å) have higher CO_2 uptake (Figure 3-6a) than the larger-sized CNTs. With the increasing pressure, the CNTs with larger pore sizes begin to win over the smaller-sized ones. At 1 bar, CNT [14, 0] (d = 10.96 Å) has the highest CO_2 uptake (4.59 mol/kg). Figure 3-6b shows the isotherms of N_2. Interestingly, the N_2 uptake in this pressure region well follows the PES curves in Figures 3-3 and 3-4: CNT [9, 0] (d = 7.05 Å) and [10, 0] (d = 7.83 Å) have the best PES overlap, so their N_2 uptake is the highest from 0 to 1 atm. This difference between CO_2 and N_2 in terms of pressure and pore size dependences can be leveraged for CO_2/N_2 separation.

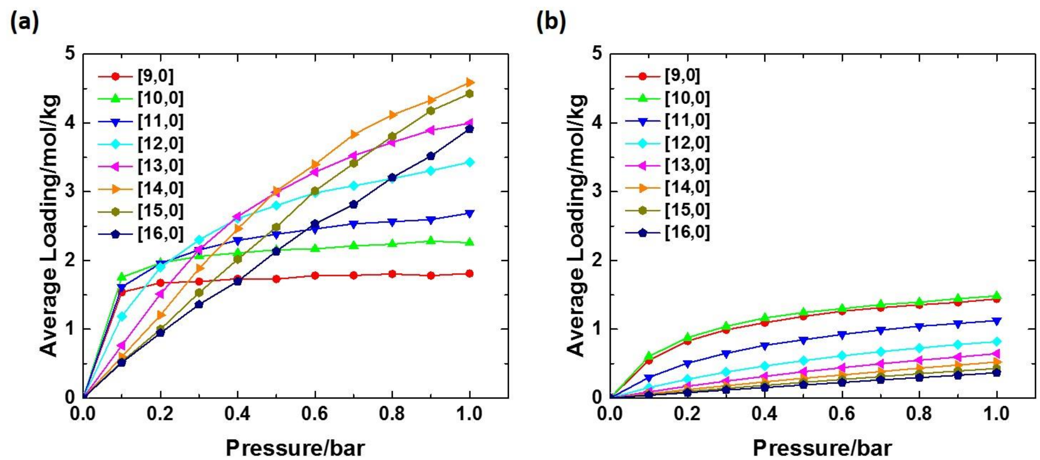

Figure 3-6. The isotherms of (a) CO_2 and (b) N_2 at 298K for different diameters of CNTs.

Figure 3-7 shows the snapshots of CO_2 distribution inside CNTs of different sizes at 0.15 atm. When the diameter of CNT is small in the cases of [9,0] and [10,0], the CO_2 molecules concentrate at the center of CNTs along the central axis, but when the diameter is larger as in [11,0], some CO_2 molecules move away from the central axis toward the wall. While the CO_2 molecules are more or less oriented along the central axis in CNT [9,0], some CO_2 molecules are actually oriented almost perpendicularly to the central axis in CNT [10,0].

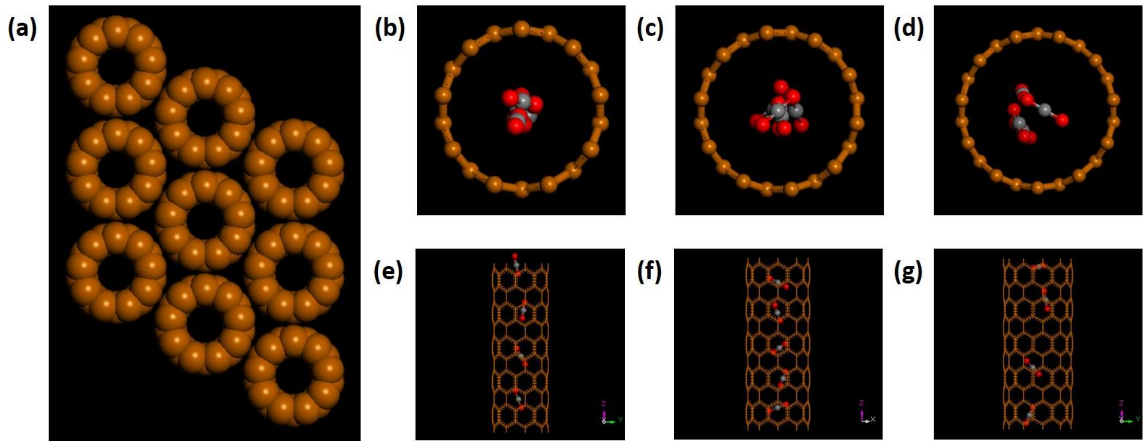

Figure 3-7. CNT bundle in GCMC simulation (a); and CO_2 distribution inside the CNT [9, 0] (b, e), CNT [10,0] (c, f) and CNT [11,0] (d, g); (b-d) are the top view figures and (e-g) are the side view figures.

3.4.4 GCMC simulations of CO_2/N_2 mixture inside the CNTs.

To be relevant to the experimental conditions, we simulated the gas uptake and the CO_2/N_2 selectivity of a 15%/85% molar ratio mixture of CO_2/N_2 at 1 atm and 298 K. Figure 3-8 shows how the gas uptake and the CO_2/N_2 selectivity change with the CNT diameter. One can see that CO_2 uptake is highest at the pore size of 7.8 Å, while N_2 uptake is highest at 10.3 Å. One can also see that the CO_2 uptake of 1.5 mol/kg from the mixture is similar to that in the pure-gas isotherm at the same partial pressure (Figure 3-6a). Due to this preferential adsorption of CO_2 from the mixture, N_2 uptake inside the CNTs from the mixture is much less than that in the pure-gas isotherm (Figure 3-6b). Figure 3-8 also shows the CO_2/N_2 selectivity, defined as

$$S_{i/j} = (x_i / x_j)(y_j / y_i)$$

where x_i and y_i are the mole fractions of component i in adsorbed and bulk phases, respectively. One can see that the highest selectivity (~33) is obtained at the pore size of 7.05 Å for CNT [9,0]. The selectivity decreases to below 15 when the pore size is greater than 10 Å.

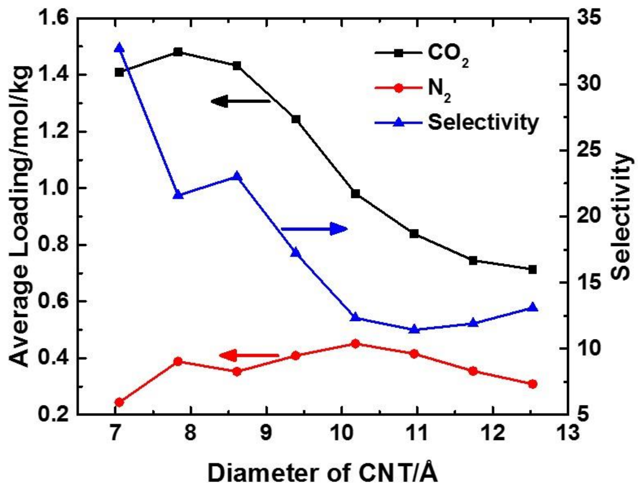

Figure 3-8. Gas uptake and CO_2/N_2 selectivity from a mixture of CO_2 (0.15 atm) and N_2 (0.85 atm) at 298K for different diameters of CNTs.

3.4.5 Selectivity from the Ideal Adsorbed Solution Theory (IAST).

Besides direct simulation of adsorption of mixture gases, another simple way to estimate the adsorption selectivity for gas mixtures is via the Ideal Adsorbed Solution Theory (IAST).[42, 51-52] Because CNT [9,0] exhibits the highest selectivity from the GCMC simulations (Figure 3-8), we applied the IAST to determine how CO_2/N_2 selectivity changes as a function of pressure for a mixture of CO_2 and N_2 in 0.15/0.85 molar ratio inside the CNT [9,0]. As shown in Figure 3-9, IAST predicts a CO_2/N_2 selectivity of 38.8 at 1 atm, very close to the GCMC result (~33) in Figure 3-8.

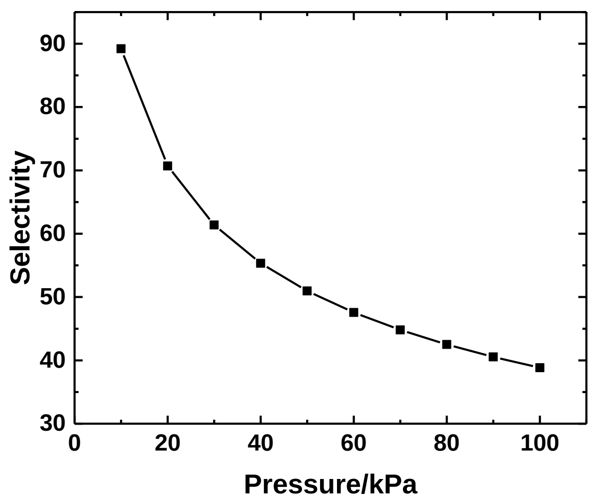

Figure 3-9. The IAST-predicted CO_2/N_2 selectivity as a function of total pressure for a mixture of CO_2 and N_2 in 0.15/0.85 molar ratio in CNT [9, 0].

3.4.6 Implications for the practical separation of CO_2 and N_2.

The enhanced CO_2 adsorption and CO_2/N_2 selectivity inside the small-diameter CNTs as predicted above beg the questions of their practicality in real-world applications, such as how to deploy them and whether the desorption could be an issue due to the enhanced interaction. We expect that the desorption should be facile for N_2 due to the much weaker N_2-CNT interaction. Although the CO_2-CNT interaction here is enhanced through the potential energy surface overlap, the interaction is still physisorption in nature and the magnitude is still lower than the chemisorption. To demonstrate this point, we compare the CNT with the conventional 13X zeolite. At a loading of 1.5 to 1.7 mmol/g, the average isosteric heat of adsorption of CO_2 is about 40 kJ/mol in 13X[53] and about 44 kJ/mol in CNT [9,0] from our own calculation. In other words, the CO_2-CNT interaction is only slightly stronger than the CO_2-13X interaction. So we think that like the 13X zeolite, the narrow CNTs can also be used for pressure-swing adsorption for CO_2/N_2 separation,[54] given their similar isotherms and heat of adsorption.

Although the present work focuses on the pore size, other factors may also contribute to the gas uptake and selectivity. These include surface chemistry and functionality, surface defects, and surface area. It would be interesting to find out how the pore size can combine with these other factors in affecting post-combustion CO_2 capture. Further simulations are warranted.

3.5 Summary and conclusions

We have investigated the overlap of potential energy surface (PES) of CO_2 in cylindrical pores modeled by CNTs from first principles van der Waals density functional (vdW-DF) theory. We further simulated the pore-size effect on CO_2 uptake and CO_2/N_2 selectivity for post-combustion CO_2 capture. By changing the diameter of CNTs, we found that the optimal pore size for overlap of PES is about 7.8 Å for the cylindrical pore. The binding strength of CO_2 inside the 7.8-Å CNT triples that between CO_2 and a single layer of graphene. We have also performed the GCMC simulations to obtain the uptakes of CO_2 at low pressure and the CO_2/N_2 selectivity from a mixture. The results show that CNTs with a pore size between 7 and 8 Å is particularly good for achieving high CO_2/N_2 selectivity (~ 33) and good CO_2 uptake (1.5 mol/kg) for a 0.15atm/0.85atm CO_2/N_2 mixture at 298 K. Our work shows that cylindrical pores of 7 to 8 Å in size are promising for post-combustion CO_2 capture.

References

(1) D'Alessandro, D. M.; Smit, B.; Long, J. R. Carbon dioxide capture: Prospects for new materials. *Angew. Chem. Int. Ed.* **2010**, *49*, 6058-6082.

(2) Zhang, X.; Zhang, X.; Dong, H.; Zhao, Z.; Zhang, S.; Huang, Y. Carbon capture with ionic liquids: Overview and progress. *Energy Env. Sci.* **2012**, *5*, 6668-6681.

(3) Samanta, A.; Zhao, A.; Shimizu, G. K. H.; Sarkar, P.; Gupta, R. Post-combustion CO_2 capture using solid sorbents: A review. *Ind. Eng. Chem. Res.* **2012**, *51*, 1438-1463.

(4) Babarao, R.; Jiang, Y. Q.; Medhekar, N. V. Postcombustion CO_2 capture in functionalized porous coordination networks. *J. Phys. Chem. C* **2013**, *117*, 26976-26987.

(5) Haszeldine, R. S. Carbon capture and storage: How green can black be? *Science* **2009**, *325*, 1647-1652.

(6) Gibbins, J.; Chalmers, H. Carbon capture and storage. *Energy Policy* **2008**, *36*, 4317–4322.

(7) Patel, H. A.; Byun, J.; Yavuz, C. T. Carbon dioxide capture adsorbents: Chemistry and methods. *Chemsuschem* **2017**, *10*, 1303-1317.

(8) Wang, J. Y.; Huang, L.; Yang, R. Y.; Zhang, Z.; Wu, J. W.; Gao, Y. S.; Wang, Q.; O'Hare, D.; Zhong, Z. Y. Recent advances in solid sorbents for CO_2 capture and new development trends. *Energy Env. Sci.* **2014**, *7*, 3478-3518.

(9) Jiang, F.; Jin, T.; Zhu, X.; Tian, Z.; Do-Thanh, C.-L.; Hu, J.; Jiang, D.-e.; Wang, H.; Liu, H.; Dai, S. Substitution effect guided synthesis of task-specific nanoporous polycarbazoles with enhanced carbon capture. *Macromolecules* **2016**, *49*, 5325-5330.

(10) Tian, Z. Q.; Dai, S.; Jiang, D. E. What can molecular simulation do for global warming? *WIRES Comput. Mol. Sci.* **2016**, *6*, 173-197.

(11) Dura, G.; Budarin, V. L.; Castro-Osma, J. A.; Shuttleworth, P. S.; Quek, S. C.; Clark, J. H.; North, M. Importance of micropore-mesopore interfaces in carbon dioxide capture by carbon-based materials. *Angew. Chem. Int. Ed.* **2016**, *55*, 9173-9177.

(12) Ahmed, A.; Babarao, R.; Huang, R. H.; Medhekar, N.; Todd, B. D.; Hill, M. R.; Thornton, A. W. Porous aromatic frameworks impregnated with lithiated fullerenes for natural gas purification. *J. Phys. Chem. C* **2015**, *119*, 9347-9354.

(13) Choi, S.; Drese, J. H.; Jones, C. W. Adsorbent materials for carbon dioxide capture from large anthropogenic point sources. *ChemSusChem* **2009**, *2*, 796-854.

(14) Sumida, K.; Rogow, D. L.; Mason, J. A.; McDonald, T. M.; Bloch, E. D.; Herm, Z. R.; Bae, T. H.; Long, J. R. Carbon dioxide capture in metal-organic frameworks. *Chem. Rev.* **2012**, *112*, 724-781.

(15) McDonald, T. M.; Lee, W. R.; Mason, J. A.; Wiers, B. M.; Hong, C. S.; Long, J. R. Capture of carbon dioxide from air and flue gas in the alkylamine-appended metal-organic framework mmen-mg-2(dobpdc). *J. Am. Chem. Soc.* **2012**, *134*, 7056-7065.

(16) Ma, S. Q.; Zhou, H. C. Gas storage in porous metal-organic frameworks for clean energy applications. *Chem. Commun.* **2010**, *46*, 44-53.

(17) Cui, Y. J.; Li, B.; He, H. J.; Zhou, W.; Chen, B. L.; Qian, G. D. Metal-organic frameworks as platforms for functional materials. *Acc. Chem. Res.* **2016**, *49*, 483-493.

(18) Wang, C.; Liu, D. M.; Lin, W. B. Metal-organic frameworks as a tunable platform for designing functional molecular materials. *J. Am. Chem. Soc.* **2013**, *135*, 13222-13234.

(19) Millward, A. R.; Yaghi, O. M. Metal-organic frameworks with exceptionally high capacity for storage of carbon dioxide at room temperature. *J. Am. Chem. Soc.* **2005**, *127*, 17998-17999.

(20) Zhai, Q. G.; Bu, X.; Mao, C.; Zhao, X.; Daemen, L.; Cheng, Y.; Ramirez-Cuesta, A. J.; Feng, P. An ultra-tunable platform for molecular engineering of high-performance crystalline porous materials. *Nature Comm.* **2016**, *7*, 13645.

(21) Zhai, Q. G.; Bu, X.; Mao, C.; Zhao, X.; Feng, P. Systematic and dramatic tuning on gas sorption performance in heterometallic metal-organic frameworks. *J. Am. Chem. Soc.* **2016**, *138*, 2524-2527.

(22) Zhai, Q. G.; Bai, N.; Li, S.; Bu, X.; Feng, P. Design of pore size and functionality in pillar-layered zn-triazolate-dicarboxylate frameworks and their high CO_2/CH_4 and c2 hydrocarbons/CH_4 selectivity. *Inorg. Chem.* **2015**, *54*, 9862-9868.

(23) Huang, R. H.; Hill, M. R.; Babarao, R.; Medhekar, N. V. CO_2 adsorption in azobenzene functionalized stimuli responsive metal-organic frameworks. *J. Phys. Chem. C* **2016**, *120*, 16658-16667.

(24) Valenzano, L.; Civalleri, B.; Chavan, S.; Palomino, G. T.; Arean, C. O.; Bordiga, S. Computational and experimental studies on the adsorption of CO, N_2, and CO_2 on mg-MOF-74. *J. Phys. Chem. C* **2010**, *114*, 11185-11191.

(25) Yang, D. A.; Cho, H. Y.; Kim, J.; Yang, S. T.; Ahn, W. S. CO_2 capture and conversion using Mg-MOF-74 prepared by a sonochemical method. *Energy Env. Sci.* **2012**, *5*, 6465-6473.

(26) Yu, J. M.; Balbuena, P. B. Water effects on postcombustion CO_2 capture in mg-MOF-74. *J. Phys. Chem. C* **2013**, *117*, 3383-3388.

(27) Zeng, Y. F.; Zou, R. Q.; Zhao, Y. L. Covalent organic frameworks for CO_2 capture. *Adv. Mater.* **2016**, *28*, 2855-2873.

(28) Huang, N.; Chen, X.; Krishna, R.; Jiang, D. Two-dimensional covalent organic frameworks for carbon dioxide capture through channel-wall functionalization. *Angew. Chem. Int. Ed.* **2015**, *54*, 2986-2990.

(29) Huang, N.; Krishna, R.; Jiang, D. Tailor-made pore surface engineering in covalent organic frameworks: Systematic functionalization for performance screening. *J. Am. Chem. Soc.* **2015**, *137*, 7079-7082.

(30) Stegbauer, L.; Hahn, M. W.; Jentys, A.; Savasci, G.; Ochsenfeld, C.; Lercher, J. A.; Lotsch, B. V. Tunable water and CO_2 sorption properties in isostructural azine-based covalent organic frameworks through polarity engineering. *Chem. Mater.* **2015**, *27*, 7874-7881.

(31) Ullah, R.; Atilhan, M.; Anaya, B.; Al-Muhtaseb, S.; Aparicio, S.; Patel, H.; Thirion, D.; Yavuz, C. T. Investigation of ester- and amide-linker-based porous organic polymers for carbon dioxide capture and separation at wide temperature's and pressures. *ACS Appl. Mater. Inter.* **2016**, *8*, 20772-20785.

(32) An, J.; Rosi, N. L. Tuning MOF CO_2 adsorption properties via cation exchange. *J. Am. Chem. Soc.* **2010**, *132*, 5578-5579.

(33) Bae, Y. S.; Snurr, R. Q. Development and evaluation of porous materials for carbon dioxide separation and capture. *Angew. Chem. Int. Ed.* **2011**, *50*, 11586-11596.

(34) Tian, Z. Q.; Dai, S.; Jiang, D. E. Expanded porphyrins as two-dimensional porous membranes for CO_2 separation. *ACS Appl. Mater. Inter.* **2015**, *7*, 13073-13079.

(35) Wang, H.; Cao, D. P. Diffusion and separation of H_2, CH_4, CO_2, and N_2 in diamond-like frameworks. *J. Phys. Chem. C* **2015**, *119*, 6324-6330.

(36) Zhang, H. B.; Zeng, X. F.; Zhao, Z. Y.; Zhai, Z. Q.; Cao, D. P. Adsorption and selectivity of CH_4/CO_2 in functional group rich organic shales. *J. Nat. Gas Sci. Eng.* **2017**, *39*, 82-89.

(37) Kumar, A.; Madden, D. G.; Lusi, M.; Chen, K. J.; Daniels, E. A.; Curtin, T.; Perry, J. J.; Zaworotko, M. J. Direct air capture of CO_2 by physisorbent materials. *Angew. Chem. Int. Ed.* **2015**, *54*, 14372-14377.

(38) Shekhah, O.; Belmabkhout, Y.; Chen, Z. J.; Guillerm, V.; Cairns, A.; Adil, K.; Eddaoudi, M. Made-to-order metal-organic frameworks for trace carbon dioxide removal and air capture. *Nature Comm.* **2014**, *5*, 4228.

(39) Nugent, P.; Belmabkhout, Y.; Burd, S. D.; Cairns, A. J.; Luebke, R.; Forrest, K.; Pham, T.; Ma, S. Q.; Space, B.; Wojtas, L.; Eddaoudi, M.; Zaworotko, M. J. Porous materials with optimal adsorption thermodynamics and kinetics for CO_2 separation. *Nature* **2013**, *495*, 80-84.

(40) Kwac, K.; Lee, J. H.; Choi, J. W.; Jung, Y. Computational analysis of pressure-dependent optimal pore size for CO_2 capture with graphitic surfaces. *J. Phys. Chem. C* **2016**, *120*, 3978-3985.

(41) Rahimi, M.; Singh, J. K.; Babu, D. J.; Schneider, J. J.; Muller-Plathe, F. Understanding carbon dioxide adsorption in carbon nanotube arrays: Molecular simulation and adsorption measurements. *J. Phys. Chem. C* **2013**, *117*, 13492-13501.

(42) Rahimi, M.; Singh, J. K.; Muller-Plathe, F. Adsorption and separation of binary and ternary mixtures of SO_2, CO_2 and N_2 by ordered carbon nanotube arrays: Grand-canonical monte carlo simulations. *Phys. Chem. Chem. Phys.* **2016**, *18*, 4112-4120.

(43) Kowalczyk, P.; Brualla, L.; Zywocinski, A.; Bhatia, S. K. Single-walled carbon nanotubes: Efficient nanomaterials for separation and on-board vehicle storage of hydrogen and methane mixture at room temperature? *J. Phys. Chem. C* **2007**, *111*, 5250-5257.

(44) Dion, M.; Rydberg, H.; Schroder, E.; Langreth, D. C.; Lundqvist, B. I. Van der waals density functional for general geometries. *Phys. Rev. Lett.* **2004**, *92*, 246401.

(45) Kresse, G.; Furthmuller, J. Efficient iterative schemes for ab initio total-energy calculations using a plane-wave basis set. *Phys. Rev. B* **1996**, *54*, 11169-11186.

(46) Klimes, J.; Bowler, D. R.; Michaelides, A. Van der waals density functionals applied to solids. *Phys. Rev. B* **2011**, *83*, 195131.

(47) Roman-Perez, G.; Soler, J. M. Efficient implementation of a van der waals density functional: Application to double-wall carbon nanotubes. *Phys. Rev. Lett.* **2009**, *103*, 096102.

(48) Perdew, J. P.; Burke, K.; Ernzerhof, M. Generalized gradient approximation made simple. *Phys. Rev. Lett.* **1996**, *77*, 3865-3868.

(49) Blochl, P. E. Projector augmented-wave method. *Phys. Rev. B* **1994**, *50*, 17953-17979.

(50) Liu, H. J.; Dai, S.; Jiang, D. E. Insights into CO_2/N_2 separation through nanoporous graphene from molecular dynamics. *Nanoscale* **2013**, *5*, 9984-9987.

(51) Cannon, J. J.; Vlugt, T. J. H.; Dubbeldam, D.; Maruyama, S.; Shiomi, J. Simulation study on the adsorption properties of linear alkanes on, closed nanotube bundles. *J. Phys. Chem. B* **2012**, *116*, 9812-9819.

(52) Lee, J. H.; Kwac, K.; Lee, H. J.; Lim, S. Y.; Jung, D. S.; Jung, Y.; Choi, J. W. Optimal activation of porous carbon for high performance CO_2 capture. *Chemnanomat* **2016**, *2*, 528-533.

(53) Lee, J. S.; Kim, J. H.; Kim, J. T.; Suh, J. K.; Lee, J. M.; Lee, C. H. Adsorption equilibria of CO_2 on zeolite 13x and zeolite x/activated carbon composite. *J. Chem. Eng. Data* **2002**, *47*, 1237-1242.

(54) Takamura, Y.; Narita, S.; Aoki, J.; Hironaka, S.; Uchida, S. Evaluation of dual-bed pressure swing adsorption for CO_2 recovery from boiler exhaust gas. *Sep. Purif. Technol.* **2001**, *24*, 519-528.

Chapter 4. Effect of Pore Density on Gas Permeation through Nanoporous Graphene Membranes

4.1 Abstract

Pore density is an important factor dictating gas separations through one-atom-thin nanoporous membranes, but how it influences the gas permeation has not been fully understood. Here we use molecular dynamics (MD) simulations to investigate gas permeation through nanoporous graphene membranes with the same pore (3.0 Å × 3.8 Å in dimensions) but varying pore densities (from 0.01 to 1.28 nm^{-2}). We find that higher pore density leads to higher permeation per unit area of membrane for both CO_2 and He, but the rate of the increase decreases greatly for CO_2 at high pore densities. As a result, the per-pore permeance decreases for CO_2 but remains relatively constant for He with the pore density. By separating the total flux into direct flux and surface flux, we find that He permeation is dominated by direct flux and hence the per-pore permeation rate is roughly constant with the pore density. In contrast, CO_2 permeation is dominated by surface flux. The overall decreasing trend of the per-pore permeation rate of CO_2 with the pore density can be explained by the decrease of coverage per pore on feed side with the increase of pore density and the coverage per pore on permeate side can be ignored. Our work now provides a complete picture of the pore-density dependence of gas permeation through one-atom-thin nanoporous membranes.

4.2 Introduction

Graphene with sub-nanometer pores is promising as a one-atom-thin membrane for applications in separations of gases, water, ions, and isotopes.[1-11] Porous graphene was first proposed as the ultimate membrane for gas separation in 2009 by a computational proof-of-concept.[12] In 2012, molecular sieving of gases through porous graphene membranes with controlled pore sizes was experimentally demonstrated.[13] Meanwhile, porous graphene membranes and their derivatives have been predicted to be able to separate hydrogen isotopes.[14] To achieve scalable production of porous graphene membranes, graphene-oxide (GO) membranes have been fabricated and tested for gas separations.[15-17] Recently, other two-dimensional materials have also been examined as porous membranes.[18-23] For example, the MoS_2 nanosheets with suitable triangular pores were proposed for separating H_2 from N_2, CO, and CH_4 and for removing CO_2 from natural gas,[19] while molecular sieving of gases was shown for a MXene membrane.[23]

Although molecular sieving has been the main working mechanism for selective gas separations by porous graphene and related ultrathin membranes,[24] Drahushuk and Strano proposed two pathways of gas permeation through nanoporous graphene membranes from a detailed kinetic analysis: direct gas-phase pathway and adsorbed phase pathway.[25] In the gas-phase pathway, the flux scales with the pore area and the differential pressure. In the adsorbed phase pathway, the permeation is divided into five steps:

adsorption, association, translocation, dissociation, and desorption.[25] Hadjiconstantinou et al. further explored the impact of pore size and pore functionalization on gas permeation through nanoporous graphene membrane by theoretical analysis and MD simulations.[26]

Although the role of pore density has been alluded to in several previous studies,[27-31] how exactly the pore density affects permeation has not been fully addressed, especially in the light of the direct gas-phase pathway vs the indirect adsorbed phase or surface pathway. In a more recent theoretical analysis combined with simulations for the adsorption-translocation mechanism, a minimum pore density has been identified for the porous graphene membrane to achieve sufficient permeance.[31] But finding an optimal pore density would help guide both the top-down and bottom-up syntheses of ultrathin membranes with desired pore densities.

The goal of the current work is to understand the role of pore density in gas permeation through porous graphene. To this end, we have built a series of nanoporous graphene membrane models with different pore densities using the same pore, and then used classical molecular dynamics (CMD) simulation to study the relationship of gas permeation with the pore density. We chose CO_2 and He, which represent two different types of gas molecule with strong and weak adsorption onto the nanoporous graphene membrane surface, respectively. By comparing the permeation behaviors of CO_2 and He, we aim to achieve a deeper understanding of how gas permeation depends on pore density on a porous graphene and to probe the direct vs indirect pathways.

4.3 Computational Method

To simulate the effect of pore density, the same membrane dimensions of 10 nm × 10 nm and the same pore are employed, while the number of pores increases from 1 to 128 (Figure 4-1a-h), corresponding to pore densities from 0.01 nm^{-2} to 1.28 nm^{-2}. The size of simulation box is 10 nm × 10 nm × 20 nm. The pore has dimensions of 3.0 Å × 3.8 Å (see Figure S4-1 in the electronic supplementary information, ESI) and has been used previously for $H_2/CO_2/N_2/CH_4$ separations; it has very good performances for selective gas separations, for example, a selectivity of 300 for CO_2/N_2 separation with a CO_2 permeance on the order of 10^5 GPU.[32, 33] A bi-chamber system (Figure 4-1i) with two-dimensional periodic boundary conditions is set up in our classical MD simulations, with the porous graphene membrane in the middle. The upper chamber is pressurized at 20 atm by 550 gas molecules of CO_2 or He for all graphene sheets of different pore densities, while the lower chamber is vacuum initially. MD simulations are performed using the LAMMPS package[34] in the canonical (NVT) ensemble at 300 K controlled using the Nose-Hoover thermostat.[35, 36] The force-field parameters for the membrane and gas molecules are taken from previous studies.[33, 37, 38] Only the non-bonded interactions (van der Waals and electrostatic) are considered. The graphene membrane is fixed, and the gas molecules are rigid during the simulations. The Lennard-Jones parameters and partial atomic charges are provided in ESI.

The cutoff distances for Lennard-Jones and Coulombic interactions are 12 Å; the long-range electrostatic interaction is calculated using the PPPM method.[39-41]

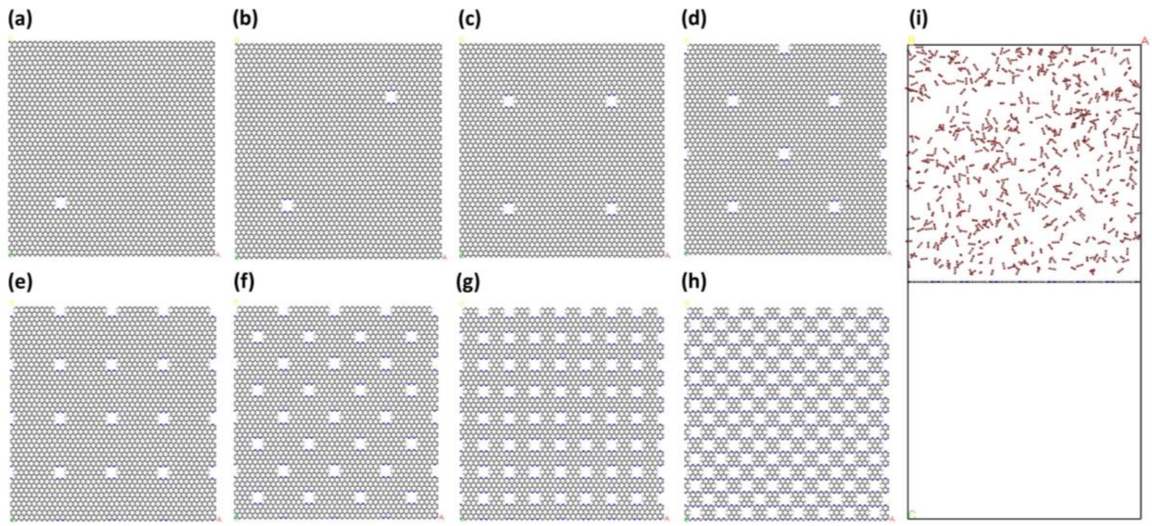

Figure 4-1. The 10×10 nm^2 porous-graphene membrane with different pore densities of the same pore (3.0 Å ×3.8 Å in size; see Figure S4-1 in ESI for a close-up view of the pore): (a) 0.01 nm^{-2}; (b) 0.02 nm^{-2}; (c) 0.04 nm^{-2}; (d) 0.08 nm^{-2}; (e) 0.16 nm^{-2}; (f) 0.32 nm^{-2}; (g) 0.64 nm^{-2}; (h) 1.28 nm^{-2}. (i) Side view of the bi-chamber setup for simulating gas permeation through the membrane in the middle; the upper chamber (the feed side) is pressurized at 20 atm while the lower chamber (the permeate side) is vacuum initially.

4.4 Results and discussion

4.4.1 Gas permeation through the nanoporous graphene membranes

Figure 4-2 shows the MD simulation results of the number of the gas molecules permeating through the porous graphene membrane with time for different pore densities. One can see that for both CO_2 (Figure 4-2a) and He (Figure 4-2b), the permeation rate (the slope of the line) increases with the pore density. This can be seen more clearly in the first 5 ns of the simulations (Figure 4-2c,d). In addition, we can see that when the pore density is relatively high (> 0.16 nm^{-2}), equilibrium can be reached within about 5 ns when pressure difference across the membranes approaches zero. To compare the permeation rates for the different pore densities, we used the initial slopes from our simulations (dashed lines in Figure 4-2c,d).

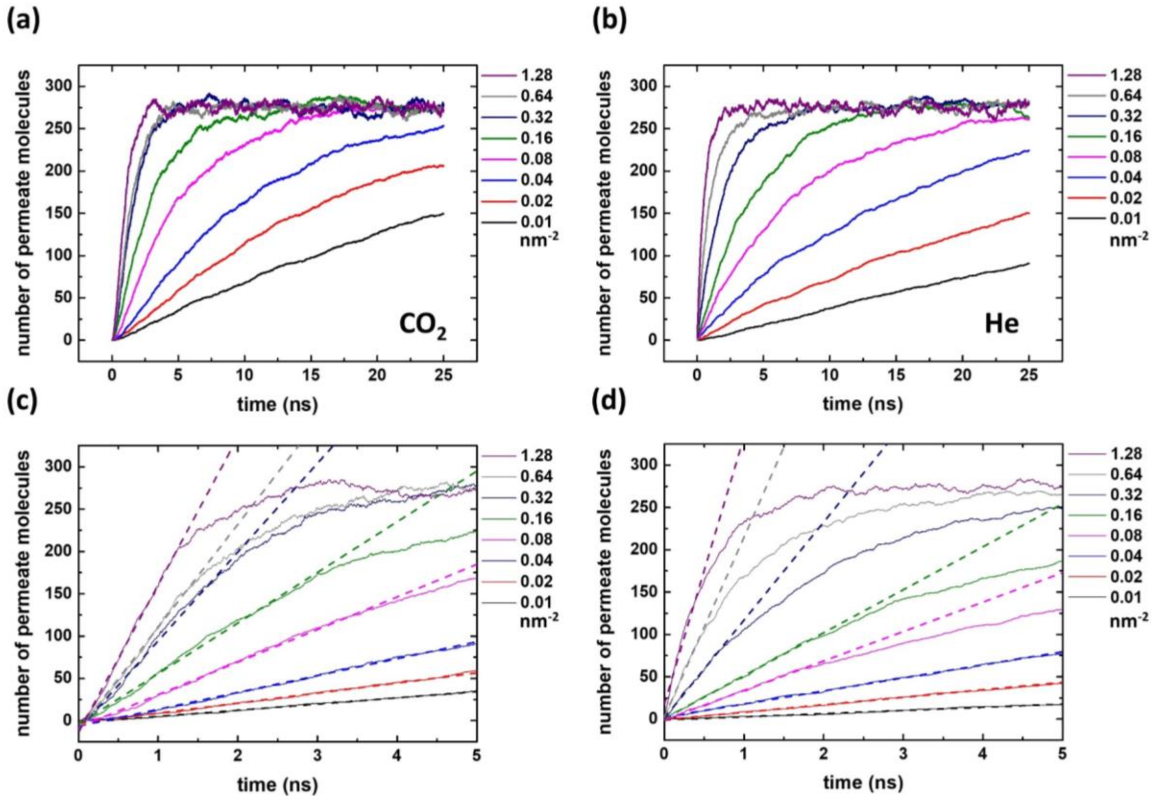

Figure 4-2. The number of gas molecules permeating through the nanoporous graphene membrane with time for different pore densities (from 0.01 to 1.28 nm^{-2}): (a) CO_2 in 25 ns; (b) He in 25 ns; (c) CO_2 in 5 ns; (d) He in 5 ns. Dashed lines in (c) and (d) denote the permeation rates used to compute the initial fluxes.

From the initial permeation rate and the membrane total area (100 nm^2), we computed the initial flux as a function of the pore density. Figure 4-3a shows that the flux of He increases almost linearly with the pore density, while the flux of CO_2 shows a similar linear increase when the pore density is < 0.3 nm^{-2} but the increase greatly slows down after 0.3 nm^{-2}. Figure 4-3c shows the bulk-pressure-normalized flux (that is, permeance). At the pore density of 1.28 nm^{-2}, the flux of CO_2 is about 60% that of He and corresponds to a permeance of ~ 6×10^6 GPU. This permeance is higher than the typical permeance found for one-atom-thin membranes (~ 10^4 to 10^5 GPU) from previous simulations[18, 33, 42, 43] because of the higher pore densities employed in this work. We also used an exponential decay model to fit the whole curves in Figure 4-2 and obtained similar trends of fluxes for both CO_2 and He (see Figure S4-3 in ESI).

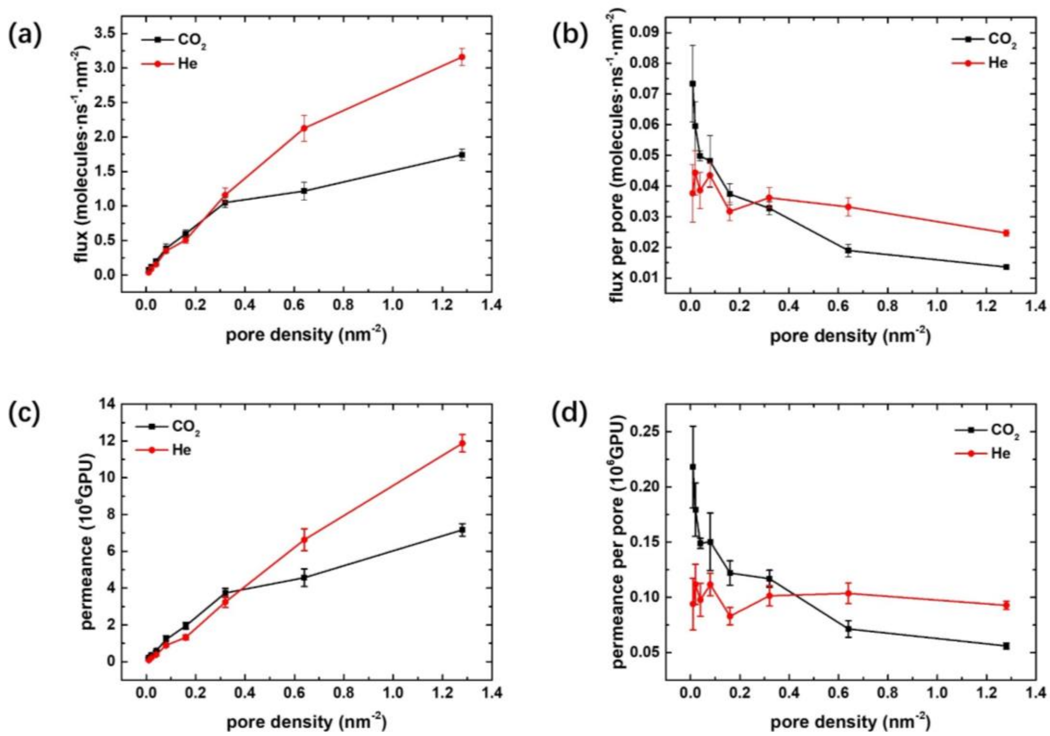

Figure 4-3. Initial flux and permeance vs pore density of graphene membranes for CO_2 and He permeation: (a) flux per unit membrane area; (b) flux per pore; (c) permeance; (d) permeance per pore. Error bars from averaging over parallel simulations.

The difference between CO_2 and He regarding the flux vs pore density trend can be more clearly seen in terms of the per-pore flux. One can see from Figure 4-3b that at low pore densities the initial flux per pore is higher for CO_2 than He, even though He is smaller in size. This reverse selectivity is not uncommon in the literature of gas-separation membranes. For example, some polymeric membranes are selective for CO_2 than the smaller H_2, due to CO_2's higher solubility in these polymers.[44] The underlying reason is similar in our case, due to the much more favorable surface adsorption of CO_2 than He on the membrane, as explained below. Over the whole range of the pore densities, Figure 4-3b shows that the initial flux per pore is nearly constant for He, but displays a roughly exponential decay with the pore density for CO_2. This distinct and interesting difference between CO_2 and He begs a detailed analysis of their permeation behaviors through the porous graphene membranes of different pore densities. We first examine the adsorption behavior.

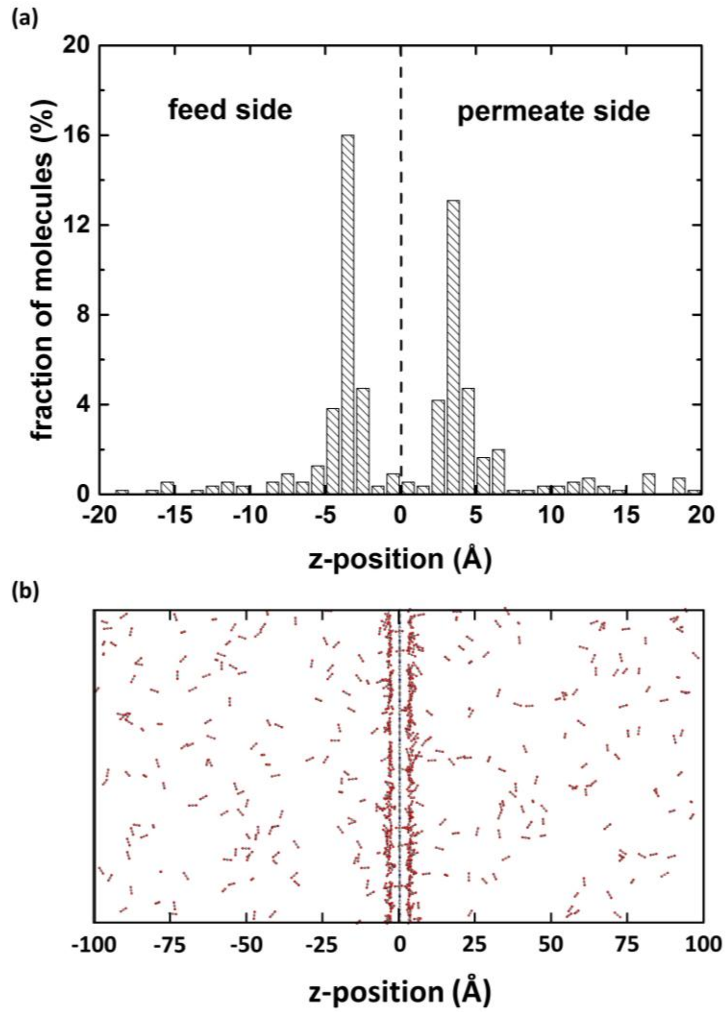

Figure 4-4. CO_2 distribution along the z direction for a graphene membrane (at z=0) with the pore density of 1.28 nm^{-2} after 25 ns MD simulation: (a) statistical distribution at the 25-ns time point (bin size: 1 Å); (b) snapshot of CO_2 distribution at the 25-ns time point.

4.4.2 Gas adsorption on the nanoporous graphene membranes

Being a larger molecule with a large quadrupole moment, CO_2 adsorbs more strongly than He on the graphene membrane. Figure 4-4 shows the distribution of CO_2 molecules along the direction perpendicular to the membrane surface after the equilibrium has been reached across the membrane. One can clearly see the adsorption layer on both sides of the membrane: each layer is about 5 Å thick, with the majority of the CO_2 molecules about 3 to 4 Å away from the graphene surface. Some CO_2 molecules with z < 3 Å are actually close to or in the pore.

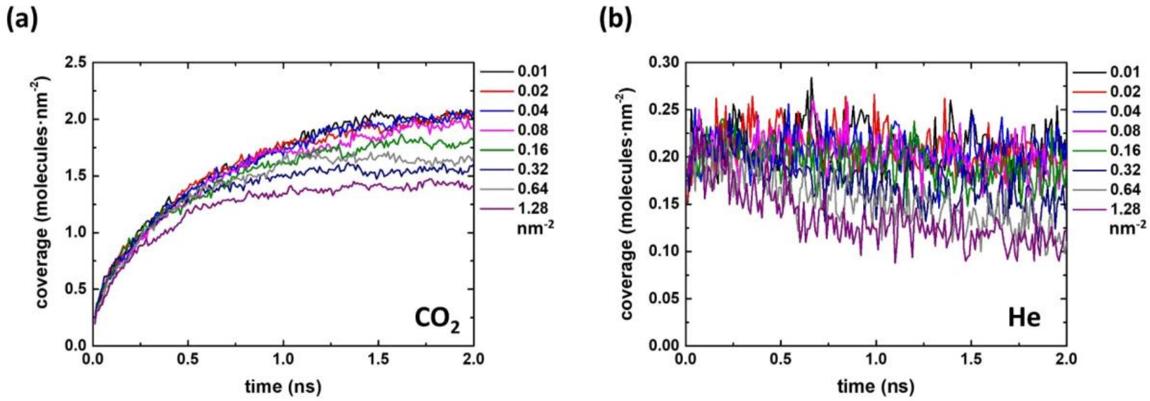

Figure 4-5. Coverage of the gas adsorbate vs time on the feed side of the graphene membranes of different pore densities: (a) CO_2; (b) He.

Next, we examined how fast the adsorption layers are built up on both sides of the graphene membrane. Figure 4-5 shows the adsorption on the feed side of the membrane. One can see that regardless of the pore density, CO_2 adsorption on the feed side quickly reaches equilibrium within about 1 ns (Figure 4-5a). In contrast, He coverage is much lower and shows much greater fluctuation (Figure 4-5b). Similarly, we proceed to analyze the adsorption on the permeate or back side of the membrane. As shown in Figure 4-6, the change of gas coverage with time displays a strong dependence on the pore density, especially for CO_2 (Figure 4-6a). Figure 4-7a shows that the initial adsorption rate on the permeate side increases with the pore density for both CO_2 and He. This increase is expected to closely correlate with the pressure rise in the permeate side; indeed, after pressure normalization, the adsorption rate becomes roughly constant at high pore densities (Figure 4-7b).

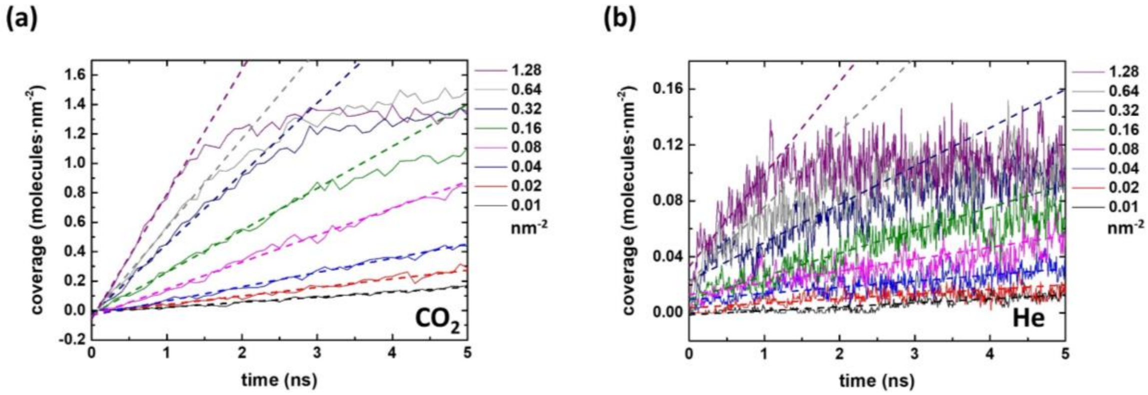

Figure 4-6. Coverage of the adsorbate vs time on the permeate side of the graphene membrane of different pore densities: (a) CO_2; (b) He.

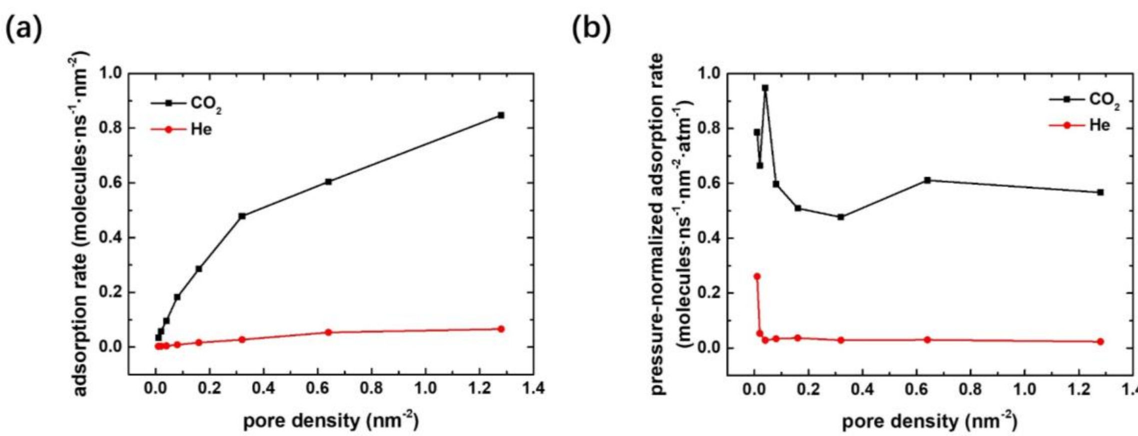

Figure 4-7. (a) Adsorption rate and (b) pressure-normalized adsorption rate on the permeate side vs the pore density for CO_2 and He.

Figures 4-5 to 4-7 indicate that adsorption plays an important role in the dependence of CO_2 permeation on the pore density. However, to fully understand the trends in Figure 4-3, we need to quantify the contribution of surface adsorption to the total flux relative to that of the direct flux.

4.4.3 Surface flux vs direct flux

According to a previous kinetic analysis of gas permeation through a porous graphene membrane, the total flux can be decomposed into direct flux and surface flux.[25, 26] To assess their contributions, we have tracked all gas molecules in our simulations individually and analyzed their trajectories during the initial 1 ns, to determine the numbers of the different events. This allowed us to obtain the surface vs direct flux contributions. For He, we found that the total flux is dominated by the direct flux and the surface flux can be ignored (especially at high pore densities, see Figure 4-8b), due to the weak adsorption (as evidenced from Figure 4-5b and Figure 4-6b). Since the direct flux scales with the permeable area (which in turns scales with the pore density), one expects a net flux linear with the pore density or a constant per-pore flux, as seen in Figure 4-3 for He.

On the other hand, CO_2 shows a completely different behavior. We found that the CO_2 total flux per pore is dominated by the surface flux, as the direct flux is minor for all pore densities (Figure 4-8a), due to the strong adsorption (as evidenced from Figure 4-5a and Figure 4-6a). Since the surface flux is relevant to surface adsorption, we will discuss the effect of adsorption behavior below.

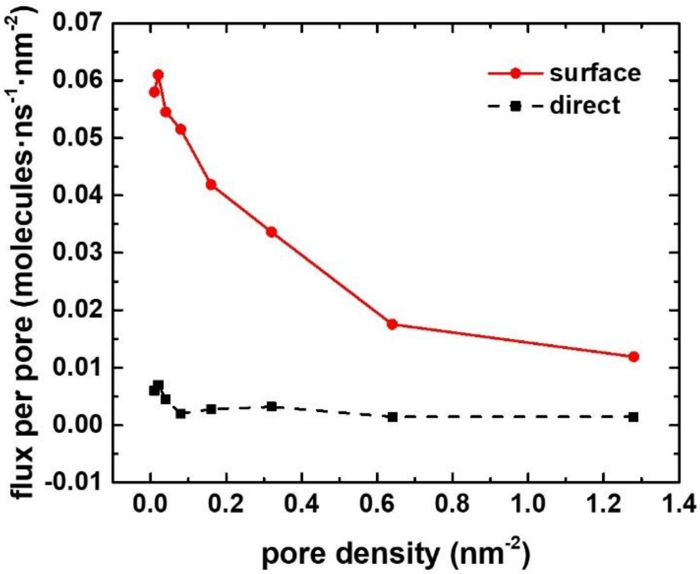

Figure 4-8. The surface flux and the direct flux of CO_2, across graphene membranes of different pore densities. The values are from the trajectory analysis of all gas molecules during the initial 1 ns.

4.4.4 The relationship between adsorption and surface flux for CO_2

Figure 4-8 suggests that surface flux is the dominating part for CO_2. To analyze the relationship between adsorption and surface flux per pore, we plot coverage per pore vs. pore density, as shown in Figure 4-9. Compared with the coverage per pore on feed side, the coverage per pore on permeate side can be ignored. The similar curve trends of coverage per pore on feed side and surface flux per pore in Figure 4-8 indicates a close relationship between them.

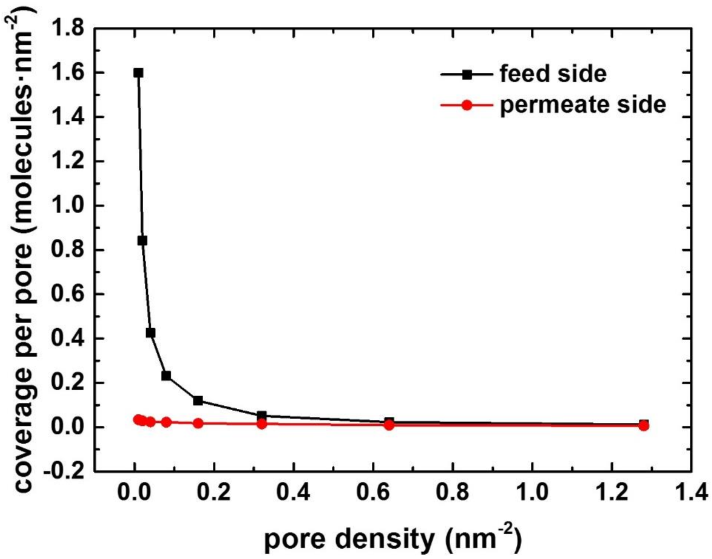

Figure 4-9. Coverage per pore of CO_2 on feed side and permeate side of the graphene membrane of different pore densities.

4.4.5 Implications

The present work revealed some interesting trends of gas permeation across the porous graphene membranes of different pore densities. Our simulations showed that the higher the pore density, the greater the flux for both strongly and weakly adsorbing gases. This is expected. More important, we found that the adsorption on both sides of the membrane greatly modulates the dependence of the flux on the pore density for a strongly adsorbing gas such as CO_2. The observation suggests that making the membranes asymmetric by creating dissimilar surfaces could lead to more interesting permeation behavior.

4.5 Summary and conclusions

We have investigated permeation of CO_2 and He through nanoporous graphene membranes with varying pore densities (from 0.01 nm^{-2} to 1.28 nm^{-2}) by using molecular dynamics (MD) simulations. Higher pore density will yield higher permeation rate for both CO_2 and He per unit area of membrane, but the increase rate decreases greatly for CO_2. Separating the total permeation flux into direct flux and surface flux allowed us to find that He permeation is dominated by direct flux, leading to a relatively flat per-pore flux with the pore density. In contrast, CO_2 permeation is dominated by the surface flux. The per-pore flux of CO_2 decreases with the pore density overall, mainly due to the decrease of coverage per pore of the adsorbed CO_2 molecules on feed side with the increase of pore density. The present work provides insights into the pore-density dependence of gas permeation through a one-atom-thin membrane and also suggests new ways to improve the design of ultrathin membranes for gas separations.

References

(1) Tian, Z. Q.; Dai, S.; Jiang, D. E. What can molecular simulation do for global warming? *WIREs Comput. Mol. Sci.* **2016**, *6*, 173-197.

(2) Gadipelli, S.; Guo, Z. X. Graphene-based materials: Synthesis and gas sorption, storage and separation. *Prog. Mater Sci.* **2015**, *69*, 1-60.

(3) Surwade, S. P.; Smirnov, S. N.; Vlassiouk, I. V.; Unocic, R. R.; Veith, G. M.; Dai, S.; Mahurin, S. M. Water desalination using nanoporous single-layer graphene. *Nat. Nanotechnol.* **2015**, *10*, 459-464.

(4) Liu, G. P.; Jin, W. Q.; Xu, N. P. Graphene-based membranes. *Chem. Soc. Rev.* **2015**, *44*, 5016-5030.

(5) Suk, M. E.; Aluru, N. R. Water transport through ultrathin graphene. *J. Phys. Chem. Lett.* **2010**, *1*, 1590-1594.

(6) Cohen-Tanugi, D.; Grossman, J. C. Water desalination across nanoporous graphene. *Nano Lett.* **2012**, *12*, 3602-3608.

(7) Sint, K.; Wang, B.; Kral, P. Selective ion passage through functionalized graphene nanopores. *J. Am. Chem. Soc.* **2008**, *130*, 16448-16449.

(8) Hu, G. H.; Mao, M.; Ghosal, S. Ion transport through a graphene nanopore. *Nanotechnology* **2012**, *23*, 395501.

(9) Ji, A. P.; Li, Z. W.; Yang, H. J.; He, P. Y.; Chen, Y. F. Transport of water and ions through a graphene nanopore in an electric field. *Biophys. J.* **2017**, *112*, 544a.

(10) Hauser, A. W.; Schwerdtfeger, P. Nanoporous graphene membranes for efficient ^{3}he/^{4}he separation. *J. Phys. Chem. Lett.* **2012**, *3*, 209-213.

(11) Hauser, A. W.; Schrier, J.; Schwerdtfeger, P. Helium tunneling through nitrogen-functionalized graphene pores: Pressure- and temperature-driven approaches to isotope separation. *J. Phys. Chem. C* **2012**, *116*, 10819-10827.

(12) Jiang, D. E.; Cooper, V. R.; Dai, S. Porous graphene as the ultimate membrane for gas separation. *Nano Lett.* **2009**, *9*, 4019-4024.

(13) Koenig, S. P.; Wang, L. D.; Pellegrino, J.; Bunch, J. S. Selective molecular sieving through porous graphene. *Nat. Nanotechnol.* **2012**, *7*, 728-732.

(14) Hankel, M.; Jiao, Y.; Du, A. J.; Gray, S. K.; Smith, S. C. Asymmetrically decorated, doped porous graphene as an effective membrane for hydrogen isotope separation. *J. Phys. Chem. C* **2012**, *116*, 6672-6676.

(15) Li, H.; Song, Z. N.; Zhang, X. J.; Huang, Y.; Li, S. G.; Mao, Y. T.; Ploehn, H. J.; Bao, Y.; Yu, M. Ultrathin, molecular-sieving graphene oxide membranes for selective hydrogen separation. *Science* **2013**, *342*, 95-98.

(16) Kim, H. W.; Yoon, H. W.; Yoon, S. M.; Yoo, B. M.; Ahn, B. K.; Cho, Y. H.; Shin, H. J.; Yang, H.; Paik, U.; Kwon, S.; Choi, J. Y.; Park, H. B. Selective gas transport through few-layered graphene and graphene oxide membranes. *Science* **2013**, *342*, 91-95.

(17) Mi, B. X. Graphene oxide membranes for ionic and molecular sieving. *Science* **2014**, *343*, 740-742.

(18) Tian, Z. Q.; Dai, S.; Jiang, D. E. Expanded porphyrins as two-dimensional porous membranes for CO_2 separation. *ACS Appl. Mater. Inter.* **2015**, *7*, 13073-13079.

(19) Zhang, Y. D.; Meng, Z. S.; Shi, Q.; Gao, H. Q.; Liu, Y. Z.; Wang, Y. H.; Rao, D. W.; Deng, K. M.; Lu, R. F. Nanoporous MoS_2 monolayer as a promising membrane for purifying hydrogen and enriching methane. *J. Phys. Condens. Mat.* **2017**, *29*, 375201.

(20) Xu, B.; Xiang, H.; Wei, Q.; Liu, J. Q.; Xia, Y. D.; Yin, J.; Liu, Z. G. Two-dimensional graphene-like c2n: An experimentally available porous membrane for hydrogen purification. *Phys. Chem. Chem. Phys.* **2015**, *17*, 15115-15118.

(21) Liu, G. P.; Jin, W. Q.; Xu, N. P. Two-dimensional-material membranes: A new family of high-performance separation membranes. *Angew. Chem. Int. Ed.* **2016**, *55*, 13384-13397.

(22) Zheng, Z. K.; Grunker, R.; Feng, X. L. Synthetic two-dimensional materials: A new paradigm of membranes for ultimate separation. *Adv. Mater.* **2016**, *28*, 6529-6545.

(23) Ding, L.; Wei, Y. Y.; Li, L. B.; Zhang, T.; Wang, H. H.; Xue, J.; Ding, L. X.; Wang, S. Q.; Caro, J.; Gogotsi, Y. Mxene molecular sieving membranes for highly efficient gas separation. *Nat. Commun.* **2018**, *9*, 155.

(24) Ismail, A. F.; David, L. I. B. A review on the latest development of carbon membranes for gas separation. *J. Membrane Sci.* **2001**, *193*, 1-18.

(25) Drahushuk, L. W.; Strano, M. S. Mechanisms of gas permeation through single layer graphene membranes. *Langmuir* **2012**, *28*, 16671-16678.

(26) Sun, C. Z.; Boutilier, M. S. H.; Au, H.; Poesio, P.; Bai, B. F.; Karnik, R.; Hadjiconstantinou, N. G. Mechanisms of molecular permeation through nanoporous graphene membranes. *Langmuir* **2014**, *30*, 675-682.

(27) Holt, J. K.; Park, H. G.; Wang, Y. M.; Stadermann, M.; Artyukhin, A. B.; Grigoropoulos, C. P.; Noy, A.; Bakajin, O. Fast mass transport through sub-2-nanometer carbon nanotubes. *Science* **2006**, *312*, 1034-1037.

(28) Sircar, S.; Golden, T. C.; Rao, M. B. Activated carbon for gas separation and storage. *Carbon* **1996**, *34*, 1-12.

(29) Gin, D. L.; Noble, R. D. Designing the next generation of chemical separation membranes. *Science* **2011**, *332*, 674-676.

(30) Liu, H. J.; Dai, S.; Jiang, D. E. Permeance of h_2 through porous graphene from molecular dynamics. *Solid State Commun.* **2013**, *175*, 101-105.

(31) Yuan, Z.; Rajan, A. G.; Misra, R. P.; Drahushuk, L. W.; Agrawal, K. V.; Strano, M. S.; Blankschtein, D. Mechanism and prediction of gas permeation through sub-

nanometer graphene pores: Comparison of theory and simulation. *ACS Nano* **2017**, *11*, 7974-7987.

(32) Liu, H. J.; Chen, Z. F.; Dai, S.; Jiang, D. E. Selectivity trend of gas separation through nanoporous graphene. *J. Solid State Chem.* **2015**, *224*, 2-6.

(33) Liu, H. J.; Dai, S.; Jiang, D. E. Insights into CO_2/N_2 separation through nanoporous graphene from molecular dynamics. *Nanoscale* **2013**, *5*, 9984-9987.

(34) Plimpton, S. Fast parallel algorithms for short-range molecular-dynamics. *J. Comput. Phys.* **1995**, *117*, 1-19.

(35) Nose, S. A unified formulation of the constant temperature molecular-dynamics methods. *J. Chem. Phys.* **1984**, *81*, 511-519.

(36) Hoover, W. G. Canonical dynamics - equilibrium phase-space distributions. *Phys. Rev. A* **1985**, *31*, 1695-1697.

(37) Neyertz, S. Molecular dynamics simulations of helium permeation in polyimides with a bulky dianhydride and a fluorinated diamine. *Macromol. Theory Simul.* **2007**, *16*, 513-524.

(38) Aziz, R. A.; Janzen, A. R.; Moldover, M. R. Ab-initio calculations for helium - a standard for transport property measurements. *Phys. Rev. Lett.* **1995**, *74*, 1586-1589.

(39) Hockney, R. W.; Eastwood, J. W. *Computer simulation using particles*; CRC Press, 1988.

(40) Yeh, I. C.; Berkowitz, M. L. Ewald summation for systems with slab geometry. *J. Chem. Phys.* **1999**, *111*, 3155-3162.

(41) Ballenegger, V.; Arnold, A.; Cerda, J. J. Simulations of non-neutral slab systems with long-range electrostatic interactions in two-dimensional periodic boundary conditions. *J. Chem. Phys.* **2009**, *131*, 094107.

(42) Schrier, J. Carbon dioxide separation with a two-dimensional polymer membrane. *ACS Appl. Mater. Inter.* **2012**, *4*, 3745-3752.

(43) Strano, M. S.; Foley, H. C. Temperature- and pressure-dependent transient analysis of single component permeation through nanoporous carbon membranes. *Carbon* **2002**, *40*, 1029-1041.

(44) Lin, H. Q.; Van Wagner, E.; Freeman, B. D.; Toy, L. G.; Gupta, R. P. Plasticization-enhanced hydrogen purification using polymeric membranes. *Science* **2006**, *311*, 639-642.

Supporting Information

1. The 4N4H pore structure

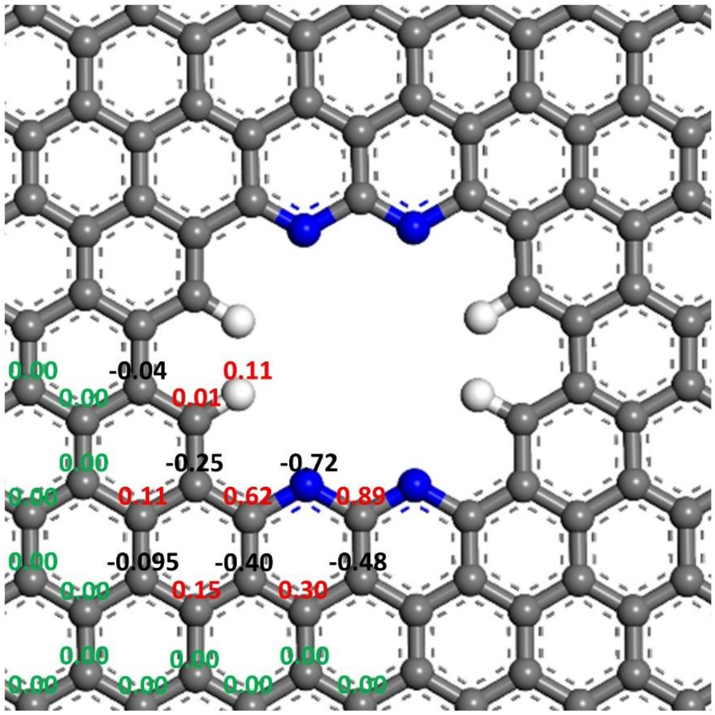

Figure S4-1. The 4N4H pore structure (carbon, grey; nitrogen, blue; hydrogen, white). The partial atomic charges used in our simulations are provided next to each atom. Due to the D2h symmetry of the pore structure, only the atoms in the lower left part are labelled with their atomic charges.

2. Force field parameters

Table S4-1. Lennard-Jones parameters for the porous graphene (atomic charges are in Figure S4-1).

Porous graphene		
	ε (K)	σ (Å)
C	28.0	3.40
N	85.6	3.25
H	15.1	2.42
bonds	length (Å)	
C-C	1.42	
C-N	1.42	
C-H	1.10	

Table S4-2. Force field parameters for gas molecules.

CO_2			
	ε (K)	σ (Å)	q (e)
C	28.129	2.757	0.6512
O	80.507	3.033	-0.3256
bonds	length (Å)		
C-O	1.149		
He			
	ε (K)	σ (Å)	q (e)
He	10.956	2.641	0

3. Exponential fitting

Instead of the linear fitting of the initial portion of the permeation number vs. time curves (Figure 4-2 in the text), here we use an exponential decay model $y = a * (1 - e^{-\lambda t})$ to fit the whole curves (Figure S4-2a,b). For each curve, the fitting yields a λ value; the half-time, $t_{1/2}$, is simply $ln(2)/\lambda$ and the permeation rate is $a/(2t_{1/2})$. Then total flux and flux per pore can be obtained (Figure S4-2c,d). Compared with the linear fitting results (Figure 4-3 in the text), one can see that the two methods give very similar results.

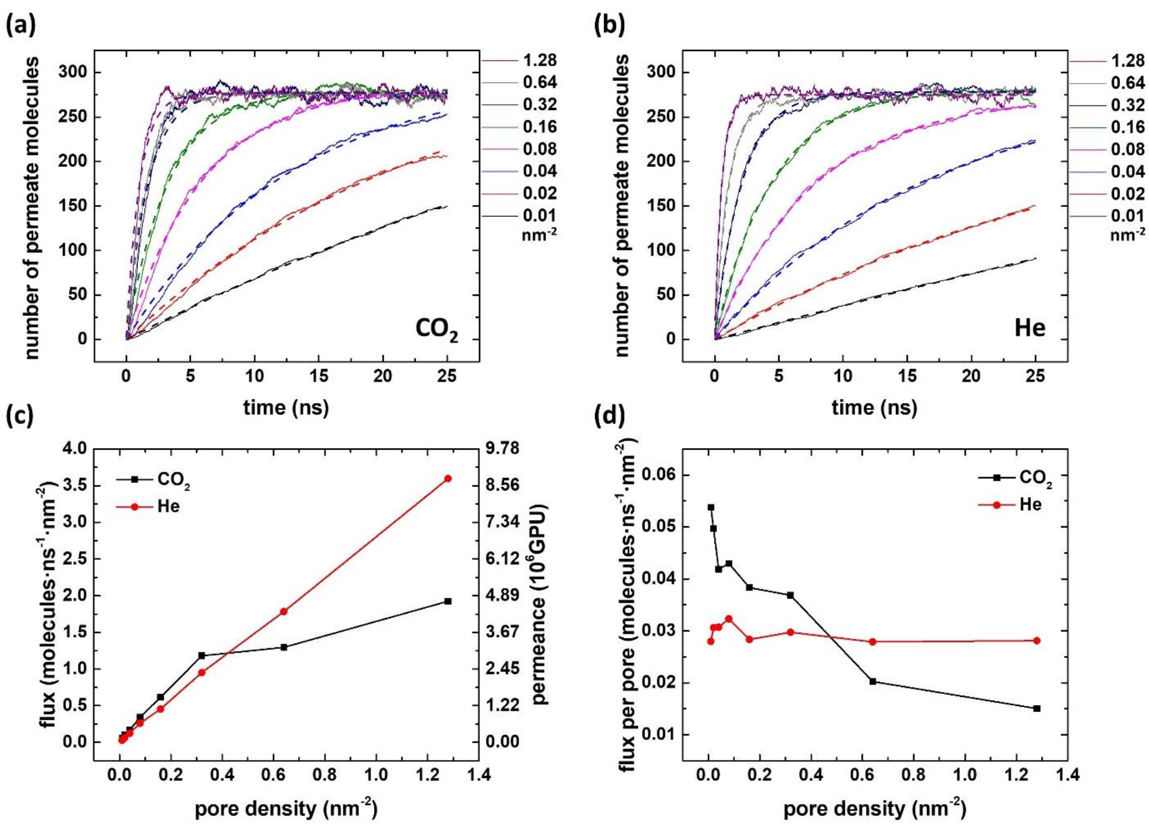

Figure S4-2. The number of gas molecules permeating through the nanoporous graphene membrane with time for different pore densities (from 0.01 to 1.28 nm^{-2}): (a) CO_2; (b) He; Dashed lines represent the exponential decay model fitting. Flux vs pore density of graphene membranes for CO_2 and He permeation: (c) flux and permeance per unit membrane area; (d) flux per pore.

4. Flux for He molecule

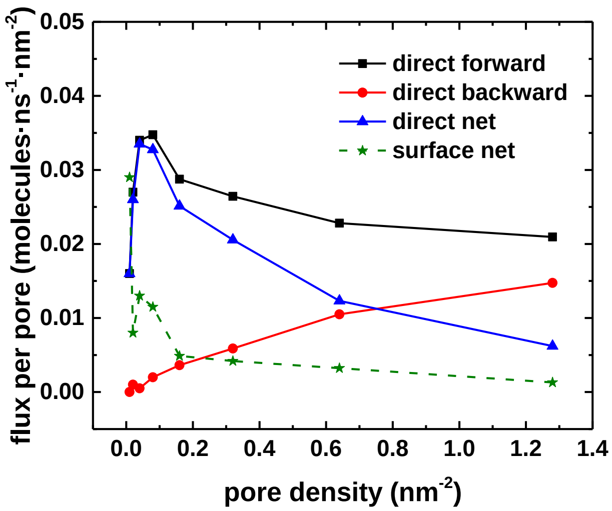

Figure S4-3. The forward, backward, and net direct fluxes, in comparison with the net surface flux of He, across graphene membranes of different pore densities.

Chapter 5. Continuously Tunable Pore Size for Gas Separation via A Bilayer Nanoporous Graphene Membrane

5.1 Abstract

Pore size is a crucial factor impacting gas separation, but it is difficult to control for a single-layer nanoporous graphene membrane. Here we propose a bilayer design of a nanoporous graphene membrane with a continuously tunable effective pore size, by shifting the lateral position of one graphene layer against the other. Molecular dynamics simulations of gas permeation reveal that selective separation of gases such as CO_2, N_2, and CH_4 of 3 to 4 Å in kinetic diameter can be achieved for a bilayer membrane from single-layer pores as large as 25 Å in size. Hence this bilayer design allows both great flexibility of pore sizes in a single layer graphene and continuous variation of the effective pore size at a sub-Å level.

5.2 Introduction

Nanoporous graphene is an important size-selective membrane both conceptually and experimentally.[1-3] With the sub-nanometer pores, it can be used as a one-atom-thin molecular-sieving membrane for separations of gases,[4-8] ions,[9-11] water,[12-14] and isotopes.[15-17] Nanoporous graphene membrane can be also used for DNA sequencing.[18-21]

For gas separation, several factors can influence the performance of nanoporous graphene membrane, including pore shape, pore size, pore density, and functionalization.[22-25] The mechanisms of gas permeation through nanoporous graphene membranes with different pore sizes were explored from molecular simulations.[24, 25] Interesting proposals such as ion gating have been proposed to tune the pore size.[26] Experimentally, it is challenging to precisely control the pore size in a one-atom-thin membrane for gas separation.[3, 27] It is even harder to continuously tune the pore size because of the molecular construction forming the pores that varies non-continuously.[25]

To overcome the above challenges in pore control in 2D membranes, we propose a bilayer nanoporous graphene membrane with continuously tunable pore size. The key idea is to use the lateral shift of the two graphene layers (called offset in this work) to tune the effective pore size continuously. Although bilayer and multilayer membranes have been explored before for gas permeations,[28, 29] these graphene-oxide-based membranes have relative large interlayer spacing (~10 Å) and the main mechanism of permeance control is via modulation of the interlayer gas adsorption.[28] In contrast, the present work focuses on the effect of the offset in the bilayer graphene membrane on the molecular sieving of gases without any interlayer adsorption. We demonstrate the working of such an idea in selective gas permeation of CO_2/CH_4 and N_2/CH_4 by using molecular dynamics simulations.

5.3 Computational Method

MD simulations were performed with the LAMMPS package[36] in the canonical

(NVT) ensemble at 300 K controlled using the Nose-Hoover thermostat.[37, 38] The simulation box of 10×10×20 nm^3 with periodic boundaries in the *xy* directions was divided into two chambers along the *z* direction by the bilayer nanoporous graphene membrane at $z = 0$: the upper chamber (the feed side) was pressurized at 10 bar, while the lower chamber (the permeate side) was vacuum initially. The bilayer nanoporous graphene membrane was fixed during the simulations. We chose a high initial pressure to accelerate our MD simulations, so that sufficient numbers of gas passing-through events could be observed in our simulation time.

The duration of each simulation was 25 ns. The feed pressure was initialized with a certain number of gas molecules in the upper chamber and then it would decrease as gas molecules begin to permeate through the membrane to the lower chamber. To determine gas permeance, we used the first 5-ns permeation data for flux analysis when the pressure difference across the membrane was roughly constant. We have previously shown that this simple approach gives similar permeances as an exponential fitting method.[23] We note that there is a more accurate approach to derive the permeance for the non-equilibrium system.[25, 39, 40] In addition, we are also exploring advanced simulation techniques that can maintain a constant pressure difference across the membrane.[41]

The partial atomic charges of nanoporous graphene were calculated by the Repeating Electrostatic Potential Extracted Atomic charges (REPEAT) method based on

DFT-derived electrostatic potential.[42] The Lennard-Jones (LJ) parameters of carbon atoms in nanoporous graphene sheet were 0.086 kcal/mol for ε and 3.4 Å for σ, while the LJ parameters of hydrogen were 0.015 kcal/mol for ε and 2.45 Å for σ.[26] The force field of gas molecular atoms were taken from previous studies.[26, 43] For CO_2 and N_2, three-site models were adopted, and for methane, all-atom model was used (Table S5-1).[26] The LJ potential parameters were calculated by using Lorentz-Berthelot Combining Rules. The cutoff distance for Lennard-Jones and Coulombic potential was 12 Å. The long ranged electrostatic interaction was calculated using the PPPM method with a kspace slab correction.[44-46]

5.4 Results and discussion

5.4.1 Bilayer design and gas permeation

Since we are tuning the offset of two pores in two overlapping graphene layers, the single pore size can be flexible and large. To demonstrate our idea, we employed a pore with all-hydrogen termination and a size of 5.7 Å (Figure 5-1a). The distance between the two layers of graphene sheets was fixed at 3.4 Å, similar to the layer spacing in graphite,[30] so there is no adsorption between the two layers. Figure 5-1c shows how the offset, which represents the relative position of two layers of graphene sheet in a lateral direction, is continuously tuned. The effective pore size and shape through the bilayer graphene membrane due to the offset can be seen in Figure 5-1b (the white space).

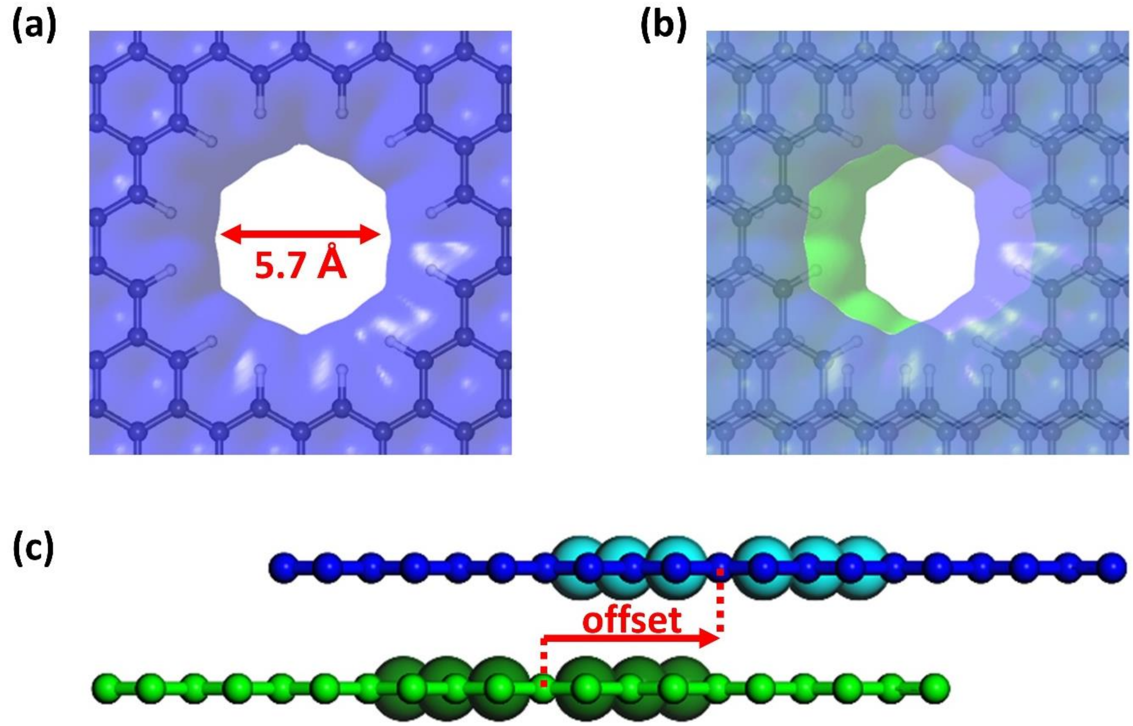

Figure 5-1. Construction of a porous bilayer graphene membrane: (a) the single-layer graphene with a relatively larger pore (5.7 Å in diameter) than the sizes of small gas molecules such as CO_2; (b) the bilayer nanoporous graphene membrane from stacking two single-layer membranes from (a); (c) side view of the bilayer nanoporous graphene membrane. Isosurfaces of electron density are shown in (a) and (b) to define the pore shape; larger spheres in (c) indicate the pore rims.

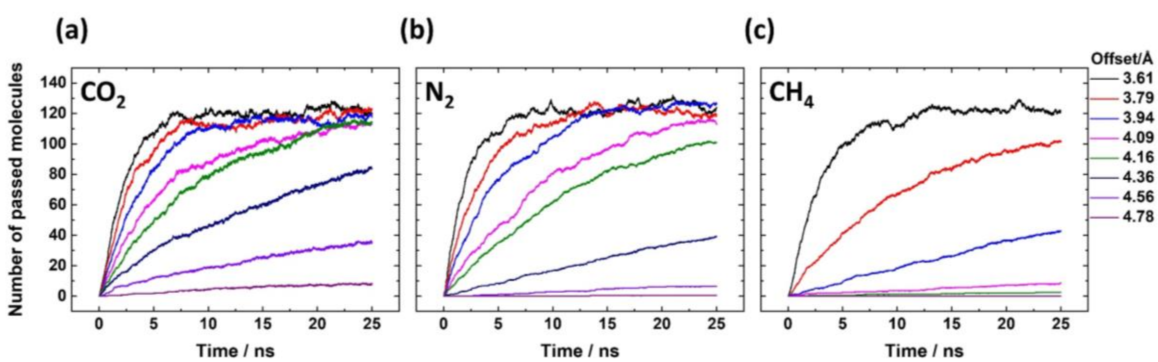

Figure 5-2. The number of gas molecules passing through the bilayer nanoporous graphene membrane vs. time for different offset values between the two single-layer graphene membranes: (a) CO_2, (b) N_2 and (c) CH_4.

To simulate gas permeation through the bilayer membrane, classical molecular dynamics (CMD) simulations were performed via a bi-chamber setup with the membrane in the middle. The feed chamber was pressurized at 10atm initially, while the permeate side started with a vacuum. Since the pore in the single-layer graphene (Figure 5-1a) has a larger size than the kinetic diameters of many small gaseous molecules, such as CO_2, N_2, and CH_4, the single layer porous graphene would not have any selectivity to separate these gases.[26] Hence, the bilayer membrane setup would provide a desirable test to determine whether selective gas permeation can be achieved. Figure 5-2 shows the number of molecules permeating through the bilayer membrane with time for the varying offset values or effective pore sizes. The trends are similar for the three gas molecules simulated. In each case, the number of pass-through gas molecules decreases with the increasing offset, due to the shrinking effective pore size. More interestingly, one can see that for the same offset (that is, same-colored curves in Figure 5-2), the decrease in the number of pass-through gas molecules is much greater for CH_4 than CO_2 and N_2. In other words, at certain offsets, the bilayer graphene membrane began to show selective permeation of CO_2 and N_2 over CH_4.

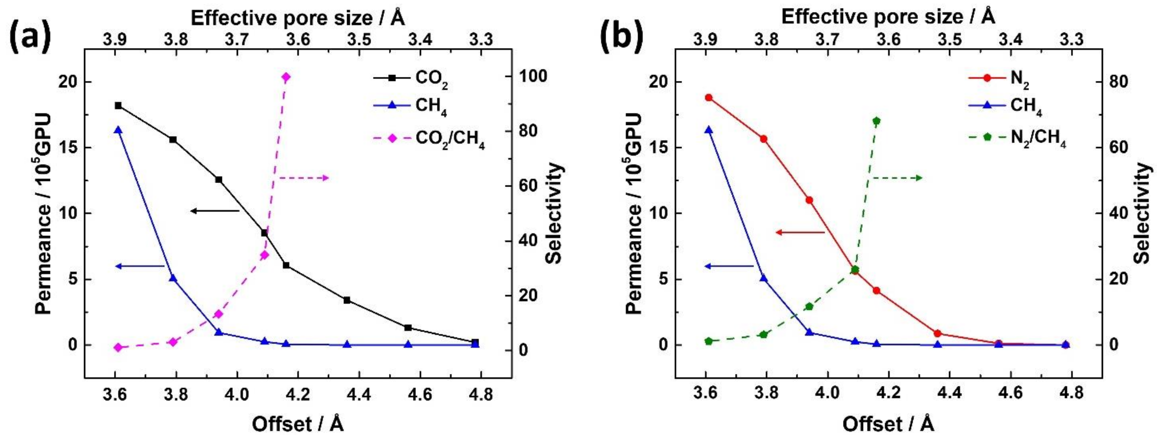

Figure 5-3. Permeance (left axis) and selectivity (right axis) as a function of the offset (bottom axis) or the effective pore size (top axis) in the bilayer nanoporous graphene membranes: (a) CO_2 vs. CH_4; (b) N_2 vs. CH_4.

5.4.2 Permeance and selectivity

To quantify the permeation rate and selectivity as a function of the offset, we chose the first 5-ns permeation data to calculate the permeance and selectivity. In addition, we also defined an effective pore size (see Figure S5-1 in SI) of the bilayer graphene membrane to better understand the control of the overlapping pore area relative to the sizes of the gas molecules. Figure 5-3a shows the permeances of CO_2 and CH_4 (two solid lines, left axis) and the CO_2/CH_4 selectivity (the dashed line, right axis). We can see that the selectivity of CO_2/CH_4 increases as the offset increases or the effective pore size decreases. When the effective pore size is about 3.6 Å, the selectivity achieves 100 with a CO_2 permeance of 6×10^5 GPU.

Further decrease of the effective pore size essentially blocks permeation of CH_4 molecule, leading to much higher selectivity of CO_2/CH_4. Since too small an effective pore size also causes the permeance of CO_2 to decrease, a trade-off between permeance and selectivity suggests that control of the effective pore size between 3.6 and 3.7 Å affords the optimal balance. Likewise for N_2 and CH_4, as shown in Figure 5-3b, when the effective pore size is about 3.6 Å, the selectivity of N_2/CH_4 reaches to 68 while N_2 permeance remains 4×10^5 GPU. Hence, Figure 5-3 has convincingly shown that the effective pore size through a bilayer porous graphene membrane can be continuously tuned for selective gas permeation.

We examined the contributions of adsorption and diffusion to the selectivity. Figure 5-4a shows the coverages of gas molecules on the feed side as a function of the effective pore size, while Figure 5-4b shows the adsorption selectivity. One can see that adsorption selectivity of CO_2/CH_4 varies between 1 and 1.5, while that of N_2/CH_4 between 0.4 and 0.7. In other words, the contribution of adsorption to the high selectivities shown in Figure 5-3 is negligible, so the diffusion selectivity is the key factor. Figure 5-4b also shows that adsorption selectivities of N_2/CH_4 and CO_2/CH_4 have a minimum at offset ~ 4.0 Å. This can be understood from Figure 5-4a: both CO_2 and N_2 adsorption amounts increase with the offset, but CH_4 adsorption amount has a maximum at offset ~ 4.0 Å, so the adsorption selectivities of N_2/CH_4 and CO_2/CH_4 as a ratio of the adsorption amount show a minimum at offset ~ 4.0 Å.

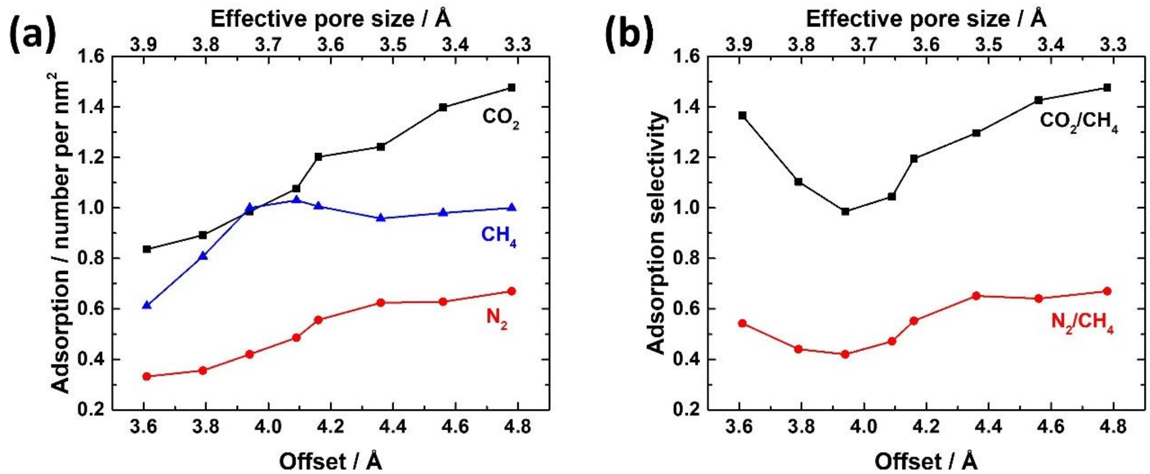

Figure 5-4. Adsorption amount of CO_2, N_2 and CH_4 on the feed side (a) and adsorption selectivities of CO_2/CH_4 and N_2/CH_4 (b) as a function of the offset (bottom axis) or the effective pore size (top axis) in the bilayer nanoporous graphene membranes.

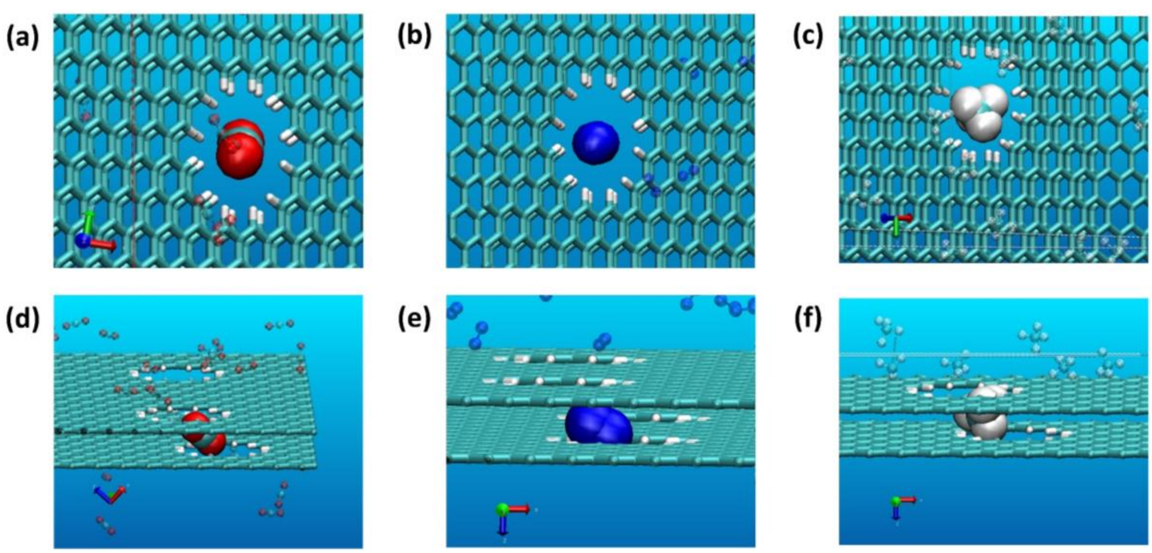

Figure 5-5. Snapshots of passing-through events of gas molecules: (a) and (d) CO_2; (b) and (e) N_2; (c) and (f) CH_4. Upper pane, top view; lower panel, side view.

As previously used for understanding gas permeation through the microporous carbon molecular sieve membrane,[31, 32] the diffusion selectivity can be decomposed into energetic selectivity and entropic selectivity.[33] Due to their smaller sizes,[34] CO_2 and N_2 diffusions are favored energetically (that is, they have lower diffusion barriers) than CH_4. Moreover, they are also favored in the entropic selectivity which is related to the partition functions in both the adsorbed state before permeation and the transition state in the pore.[33] For the linear gas molecules such as CO_2 and N_2, they pass along the pore channel by orienting their molecular axis along the line connecting the two pore centers, as shown in Figure 5-5a,d for CO_2 and Figure 5-5b,e for N_2. In contrast, the CH_4 molecule is more tightly held in the transition state (Figure 5-5c,f).

5.4.3 Entropic effect

Although CH_4 is more spherical, its kinetic dimeter is larger, so it can only struggle through the nanopore and will lose all three rotational degrees of freedom in the transition state. On the other hand, the linear molecules such as N_2 and CO_2 are thinner than CH_4. So, they still keep one of their two rotational degree of freedom in the transition state. The elliptic-cylinder shape of the composite pore of the bilayer membrane also facilitates the rotation of N_2 and CO_2, leading to higher entropy selectivity (more degrees of freedom at the transition state, leading to a lower free energy of permeation). O_2 is even thinner than N_2, so when the pore size is controlled properly to be between the kinetic diameters of O_2 and N_2, N_2 will lose all two rotational degrees of freedom, while O_2 can maintain one, leading to a higher O_2/N_2 selectivity due to the entropy different at the transition state.[33]

There are both similarities and differences regarding the mechanism of selective gas separation between the single-layer graphene and the bilayer graphene. Gas permeation through both types of membranes involve adsorption and diffusion and the selectivity is mainly dictated by the (effective) pore size. But the difference in pore shape does have a significant impact on permselectivity: the single-layer porous graphene has a disk-like pore shape, while the bilayer porous graphene with a small effective pore size has an elliptic-cylinder shape. This difference in the pore shape has an impact on the motion of the gas molecule in the transition state. This entropic-selectivity difference will be fully addressed in next chapter.

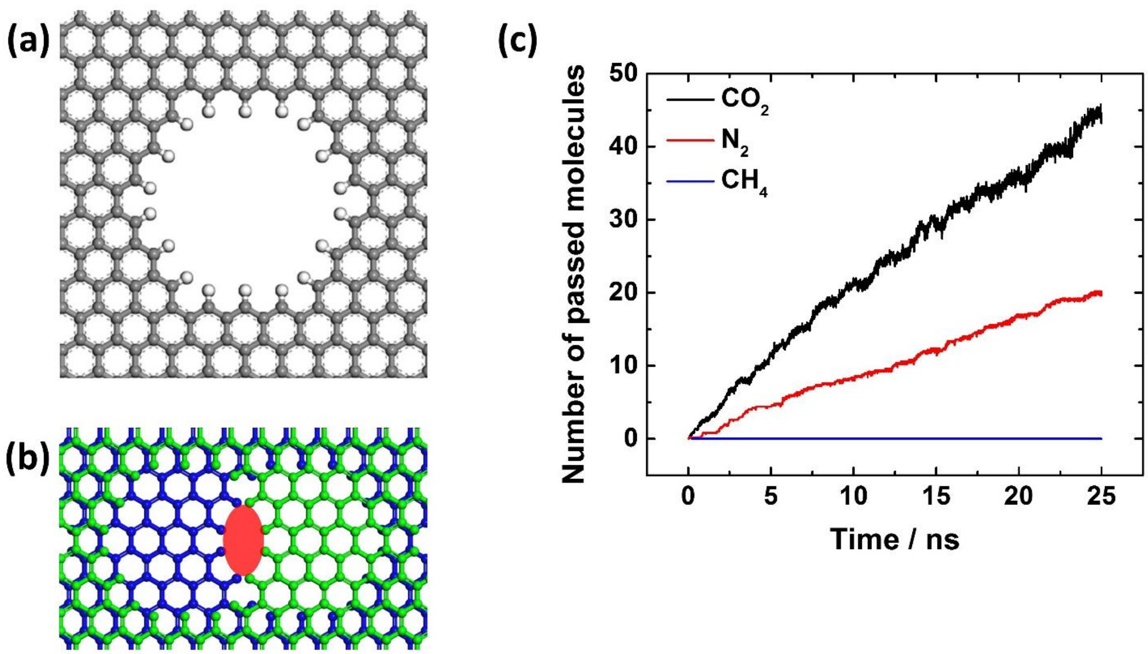

Figure 5-6. Bilayer membranes with pore size of 10.4 Å. (a) Structure of the graphene sheet with pore size of 10.4 Å; (b) the bilayer graphene membrane from two single-layer membranes from (a) at an offset of 9.3 Å (red oval represents the effective pore dimensions, ~3.6 Å in width); (c) permeation of CO_2, N_2 and CH_4 with time through the bilayer graphene membrane in (b).

5.4.4 Bilayer membranes with larger pores in the single layer

Having demonstrated that selective gas separation can be achieved for a bilayer graphene membrane with a pore size of 5.7 Å in a single graphene layer, we next explore the flexibility in the pore size. In other words, we want to show that the continuously tunable effective pore size can be achieved for offsetting very large pores in a bilayer graphene membrane. We first tested a pore size of 10.4 Å (Figure 5-6a) and tuned the offset such that the effective pore size is about 3.6 Å (Figure 5-6b). As shown in Figure 5-6c, highly selective CO_2/CH_4 and N_2/CH_4 permeation can be seen. We further tested a pore as large as 25.2 Å (Figure 5-7a), which is in the mesopore range. Again, at the effective pore size of 3.6 Å (Figure 5-7b), selective CO_2/CH_4 and N_2/CH_4 permeations can be achieved (Figure 5-7c).

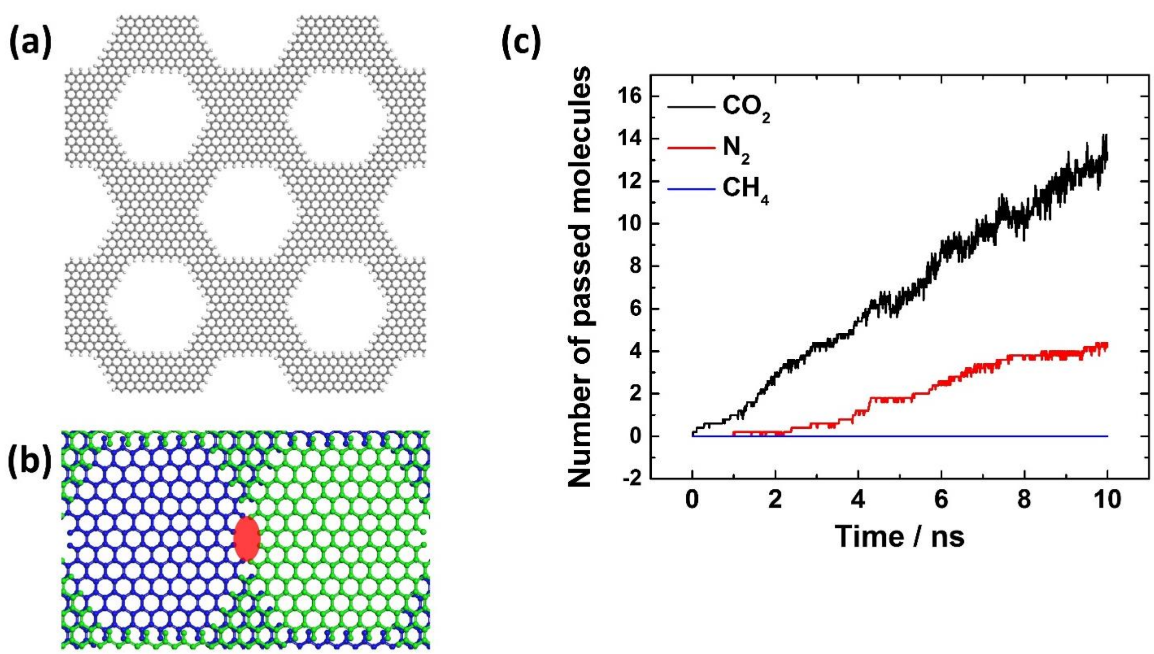

Figure 5-7. Bilayer membranes with pore size of 25.2 Å. (a) Structure of the graphene sheet with pore size of 25.2 Å; (b) the bilayer graphene membrane from two single-layer membranes from (a) at an offset of 24.0 Å (red oval represents the effective pore dimensions; ~3.6 Å in width); (c) permeation of CO_2, N_2 and CH_4 with time through the bilayer graphene membrane in (b).

We further estimated the gas permeances for the two bilayer porous graphene membranes. For the membrane in Figure 5-6, average permeances are 1.18×10^5 GPU for CO_2 and 0.47×10^5 GPU for N_2. For the membrane in Figure 5-7, average permeances are 0.67×10^5 GPU for CO_2 and 0.13×10^5 GPU for N_2. For CH_4, no permeation through these two bilayer porous graphene membranes has been observed in the simulation time scale, so the permeances of CH_4 are too slow to allow a reliable determination of the very high selectivities of CO_2/CH_4 and N_2/CH_4 in these two membranes.

5.4.5 Implications

In current work, we considered only the overlapping of two single-layer pores to form a single composite pore in the bilayer membrane. For large-scale bilayer membranes, there would be many such composite pores and it would be challenging to maintain uniform offsets among the different composite pores. To alleviate this difficulty, we think that the key is to make sure that the single-layer porous graphene membrane has an ordered array of the same-sized pores as in a two-dimensional covalent-organic framework. It is encouraging that great progress toward the bottom-up synthesis of such porous graphene has been made recently.[27]

To experimentally realize the desired offset of one graphene layer against the other, it would be challenging to have just only one bilayer membrane and then try to vary its offset. Instead, we suggest that one prepare many parallel, random samples of porous graphene bilayer membranes stabilized by the van der Waals interaction and with different offsets and then transfer them on a porous support (such as carbon) for characterization of the offset and test of membrane performance. To prepare such bilayer membranes, we suggest two strategies. First, one can simply stack one porous-graphene layer to another one. Recently, great progress has been made in bottom-up synthesis of single-layer porous graphene.[27] The second strategy is to fold a porous single-layer porous graphene into a bilayer. Ruoff and coworkers reported the folded graphene film by using a tailored substrate having a hydrophobic region and a hydrophilic region.[35]

5.5 Summary and conclusions

In summary, we have designed bilayer nanoporous graphene membranes with continuously tunable effective pore size. Using classical molecular dynamics (MD) simulations, we showed that the effective pore size can be tuned in the bilayer membranes to achieve selective CO_2/CH_4 and N_2/CH_4 separations while CO_2 or N_2 permeance remains on the order of 10^5 GPU. We further showed that the bilayer membrane can utilize pores as large as 25.2 Å in the single layer to achieve selective gas separations.

Compared with single-layer porous graphene, the bilayer porous graphene makes the effective pore size continuously tunable, allows the use of much larger graphene pores, and creates a unique and variable pore shape that allows one to explore more permeation mechanisms such as entropic selectivity in addition to molecular sieving that dominates the permeation through the single-layer porous graphene. Hence, our work suggests a promising direction to achieve advanced control in pore sizes and permeation mechanisms for selective gas separations via the ultrathin membranes.

References

(1) Tang, Q.; Zhou, Z.; Chen, Z. Graphene-Related Nanomaterials: Tuning Properties by Functionalization. *Nanoscale* **2013,** *5*, 4541-4583.

(2) Schrier, J. Fluorinated and Nanoporous Graphene Materials as Sorbents for Gas Separations. *ACS Appl. Mater. Inter.* **2011,** *3*, 4451-4458.

(3) Koenig, S. P.; Wang, L. D.; Pellegrino, J.; Bunch, J. S. Selective Molecular Sieving through Porous Graphene. *Nat. Nanotechnol.* **2012,** *7*, 728-732.

(4) Gadipelli, S.; Guo, Z. X. Graphene-Based Materials: Synthesis and Gas Sorption, Storage and Separation. *Prog. Mater. Sci.* **2015,** *69*, 1-60.

(5) Liu, G. P.; Jin, W. Q.; Xu, N. P. Graphene-Based Membranes. *Chem. Soc. Rev.* **2015,** *44*, 5016-5030.

(6) Tian, Z. Q.; Dai, S.; Jiang, D. E. What Can Molecular Simulation Do for Global Warming? *WIREs Comput. Mol. Sci.* **2016,** *6*, 173-197.

(7) Li, Y.; Zhou, Z.; Shen, P.; Chen, Z. Two-Dimensional Polyphenylene: Experimentally Available Porous Graphene as a Hydrogen Purification Membrane. *Chem. Commun.* **2010,** *46*, 3672-3674.

(8) Schrier, J. Helium Separation Using Porous Graphene Membranes. *J. Phys. Chem. Lett.* **2010,** *1*, 2284-2287.

(9) Sint, K.; Wang, B.; Kral, P. Selective Ion Passage through Functionalized Graphene Nanopores. *J. Am. Chem. Soc.* **2008,** *130*, 16448-16449.

(10) Hu, G. H.; Mao, M.; Ghosal, S. Ion Transport through a Graphene Nanopore. *Nanotechnology* **2012,** *23*, 395501.

(11) Ji, A. P.; Li, Z. W.; Yang, H. J.; He, P. Y.; Chen, Y. F. Transport of Water and Ions through a Graphene Nanopore in an Electric Field. *Biophys. J.* **2017,** *112*, 544a.

(12) Suk, M. E.; Aluru, N. R. Water Transport through Ultrathin Graphene. *J. Phys. Chem. Lett.* **2010,** *1*, 1590-1594.

(13) Cohen-Tanugi, D.; Grossman, J. C. Water Desalination across Nanoporous Graphene. *Nano Lett.* **2012,** *12*, 3602-3608.

(14) Surwade, S. P.; Smirnov, S. N.; Vlassiouk, I. V.; Unocic, R. R.; Veith, G. M.; Dai, S.; Mahurin, S. M. Water Desalination Using Nanoporous Single-Layer Graphene. *Nat. Nanotechnol.* **2015,** *10*, 459-464.

(15) Hauser, A. W.; Schrier, J.; Schwerdtfeger, P. Helium Tunneling through Nitrogen-Functionalized Graphene Pores: Pressure- and Temperature-Driven Approaches to Isotope Separation. *J. Phys. Chem. C* **2012,** *116*, 10819-10827.

(16) Hauser, A. W.; Schwerdtfeger, P. Nanoporous Graphene Membranes for Efficient $^3He/^4He$ Separation. *J. Phys. Chem. Lett.* **2012,** *3*, 209-213.

(17) Hankel, M.; Jiao, Y.; Du, A.; Gray, S. K.; Smith, S. C. Asymmetrically Decorated, Doped Porous Graphene as an Effective Membrane for Hydrogen Isotope Separation. *J. Phys. Chem. C* **2012,** *116*, 6672-6676.

(18) Merchant, C. A.; Healy, K.; Wanunu, M.; Ray, V.; Peterman, N.; Bartel, J.; Fischbein, M. D.; Venta, K.; Luo, Z. T.; Johnson, A. T. C.; Drndic, M. DNA Translocation through Graphene Nanopores. *Nano Lett.* **2010,** *10*, 2915-2921.

(19) Schneider, G. F.; Kowalczyk, S. W.; Calado, V. E.; Pandraud, G.; Zandbergen, H. W.; Vandersypen, L. M. K.; Dekker, C. DNA Translocation through Graphene Nanopores. *Nano Lett.* **2010,** *10*, 3163-3167.

(20) Avdoshenko, S. M.; Nozaki, D.; da Rocha, C. G.; Gonzalez, J. W.; Lee, M. H.; Gutierrez, R.; Cuniberti, G. Dynamic and Electronic Transport Properties of DNA Translocation through Graphene Nanopores. *Nano Lett.* **2013,** *13*, 1969-1976.

(21) Kulkarni, M.; Mukherjee, A. Ionic Liquid Prolongs DNA Translocation through Graphene Nanopores. *Rsc Adv.* **2016,** *6*, 46019-46029.

(22) You, Y.; Deng, J.; Tan, X.; Gorjizadeh, N.; Yoshimura, M.; Smith, S.; Sahajwalla, V.; Joshi, R. On the Mechanism of Gas Adsorption for Pristine, Defective and Functionalized Graphene. *Phys. Chem. Chem. Phys.* **2017,** *19*, 6051-6056.

(23) Wang, S.; Tian, Z.; Dai, S.; Jiang, D. E. Effect of Pore Density on Gas Permeation through Nanoporous Graphene Membranes. *Nanoscale* **2018,** *10*, 14660-14666.

(24) Drahushuk, L. W.; Strano, M. S. Mechanisms of Gas Permeation through Single Layer Graphene Membranes. *Langmuir* **2012,** *28*, 16671-16678.

(25) Sun, C. Z.; Boutilier, M. S. H.; Au, H.; Poesio, P.; Bai, B. F.; Karnik, R.; Hadjiconstantinou, N. G. Mechanisms of Molecular Permeation through Nanoporous Graphene Membranes. *Langmuir* **2014,** *30*, 675-682.

(26) Tian, Z. Q.; Mahurin, S. M.; Dai, S.; Jiang, D. E. Ion-Gated Gas Separation through Porous Graphene. *Nano Lett.* **2017,** *17*, 1802-1807.

(27) Moreno, C.; Vilas-Varela, M.; Kretz, B.; Garcia-Lekue, A.; Costache, M. V.; Paradinas, M.; Panighel, M.; Ceballos, G.; Valenzuela, S. O.; Pena, D.; Mugarza, A. Bottom-up Synthesis of Multifunctional Nanoporous Graphene. *Science* **2018,** *360*, 199-203.

(28) Liu, Q.; Gupta, K. M.; Xu, Q.; Liu, G.; Jin, W. Gas Permeation through Double-Layer Graphene Oxide Membranes: The Role of Interlayer Distance and Pore Offset. *Sep. Purif. Technol.* **2019,** *209*, 419-425.

(29) Wang, P.; Li, W.; Du, C.; Zheng, X.; Sun, X.; Yan, Y.; Zhang, J. CO_2/N_2 Separation Via Multilayer Nanoslit Graphene Oxide Membranes: Molecular Dynamics Simulation Study. *Comp. Mater. Sci.* **2017,** *140*, 284-289.

(30) Kim, T. H.; Jeon, E. K.; Ko, Y.; Jang, B. Y.; Kim, B. S.; Song, H. K. Enlarging the D-Spacing of Graphite and Polarizing Its Surface Charge for Driving Lithium Ions Fast. *J. Mater. Chem. A* **2014,** *2*, 7600-7605.

(31) Singh, A.; Koros, W. Significance of Entropic Selectivity for Advanced Gas Separation Membranes. *Ind. Eng. Chem. Res.* **1996,** *35*, 1231-1234.

(32) Ning, X.; Koros, W. J. Carbon Molecular Sieve Membranes Derived from Matrimid® Polyimide for Nitrogen/Methane Separation. *Carbon* **2014,** *66*, 511-522.

(33) Koros, W. J.; Zhang, C. Materials for Next-Generation Molecularly Selective Synthetic Membranes. *Nat. Mater.* **2017,** *16*, 289-297.

(34) Mehio, N.; Dai, S.; Jiang, D. E. Quantum Mechanical Basis for Kinetic Diameters of Small Gaseous Molecules. *J. Phys. Chem. A* **2014,** *118*, 1150-1154.

(35) Wang, B.; Huang, M.; Kim, N. Y.; Cunning, B. V.; Huang, Y.; Qu, D. S.; Chen, X. J.; Jin, S.; Biswal, M.; Zhang, X.; Lee, S. H.; Lim, H.; Yoo, W. J.; Lee, Z.; Ruoff, R. S. Controlled Folding of Single Crystal Graphene. *Nano Lett.* **2017,** *17*, 1467-1473.

(36) Plimpton, S. Fast Parallel Algorithms for Short-Range Molecular-Dynamics. *J. Comput. Phys.* **1995,** *117*, 1-19.

(37) Nose, S. A Unified Formulation of the Constant Temperature Molecular-Dynamics Methods. *J. Chem. Phys.* **1984,** *81*, 511-519.

(38) Hoover, W. G. Canonical Dynamics: Equilibrium Phase-Space Distributions. *Phys. Rev. A* **1985,** *31*, 1695-1697.

(39) Sun, C.; Bai, B. Molecular Sieving through a Graphene Nanopore: Non-Equilibrium Molecular Dynamics Simulation. *Science bulletin* **2017,** *62*, 554-562.

(40) Sun, C.; Bai, B. Improved CO_2/CH_4 Separation Performance in Negatively Charged Nanoporous Graphene Membranes. *J. Phys. Chem. C* **2018,** *122*, 6178-6185.

(41) Ozcan, A.; Perego, C.; Salvalaglio, M.; Parrinello, M.; Yazaydin, O. Concentration Gradient Driven Molecular Dynamics: A New Method for Simulations of Membrane Permeation and Separation. *Chem. Sci.* **2017,** *8*, 3858-3865.

(42) Campana, C.; Mussard, B.; Woo, T. K. Electrostatic Potential Derived Atomic Charges for Periodic Systems Using a Modified Error Functional. *J. Chem. Theory. Comput.* **2009,** *5*, 2866-2878.

(43) Liu, H. J.; Dai, S.; Jiang, D. E. Insights into CO_2/N_2 Separation through Nanoporous Graphene from Molecular Dynamics. *Nanoscale* **2013,** *5*, 9984-9987.

(44) Yeh, I. C.; Berkowitz, M. L. Ewald Summation for Systems with Slab Geometry. *J. Chem. Phys.* **1999,** *111*, 3155-3162.

(45) Ballenegger, V.; Arnold, A.; Cerda, J. J. Simulations of Non-Neutral Slab Systems with Long-Range Electrostatic Interactions in Two-Dimensional Periodic Boundary Conditions. *J. Chem. Phys.* **2009,** *131*, 094107.

(46) Hockney, R. W.; Eastwood, J. W. *Computer Simulation Using Particles*. CRC Press: **1988**.

Supporting Information

Table S5-1. Force field parameters for gas molecules

CO_2			
	ε (K)	σ (Å)	q (e)
C	28.129	2.757	0.6512
O	80.507	3.033	-0.3256
bonds	length (Å)		
C-O	1.149		
N_2			
	ε (K)	σ (Å)	q (e)
N	36.4	3.318	-0.4048
COM	0	0	0.8096
bonds	length (Å)		
N-N	1.098		
CH_4			
	ε (K)	σ (Å)	q (e)
C	33.23	3.500	-0.2400
H	15.1	2.500	0.0600
bonds	length (Å)		
C-H	1.087		

Definition of effective pore size

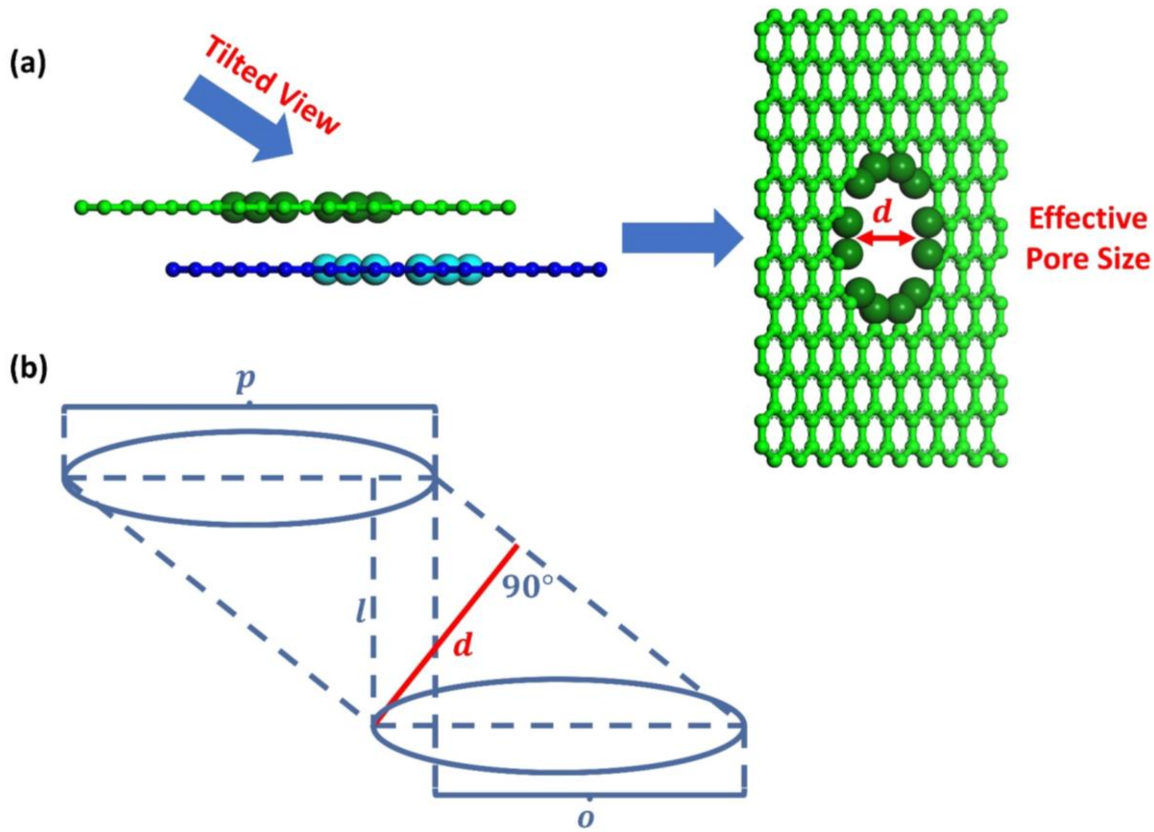

Figure S5-1. (a) Side view and tilted view of bilayer nanoporous graphene membrane; (b) Schematic of cross section of pore (5.7 Å).

As shown in Figure S5-1a, if we look at the membrane in tilted view angle, the short shaft of the elliptical pore is defined as effective pore size, which can be calculated by mathematic formula. Figure S5-1b is a schematic of cross section of the pore, the effective pore size (d) can be expressed as:

$$d = \frac{l}{\sqrt{l^2 + o^2}} \times p$$

where l is the interlayer distance, o is the offset, p is the original pore size. When l

and p are fixed, the offset is the only parameter affecting effective pore size. Table S5-2 shows eight numbers of offset used in this work and corresponding effective pore sizes.

Table S5-2. Eight numbers of offset used in this work and corresponding effective pore sizes.

p = 5.7 Å, l = 3.4 Å								
o/Å	3.61	3.79	3.94	4.09	4.16	4.36	4.56	4.78
d/Å	3.90	3.80	3.72	3.64	3.60	3.50	3.40	3.30

Chapter 6. Entropic Selectivity in Air Separation via a Bilayer Nanoporous Graphene Membrane

6.1 Abstract

Membranes are an energy-efficient technology for air separation, but it is difficult to control the pore size to separate N_2 and O_2 due to their similar kinetic diameters. Here we demonstrate from molecular dynamics simulations that a bilayer nanoporous graphene membrane with continuously tunable pore sizes by the offset between the two graphene layers can achieve O_2/N_2 selectivity up to 26 with a permeance over 10^5 GPU. We find that the entropic selectivity is the main reason behind the high selectivity via the tumbling movement of the skinnier and shorter O_2 molecules entering and passing through the elliptic-cylinder-shaped nanopore of the bilayer membrane. Such motion is absent in the single-layer graphene membrane with a similar-sized and similar-shaped pore which yields an O_2/N_2 selectivity of only 6 via molecular sieving alone. Hence the bilayer nanoporous graphene membrane provides a novel way to enhance entropic selectivity for gas separation via control of both the pore size and the 3D pore shape.

6.2 Introduction

Pure oxygen is widely used in medical, chemical, and material applications. Pure nitrogen is also important as a feedstock in ammonia synthesis, an inert atmosphere, or a coolant. Hence, air separation is paramount for many industrial and medical uses. Conventionally, large-scale oxygen/nitrogen production by air separation is performed by the energy-intensive cryogenic distillation process.[1-3] For small to medium scales, other technologies such as pressure-swing-adsorption and membranes are also employed.[4-8]

Membrane technologies can provide a more energy-efficient alternative for air separation.[4, 8] An increasing number of membrane materials have been synthesized, such as polymers, zeolites, inorganic ceramic materials, carbon molecular sieves (CMS), and metal-organic frameworks (MOFs).[9-14] There is a well-known trade-off between membrane selectivity and membrane permeability, called the Robeson upper bound.[10, 15, 16] To surpass the upper bound, various approaches have been suggested for next-generation molecularly selective synthetic membranes, for example, using advanced semi-rigid polymers, hybrid materials, or scalable molecular sieves.[14]

One-atom-thin membranes such as porous graphene offers an attractive feature of ultra-high permeance and selectivity for gas separations based on molecule sieving.[17-22] However, due to the similar kinetic diameters of N_2 (3.64 Å) and O_2 (3.46 Å) and the discontinuously varying pore size on the graphene sheet, high O_2/N_2 selectivity is hard to achieve via the monolayer nanoporous graphene membranes. It is well known that the kinetic selectivity favors O_2 over N_2 in carbon molecular sieves via the ultra-micropore windows.[10] The selectivity has been attributed to an entropic factor that favors a smaller molecule at the transition state, while the diffusion motion of the larger molecule is hindered.

Given the increasing interest in graphene and other 2D membranes for molecular and ion transport,[23, 24] we wonders if the entropic selectivity of O_2/N_2 can be achieved by a nanoporous graphene membrane. To address this question, we perform classical molecular dynamics (CMD) simulations and show that high nanoporous entropic selectivity of O_2/N_2 can be achieved via O_2 tumbling through a bilayer nanoporous graphene membrane. Below we first explain our simulation methods and then show our membrane design and performance. This is followed by the explanation and analysis of the selectivity mechanism and then the implications of our results and main conclusions.

6.3 Computational Method

Classical molecular dynamics (CMD) simulations were performed with the LAMMPS package[25] in the canonical (NVT) ensemble at 300 K via the Nose-Hoover thermostat.[26, 27] The simulation box of $10\times10\times20$ nm^3 with periodic boundaries in the *xy* directions was divided into two chambers along the *z* direction by the bilayer nanoporous graphene membrane at $z = 0$: the feed side was pressurized at 10 bar, while the permeate side was vacuum initially. Single-component or pure-gas permeance was simulated; the feed pressure was initialized by randomly placing a certain number of pure gas molecules in the feed side to yield a pressure of 10 bar according to the ideal-gas law. The duration of each simulation was 10 ns; the number of molecules in the permeate side, as the number of molecules crossed net that of crossed back, was counted every 10 ps. The bilayer nanoporous graphene membrane was fixed during the simulations. The force-field parameters for the membrane (consisting of carbon and hydrogen atoms only) were given in ESI. For O_2 and N_2, three-site models were adopted.[28] The LJ potential parameters were calculated by using Lorentz-Berthelot Combining Rules. The cutoff distance for Lennard-Jones and Coulombic potential was 12 Å. The long ranged electrostatic interaction was calculated using the PPPM method with a k-space slab correction.[29-31] Free-energy profiles were calculated via the umbrella sampling method implemented in the PLUMED tool.[32] The weighted histogram analysis method (WHAM) was applied to reconstruct the free energy profile.[33]

6.4 Results and discussion

6.4.1 Membrane setup

Bilayer nanoporous graphene membranes provide an effective way to continuously tune the pore size at sub-angstrom resolution via the offset between the two one-atom-thin membranes.[34] It also offers a knob to control the diffusion path through the bilayer membrane. Figure 6-1a shows the single-layer porous graphene used to build the bilayer. It has an all-hydrogen-terminated pore of 5.7 Å in size which is much greater than the sizes of O_2 and N_2 (Figure 6-1d). So the single-layer membrane would not have any O_2/N_2

selectivity (that is, it is close to 1). The bilayer membrane is then constructed with an interlayer spacing of 3.4 Å (similar that in graphite) between the two porous single-layer graphene membranes (Figure 6-1b), so there is no adsorption between the two layers (the accessible pore size in between the layers is hence zero). The offset (Figure 6-1c) can be tuned to control the effective pore size of the bilayer membrane for gas permeation.

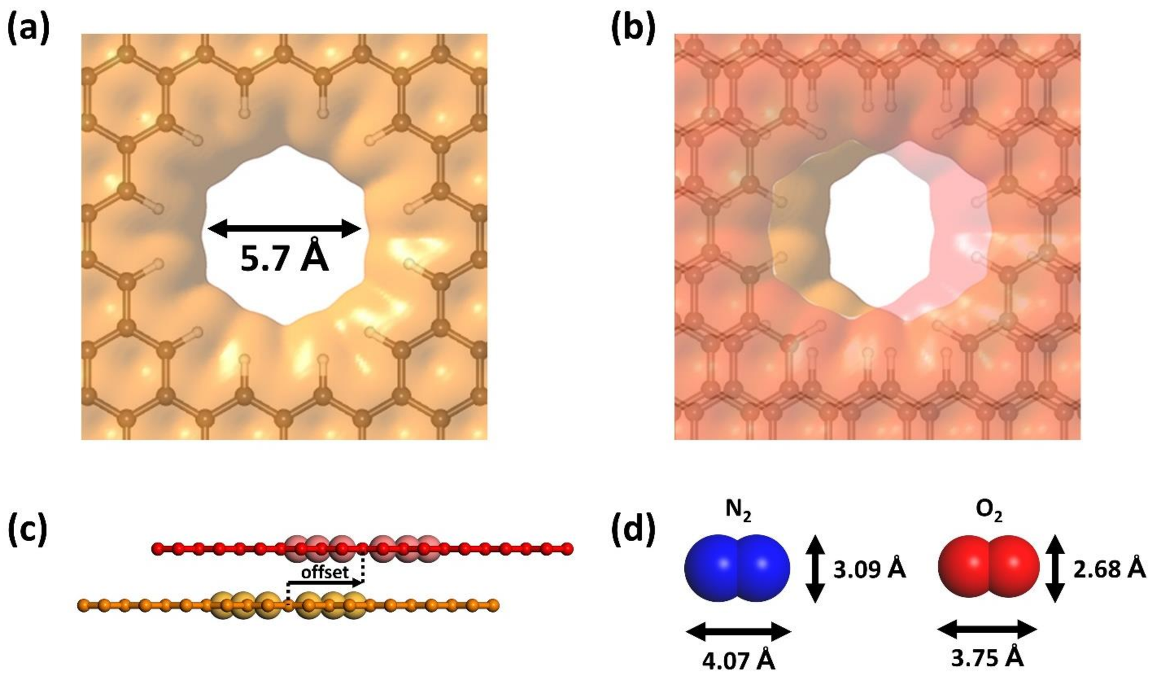

Figure 6-1. Construction of a porous bilayer graphene membrane: (a) Single-layer graphene pore; (b) bilayer nanoporous graphene membrane; (c) side view of the bilayer nanoporous graphene membrane with an offset of the two pore centers (the larger spheres indicate the pore rims); (d) molecular sizes of nitrogen and oxygen. In (a) and (b), the pore shapes and sizes are estimated by the isosurfaces of electron density at 0.0004 e/a_0^3.

6.4.2 O_2/N_2 permeation through the bilayer membrane

The bilayer membrane was then placed in the middle of a bi-chamber system where the upper chamber was pressurized at 10 bar with either O_2 or N_2 and the lower was vacuum.

Then classical molecular dynamics simulations were performed to follow the trajectories of the gas molecules. Figure 6-2 shows the number of gas molecules (N_2 or O_2) permeating through the bilayer membrane with time for different effective pore sizes. The effective size is determined by a simple analytical relationship with the offset (Figure S6-1; ESI). When the effective pore size is 3.60 Å (Figure 6-2a), both of N_2 and O_2 have high permeances. When the effective pore size decreases to 3.50 Å (Figure 6-2b), N_2 permeance is significantly reduced while O_2 permeance decrease only slightly, indicating an increase in O_2/N_2 selectivity. When the effective pore size further decreases to 3.45 Å (Figure 6-2c), N_2 permeance is greatly reduced, because now the pore size is much less than the N_2 kinetic dimeter (3.64 Å) but still comparable to O_2 kinetic diameter (3.46 Å). When the effective pore size further decreases to 3.40 Å (Figure 6-2d), now O_2 permeance is also greatly reduced. Figure 6-2 suggests that an effective pore size of 3.45 Å would be optimal for O_2/N_2 selectivity and O_2 permeance.

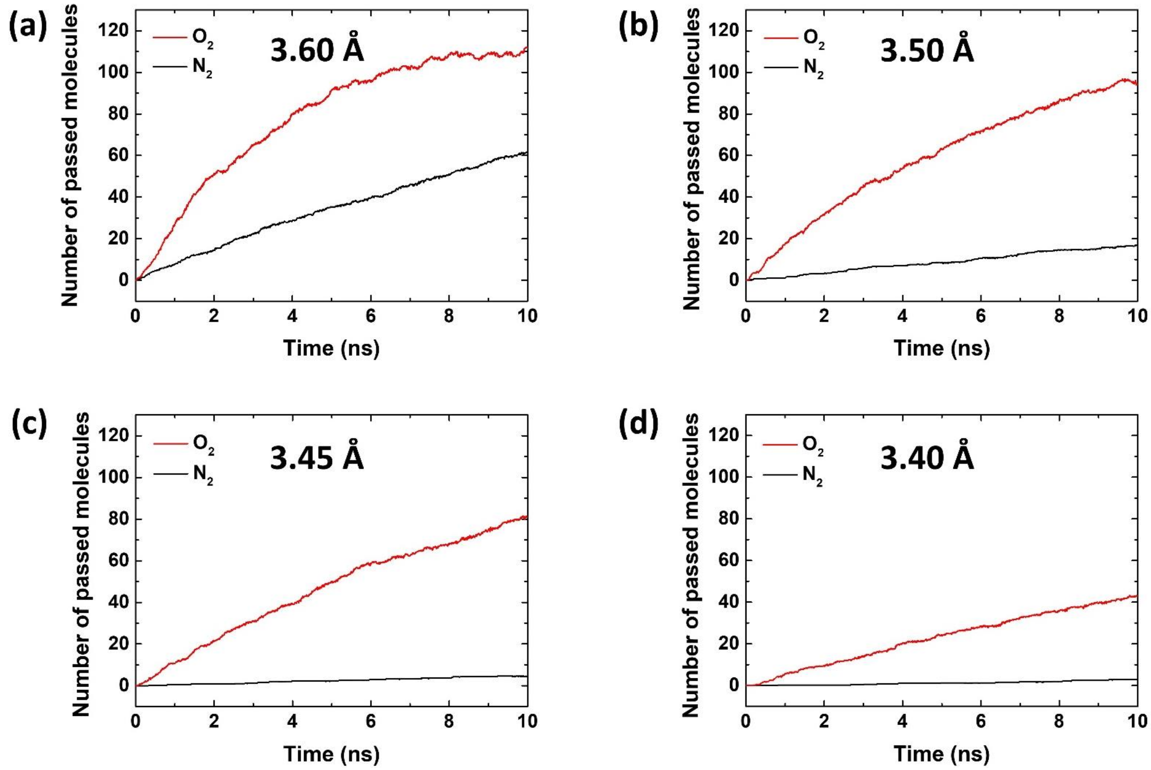

Figure 6-2. The numbers of gas molecules passed through the bilayer nanoporous graphene membranes with different effective pore sizes: (a) 3.60 Å; (b) 3.50 Å; (c) 3.45 Å; (d) 3.40 Å.

6.4.3 O_2/N_2 selectivity

To analyze the relationship between the O_2/N_2 selectivity and the effective pore size, we first fitted the curves in Figure 6-2 via an exponential model, $y = a * (1 - e^{-\lambda t})$,[35] to obtain the fitting parameter a and λ whose product is proportional to the permeance. Figure 6-3 shows how O_2 and N_2 permeances and O_2/N_2 permselectivity vary with the effective pore size. One can see that the effective pore size of 3.45 Å affords the highest selectivity of 25.6, while the O_2 permeance is at 5×10^5 GPU (gas permeation unit). For comparison, carbon molecular sieve (CMS) membranes show O_2/N_2 selectivity of 8 – 25.[13,]

[36] So the bilayer nanoporous graphene membrane with the optimal effective pore size rivals the best CMS membranes in terms of O_2/N_2 selectivity.

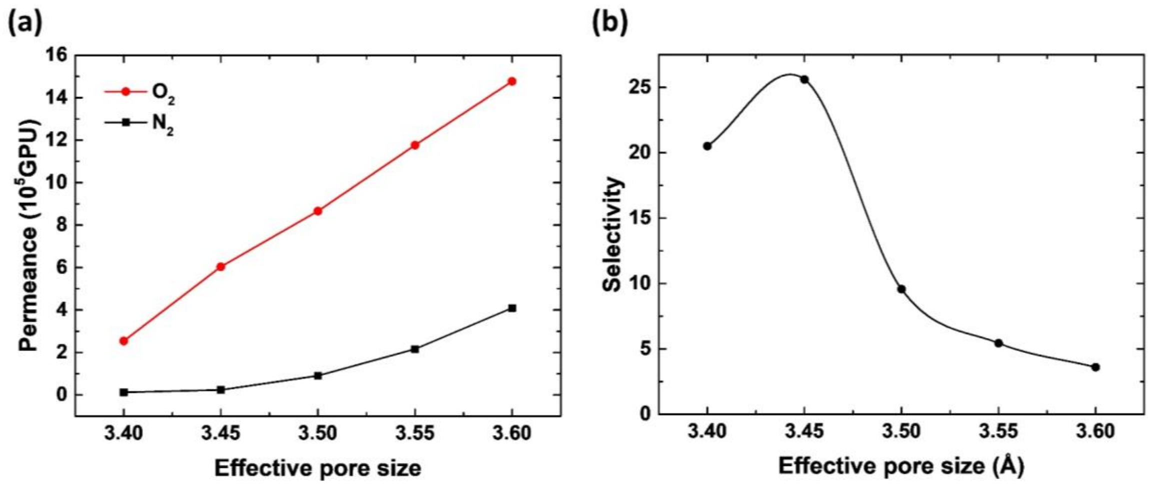

Figure 6-3. O_2 and N_2 permeances (a) and O_2/N_2 permselectivity (b) of the bilayer nanoporous graphene membranes with different effective pore sizes.

6.4.4 Mechanism of O_2/N_2 separation

For ultrathin membranes such as porous graphene, gas permeation usually consists of two main steps: adsorption on the surface of the feed side and diffusion across the membrane.[14, 37] To determine which step dictates the selectivity, we analyze them separately. Figure 6-4 shows that the coverages of N_2 and O_2 on the feed side with time for the bilayer membrane with the optimal effective pore size of 3.45 Å. One can see that both gases reach their maximum coverages very quickly (< 1 ns). Then O_2 coverage slightly decreases, while N_2 coverage fluctuates. After 4 ns, O_2 and N_2 coverages are close to each other and in fact N_2 coverage is slightly higher, so the adsorption selectivity is close 1, which means that O_2/N_2 permselectivity is dictated by the diffusion process.

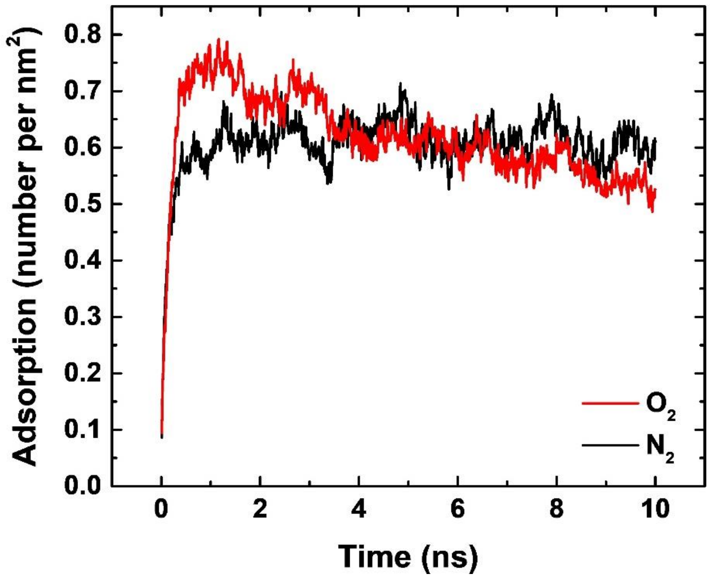

Figure 6-4. Adsorption amount on the feed site of the bilayer nanoporous graphene membrane (effective pore size at 3.45 Å) with time.

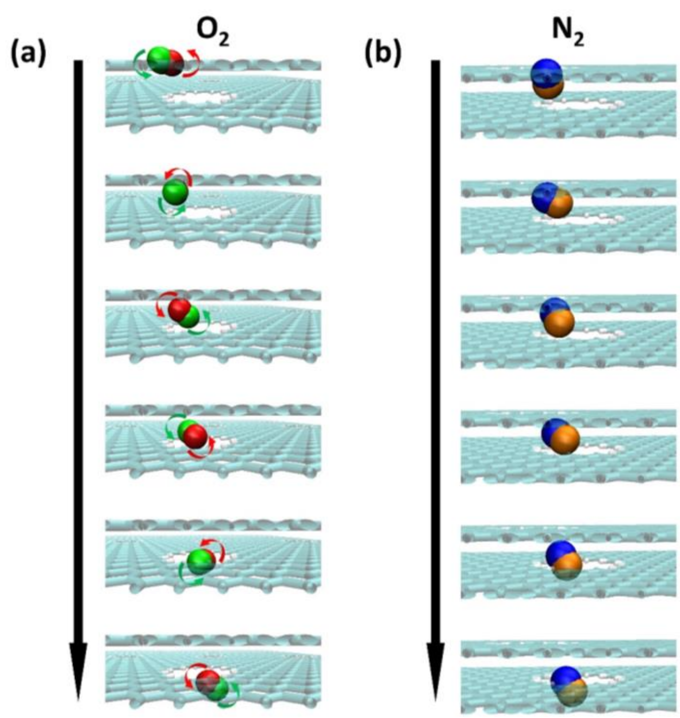

Figure 6-5. Snapshots of (a) O_2 and (b) N_2 passing through bilayer nanoporous graphene membrane with effective pore size of 3.45 Å.

To understand how the bilayer membrane modulates the diffusion process and hence yields the high O_2/N_2 selectivity, we tracked and analyzed the motions of O_2 and N_2 molecules passing through the membrane. As shown in Figure 6-5, the skinnier and shorter O_2 molecule tumbles through the elliptical-shaped nanopore (Figure 6-5a), while the longer and fatter N_2 molecule wiggles through the nanopore with the rotational degrees of freedom hindered (Figure 6-5b). Hence the unique elliptical-shaped nanopore in the bilayer graphene greatly facilitates the tumbling of O_2.

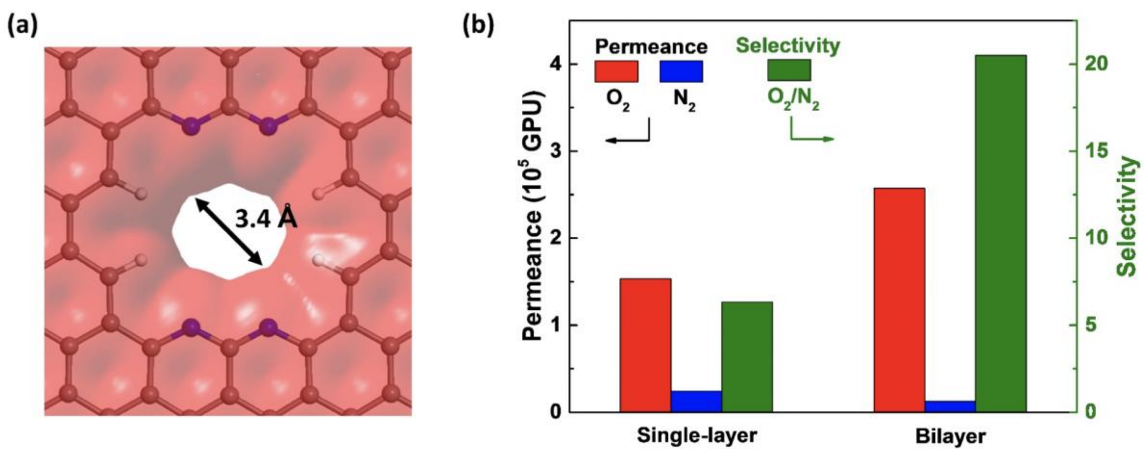

Figure 6-6. Comparison between single-layer and bilayer graphene membrane. (a) A single-layer porous graphene membrane with a pore of an elliptic shape and an average pore size of 3.4 Å. (b) Comparison of O_2 and N_2 permeances as well as O_2/N_2 selectivity between a single-layer graphene with a pore size of 3.4 Å and the bilayer graphene membrane with an effective pore size of 3.4 Å.

To further show that the distinct difference of this bilayer-graphene nanopore from the single-layer graphene pore, we also simulated O_2/N_2 separation through a single-layer graphene pore with an elliptic shape and an average pore size of 3.4 Å (Figure 6-6a). As shown in Figure 6-6b, in comparison with the performances of the bilayer graphene membrane of the similar pore size, the O_2 permeance becomes lower while the N_2 permeance becomes higher through the single-layer membrane, leading to a lower O_2/N_2 selectivity of 7. Further analysis of the trajectories confirmed that there is no tumbling motion for either O_2 or N_2 in passing through the single-layer membrane. In other words, the size-sieving effect of the single-layer membrane achieves O_2/N_2 selectivity of 7, while the additional entropic effect via the tumbling of the O_2 molecule through the bilayer membrane increases the selectivity by two times.

Figures 6-5 and 6-6 clearly indicate that it is the entropic effect that yields the high O_2/N_2 selectivity through the bilayer graphene membrane, due to the extra unconstrained rotational degrees of freedom that O_2 enjoys at the transition state. To quantify this entropic difference, the umbrella sampling method was applied to determine the free-energy profiles of permeation for N_2 and O_2 through the bilayer membrane (Figure 6-6). The two porous graphene layers are at $z = \pm 1.7$ Å. For both O_2 and N_2, the transition state is at the middle of the bilayer ($z = 0$), with the free energy barrier of 5.08 kcal/mol for N_2 permeation and 3.18 kcal/mol for O_2. Then, we apply the transition-state theory. The free-energy-barrier difference would yield an O_2/N_2 selectivity of 24.5, which is consistent with the selectivity of 25.6 from CMD simulations. The 1.9 kcal/mol difference between N_2 and O_2 at the transition state should mainly result from the entropy contribution, because a simple estimate of the entropy difference from the partition functions would yield a contribution to the free energy at 1.7 kcal/mol at room temperature (see ESI).

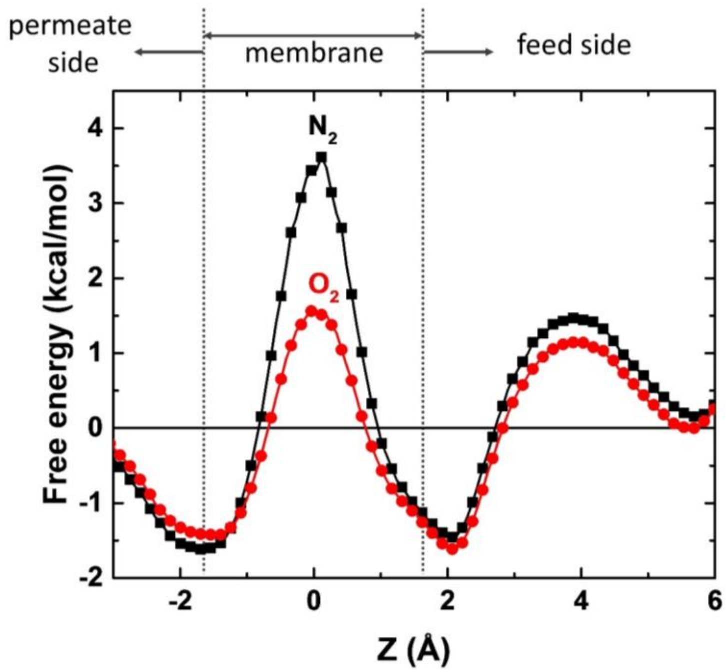

Figure 6-7. Free energy profiles of gas-permeation through the bilayer nanoporous graphene membrane (effective pore size at 3.45 Å) for N_2 and O_2.

To further show the favorable entropic selectivity in the bilayer graphene membrane, we simulated the temperature effect on the selectivity whereby a more favorable entropy contribution would yield a higher selectivity at a higher temperature. As shown in Figure 6-8, the O_2/N_2 selectivity through the bilayer membrane increases from 273 K to 300K, while it stays about the same for the single-layer membrane during the same temperature range.

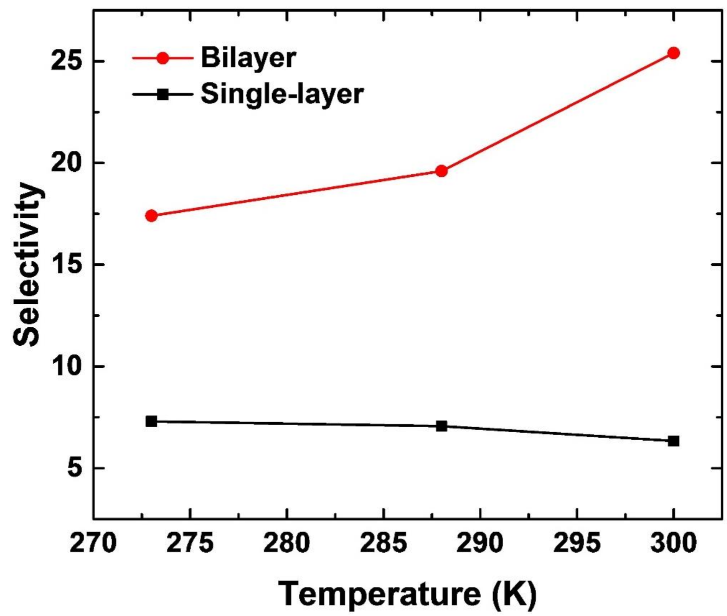

Figure 6-8. Change of O_2/N_2 selectivity with temperature for single-layer and bilayer nanoporous graphene membranes.

6.4.5 Comparison of air-separation performances with available materials

Although our bilayer porous graphene membranes are still a design concept to be realized experimentally, it is still informative to compare with available materials in the literature for their air-separation performances, to show the distinctive features of the bilayer porous graphene membranes. Figure 6-9 shows that the bilayer porous graphene membranes have much higher permeances because of their sub-nanometer thickness, way beyond the upper bound.[16] More important, by obtaining the entropic selectivity via controlling the effective pore size, the bilayer porous graphene membranes can achieve higher O_2/N_2 selectivity, rivaling those of carbon-based mixed matrix membranes and carbon-molecular-sieve (CMS) membranes.

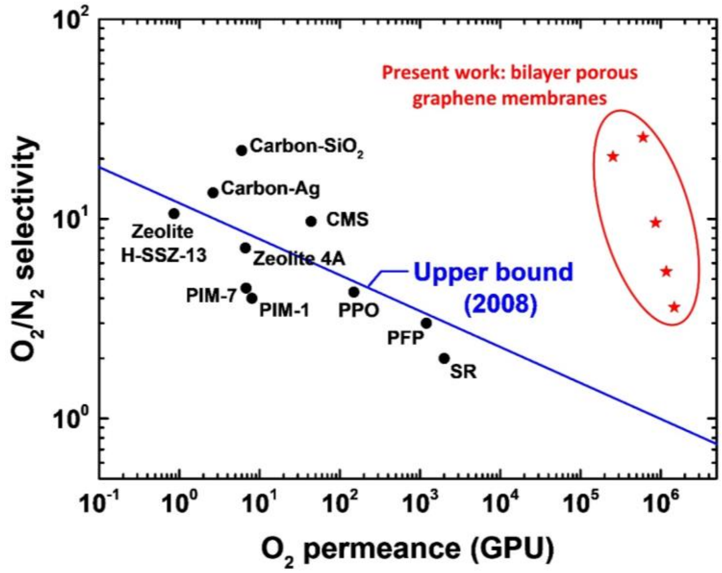

Figure 6-9. Comparison of bilayer porous graphene membranes to other membranes for O_2/N_2 separation.[8, 38] The upper bound for polymer membranes is plotted with an assumed 1 μm-thick selective layer.[38] CMS: carbon molecular sieve; PPO: poly(phenylene oxide); PFP: perfluoropolymer; SR: silicone rubber.

The bilayer design is not limited to graphene membranes and could also be extended to 2D covalent-organic frameworks (COFs) and MOFs. To experimentally realize such design, we propose to first prepare a single-layer membrane with uniform pore sizes. There has been great progress recently in bottom-up synthesis of single-layer porous graphene.[39] More excitingly, 2D COFs[40] and MOFs[41, 42] have also been created by exfoliation. Once such a 2D membrane with uniform pores is available, one can stack such two layers together randomly to create the bilayer membranes with different offsets, or one can fold it into a bilayer, as experimentally demonstrated recently.[43]

6.5 Summary and conclusions

In summary, we have demonstrated by classical molecular dynamics simulations that bilayer nanoporous graphene membranes with a proper effective pore size can achieve an O_2/N_2 selectivity as high as 26, while maintaining an O_2 permeance above 10^5 GPU. By tracking the trajectories of gas-permeation events, we found that the high O_2/N_2 permselectivity is mainly contributed by the extra tumbling motion of O_2 molecules through the elliptical-shaped pore. Both transition-state theory analysis, simulated free-energy profiles, and temperature-dependent permeation confirm this entropic contribution to the selectivity. Our work hence shows that the bilayer nanoporous graphene membrane is effective for air separation and could be potentially useful for other separations by enhancing entropic selectivity.

References

(1) Castle, W. Air separation and liquefaction: Recent developments and prospects for the beginning of the new millennium. *Int. J. Refrig.* **2002**, *25*, 158-172.

(2) Burdyny, T.; Struchtrup, H. Hybrid membrane/cryogenic separation of oxygen from air for use in the oxy-fuel process. *Energy* **2010**, *35*, 1884-1897.

(3) Zhu, Y.; Legg, S.; Laird, C. D. Optimal design of cryogenic air separation columns under uncertainty. *Comput. Chem. Eng.* **2010**, *34*, 1377-1384.

(4) Murali, R. S.; Sankarshana, T.; Sridhar, S. Air separation by polymer-based membrane technology. *Sep. Purif. Rev.* **2013**, *42*, 130-186.

(5) Smith, A.; Klosek, J. A review of air separation technologies and their integration with energy conversion processes. *Fuel Process. Technol.* **2001**, *70*, 115-134.

(6) Singh-Ghosal, A.; Koros, W. Air separation properties of flat sheet homogeneous pyrolytic carbon membranes. *J. Membr. Sci.* **2000**, *174*, 177-188.

(7) Baker, R. W. Future directions of membrane gas separation technology. *Ind. Eng. Chem. Res.* **2002**, *41*, 1393-1411.

(8) Bernardo, P.; Drioli, E.; Golemme, G. Membrane gas separation: A review/state of the art. *Ind. Eng. Chem. Res.* **2009**, *48*, 4638-4663.

(9) Yong, W. F.; Li, F. Y.; Xiao, Y. C.; Chung, T. S.; Tong, Y. W. High performance pim-1/matrimid hollow fiber membranes for CO_2/CH_4, O_2/N_2 and CO_2/N_2 separation. *J. Membr. Sci.* **2013**, *443*, 156-169.

(10) Singh, A.; Koros, W. Significance of entropic selectivity for advanced gas separation membranes. *Ind. Eng. Chem. Res.* **1996**, *35*, 1231-1234.

(11) Reid, C.; O'koy, I.; Thomas, K. Adsorption of gases on carbon molecular sieves used for air separation. Spherical adsorptives as probes for kinetic selectivity. *Langmuir* **1998**, *14*, 2415-2425.

(12) Wesołowski, R. P.; Terzyk, A. P. Dynamics of effusive and diffusive gas separation on pillared graphene. *Phys. Chem. Chem. Phys.* **2016**, *18*, 17018-17023.

(13) Reid, C.; Thomas, K. Adsorption of gases on a carbon molecular sieve used for air separation: Linear adsorptives as probes for kinetic selectivity. *Langmuir* **1999**, *15*, 3206-3218.

(14) Koros, W. J.; Zhang, C. Materials for next-generation molecularly selective synthetic membranes. *Nat. Mater.* **2017**, *16*, 289-297.

(15) Robeson, L. M. Correlation of separation factor versus permeability for polymeric membranes. *J. Membr. Sci.* **1991**, *62*, 165-185.

(16) Robeson, L. M. The upper bound revisited. *J. Membr. Sci.* **2008**, *320*, 390-400.

(17) Wesołowski, R. P.; Terzyk, A. P. Pillared graphene as a gas separation membrane. *Phys. Chem. Chem. Phys.* **2011**, *13*, 17027-17029.

(18) Jiang, D.-e.; Cooper, V. R.; Dai, S. Porous graphene as the ultimate membrane for gas separation. *Nano Lett.* **2009**, *9*, 4019-4024.

(19) Jiao, Y.; Du, A.; Hankel, M.; Smith, S. C. Modelling carbon membranes for gas and isotope separation. *Phys. Chem. Chem. Phys.* **2013**, *15*, 4832-4843.

(20) Koenig, S. P.; Wang, L.; Pellegrino, J.; Bunch, J. S. Selective molecular sieving through porous graphene. *Nat. Nanotechnol.* **2012**, *7*, 728-732.

(21) Tang, Q.; Zhou, Z.; Chen, Z. Graphene-related nanomaterials: Tuning properties by functionalization. *Nanoscale* **2013**, *5*, 4541-4583.

(22) Liu, H.; Dai, S.; Jiang, D.-e. Insights into CO_2/N_2 separation through nanoporous graphene from molecular dynamics. *Nanoscale* **2013**, *5*, 9984-9987.

(23) Dahanayaka, M.; Liu, B.; Hu, Z.; Pei, Q.-X.; Chen, Z.; Law, A. W.-K.; Zhou, K. Graphene membranes with nanoslits for seawater desalination via forward osmosis. *Phys. Chem. Chem. Phys.* **2017**, *19*, 30551-30561.

(24) Raghav, N.; Chakraborty, S.; Maiti, P. K. Molecular mechanism of water permeation in a helium impermeable graphene and graphene oxide membrane. *Phys. Chem. Chem. Phys.* **2015**, *17*, 20557-20562.

(25) Plimpton, S. Fast parallel algorithms for short-range molecular dynamics. *J. Comput. Phys.* **1995**, *117*, 1-19.

(26) Nosé, S. A unified formulation of the constant temperature molecular dynamics methods. *J. Chem. Phys.* **1984**, *81*, 511-519.

(27) Hoover, W. G. Canonical dynamics: Equilibrium phase-space distributions. *Phys. Rev. A* **1985**, *31*, 1695-1697.

(28) Sun, Y.; Han, S. Diffusion of N_2, O_2, H_2S and SO_2 in mfi and 4A zeolites by molecular dynamics simulations. *Mol. Simulat.* **2015**, *41*, 1095-1109.

(29) Hockney, R. W.; Eastwood, J. W. *Computer simulation using particles*; CRC Press, 1988.

(30) Yeh, I.-C.; Berkowitz, M. L. Ewald summation for systems with slab geometry. *J. Chem. Phys.* **1999**, *111*, 3155-3162.

(31) Ballenegger, V.; Arnold, A.; Cerda, J. Simulations of non-neutral slab systems with long-range electrostatic interactions in two-dimensional periodic boundary conditions. *J. Chem. Phys.* **2009**, *131*, 094107.

(32) Bonomi, M.; Branduardi, D.; Bussi, G.; Camilloni, C.; Provasi, D.; Raiteri, P.; Donadio, D.; Marinelli, F.; Pietrucci, F.; Broglia, R. A. Plumed: A portable plugin for free-energy calculations with molecular dynamics. *Comput. Phys. Commun.* **2009**, *180*, 1961-1972.

(33) Kumar, S.; Rosenberg, J. M.; Bouzida, D.; Swendsen, R. H.; Kollman, P. A. Multidimensional free-energy calculations using the weighted histogram analysis method. *J. Comput. Chem.* **1995**, *16*, 1339-1350.

(34) Wang, S.; Dai, S.; Jiang, D.-e. Continuously tunable pore size for gas separation via a bilayer nanoporous graphene membrane. *ACS Appl. Nano Mater.* **2019**, *2*, 379-384.

(35) Sun, C.; Bai, B. Improved CO_2/CH_4 separation performance in negatively charged nanoporous graphene membranes. *J. Phys. Chem. C* **2018**, *122*, 6178-6185.

(36) Himma, N. F.; Wardani, A. K.; Prasetya, N.; Aryanti, P. T.; Wenten, I. G. Recent progress and challenges in membrane-based O_2/N_2 separation. *Rev. Chem. Eng.* **2018**, *20170094*, 2191-0235.

(37) Sun, C. Z.; Boutilier, M. S. H.; Au, H.; Poesio, P.; Bai, B. F.; Karnik, R.; Hadjiconstantinou, N. G. Mechanisms of molecular permeation through nanoporous graphene membranes. *Langmuir* **2014**, *30*, 675-682.

(38) Lin, H.; Zhou, M.; Ly, J.; Vu, J.; Wijmans, J. G.; Merkel, T. C.; Jin, J.; Haldeman, A.; Wagener, E. H.; Rue, D. Membrane-based oxygen-enriched combustion. *Ind. Eng. Chem. Res.* **2013**, *52*, 10820-10834.

(39) Moreno, C.; Vilas-Varela, M.; Kretz, B.; Garcia-Lekue, A.; Costache, M. V.; Paradinas, M.; Panighel, M.; Ceballos, G.; Valenzuela, S. O.; Peña, D. Bottom-up synthesis of multifunctional nanoporous graphene. *Science* **2018**, *360*, 199-203.

(40) Peng, Y.; Huang, Y.; Zhu, Y.; Chen, B.; Wang, L.; Lai, Z.; Zhang, Z.; Zhao, M.; Tan, C.; Yang, N. Ultrathin two-dimensional covalent organic framework nanosheets: Preparation and application in highly sensitive and selective DNA detection. *J. Am. Chem. Soc.* **2017**, *139*, 8698-8704.

(41) Peng, Y.; Li, Y.; Ban, Y.; Jin, H.; Jiao, W.; Liu, X.; Yang, W. Metal-organic framework nanosheets as building blocks for molecular sieving membranes. *Science* **2014**, *346*, 1356-1359.

(42) Peng, Y.; Li, Y.; Ban, Y.; Yang, W. Two-dimensional metal–organic framework nanosheets for membrane-based gas separation. *Angew. Chem. Int. Ed.* **2017**, *56*, 9757-9761.

(43) Wang, B.; Huang, M.; Kim, N. Y.; Cunning, B. V.; Huang, Y.; Qu, D.; Chen, X.; Jin, S.; Biswal, M.; Zhang, X. Controlled folding of single crystal graphene. *Nano Lett.* **2017**, *17*, 1467-1473.

Supporting Information

1. Definition of the effective pore size (d)

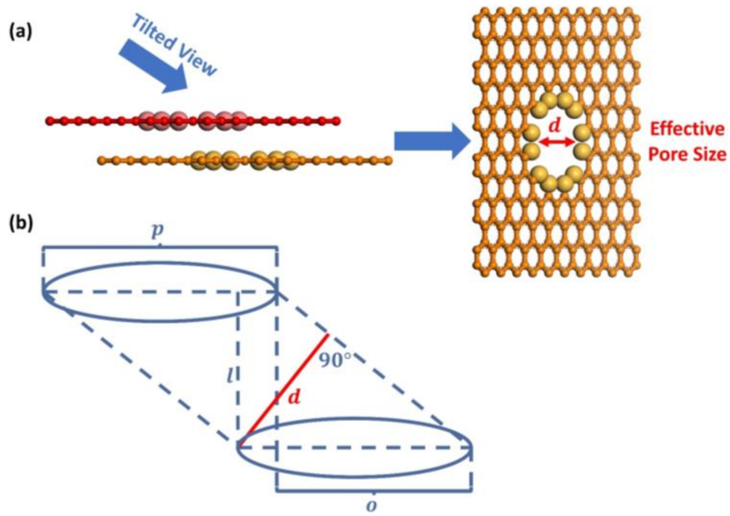

Figure S6-1. (a) Side view and tilted view of bilayer nanoporous graphene membrane; (b) Schematic of cross section of pore (5.7 Å).

$$d = \frac{l}{\sqrt{l^2 + o^2}} \times p$$

l: the interlayer distance;

o: is the offset

p: single-layer pore size.

Table S6-1. Five numbers of offset used in this work and corresponding effective pore sizes.

p = 5.7 Å, l = 3.4 Å					
o/Å	4.16	4.26	4.36	4.46	4.56
d/Å	3.60	3.55	3.50	3.45	3.40

2. Calculation of entropic selectivity

According to transition state theory of diffusion,[1, 2] the O_2/N_2 entropic diffusion selectivity can be written as:

$$\left(\frac{D_{O_2}}{D_{N_2}}\right)_{entropic} = \exp\left(\frac{S_{D,O_2} - S_{D,N_2}}{R}\right) = \frac{(F^{\neq}/F)_{O_2}}{(F^{\neq}/F)_{N_2}}$$

where D is diffusion, S is entropy, F is partition function for normal state, and $F^{\neq}$ is partition function for transition state. The partition function includes translational, rotational, and vibrational contributions, as shown below:

$$F = F_{trans} \cdot F_{rot} \cdot F_{vib},\ F_{trans} = \left(\frac{2\pi mkT}{h^2}\right)^{n/2} a^n, \quad F_{rot} = \left(\frac{T}{\sigma\theta_r}\right)^{n/2},\ F_{vib} = \left[\frac{\exp\left(-\frac{\theta_v}{2T}\right)}{1-\exp\left(-\frac{\theta_v}{T}\right)}\right]^n$$

where n is degree of freedom, m is mass of molecule, k is Boltzmann constant, h is Planck constant, a is cavity length (which is the difference between gas molecular width and the elliptical pore size[2]), σ is symmetry number of gas molecule, θ_r is characteristic rotational temperature, θ_v is characteristic vibrational temperature. In the transition state, all two rotational degrees of freedom of N_2 is suppressed, while O_2 still keeps one unconstrained rotational degrees of freedom. And in the transition state, both of N_2 and O_2 are believed to only have two translational degrees of freedom, since the factor $\frac{kT}{h}$ accounts for the translational degree of freedom in the direction of gas diffusion. The vibrational degrees of freedom of N_2 and O_2 are unrestricted in both normal and transitional state.[1] Thus, the vibrational partition functions are cancelled out. Table S6-2 shows the parameters used in calculations. According to these functions and parameters, the O_2/N_2 entropy difference is 5.67 cal/K and entropic diffusion selectivity is 17.3 at 300 K.

Table S6-2. Parameters used in entropic selectivity calculation when effective pore size of 3.45 Å[1,2]

	O_2	N_2
a for normal state / Å	100	100
a for transition state / Å	0.77 for short axis 2.85 for long axis	0.36 for short axis 2.01 for long axis
σ	2	2
θ_r	2.07	2.88

3. Force field parameters

3.1. Gas molecules

Table S6-3. Force field parameters for gas molecules[3]

O_2			
	ε (kcal/mol)	σ (Å)	q (e)
O	0.108	3.050	-0.1120
COM	0	0	0.2240
bonds	length (Å)		
O-O	1.21		
N_2			
	ε (K)	σ (Å)	q (e)
N	0.0728	3.318	-0.4048
COM	0	0	0.8096
bonds	length (Å)		
N-N	1.098		

3.2. Porous graphene

Table S6-4. Lennard-Jones parameters for the bilayer porous graphene membrane[4]

	ε (kcal/mol)	σ (Å)
C	0.086	3.400
H	0.015	2.450

References

(1) Singh, A.; Koros, W. Significance of entropic selectivity for advanced gas separation membranes. *Ind. Eng. Chem. Res.* **1996**, *35*, 1231-1234.

(2) Ning, X.; Koros, W. J. Carbon molecular sieve membranes derived from matrimid® polyimide for nitrogen/methane separation. *Carbon* **2014**, *66*, 511-522.

(3) Sun, Y.; Han, S. Diffusion of N_2, O_2, H_2S and SO_2 in mfi and 4A zeolites by molecular dynamics simulations. *Mol. Simulat.* **2015**, *41*, 1095-1109.

(4) Tian, Z.; Mahurin, S. M.; Dai, S.; Jiang, D.-e. Ion-gated gas separation through porous graphene. *Nano Lett.* **2017**, *17*, 1802-1807

Chapter 7. Highly Selective CO_2 Separation via Graphene/Ionic-Liquid Composites

7.1 Abstract

Pore size is a crucial factor impacting gas separation in porous separation materials, but how to control the pore size to optimize the separation performance remains a challenge. Here we propose a design of graphene/ionic-liquid (GIL) composites with tunable slit pore size where cation and anions are intercalated between graphene layers. By varying the sizes of the ions, we show from first-principles density function theory calculations that the accessible pore size can be tuned from 3.4 Å to 6.0 Å. Grand canonical Monte Carlo simulations of gas uptakes find that the composite materials possess high CO_2 uptakes at room temperature and 1 bar. Further simulations of adsorption of gas mixtures reveals that high CO_2/N_2 and CO_2/CH_4 adsorption selectivities can be obtained when the accessible pore size is < 5 Å. This work suggests a new strategy to achieve tunable pore size via the graphene/IL composites for highly selective CO_2/N_2 and CO_2/CH_4 adsorption.

7.2 Introduction

Increasing demand for energy has been driving the combustion of fossil fuel in the past century. Consequently, rising CO_2 levels in the atmosphere has led to climate change. Developing advanced materials and technologies is key to energy-efficient carbon capture and sequestration (CCS) which has garnered interest of many researchers.[1-3] Sorbents and membranes are two common types of materials for carbon capture.

Porous materials are the most widely studied system for CO_2 separation.[4] Metal-organic frameworks (MOFs) have shown excellent performance as CO_2 sorbents.[5] For example, at 303 K and 0.15 bar, Mg-MOF-74 achieves CO_2 uptake of 5.9 mmol/g and CO_2/N_2 selectivity of 44.[6] Other porous materials such as covalent-organic frameworks, conventional zeolites, porous carbons, and porous organic polymers have also been explored for carbon capture.[7-10]

The pore size of porous materials is an important factor for molecule adsorption and separation.[11] For example, the SIFSIX-3-Zn MOF with a pore size of 3.84 Å shows prominent CO_2 uptakes, while SIFSIX-3-Cu with smaller pore size of 3.5 Å possesses even higher CO_2 uptakes.[12] Based on the idea of the overlapping of potential energy surfaces, the optimal accessible pore size for achieving high uptake and selectivity of CO_2 separation has been shown to be ~3.6 Å.[11] The pore size of SIFSIX-3-Cu is right in this optimal range.

The tremendous advances in 2D materials in the past 15 years prompted the question how one can leverage them to create tunable spaces for carbon capture and storage. One idea is to use pillars and layer-by-layer assembly to create a composite system with tunable interlayer spacing and amply empty space. Due to their non-volatile nature and great tunability,[13] ionic liquids can be the perfect candidate for the pillars. The interface of an ionic liquid with a 2D material has been previously explored for membrane gas separation and water/ion separation.[14] Here we think that there is a great opportunity in creating the composites of 2D materials and ionic liquids as adsorbents for CO_2 separation by controlling the accessible pore size.

Using graphene as our 2D material of choice, Figure 7-1 shows the schematic of our design. The interlayer distance of multilayer graphene as in graphite is just 3.4 Å, so the accessible pore size is zero and there is no space for gas sorption. After inserting an ionic liquid in between graphene layers, the interlayer space could be opened up for gas uptake. By choosing different ionic liquids, the slit pore size could be tuned to achieve highest uptake and/or selectivity. To demonstrate this proof-of-concept, we use both first-principles density function theory calculations (to determine the slit pore size) and grand canonical Monte Carlo simulations (to obtain gas-adsorption isotherms and selectivity).

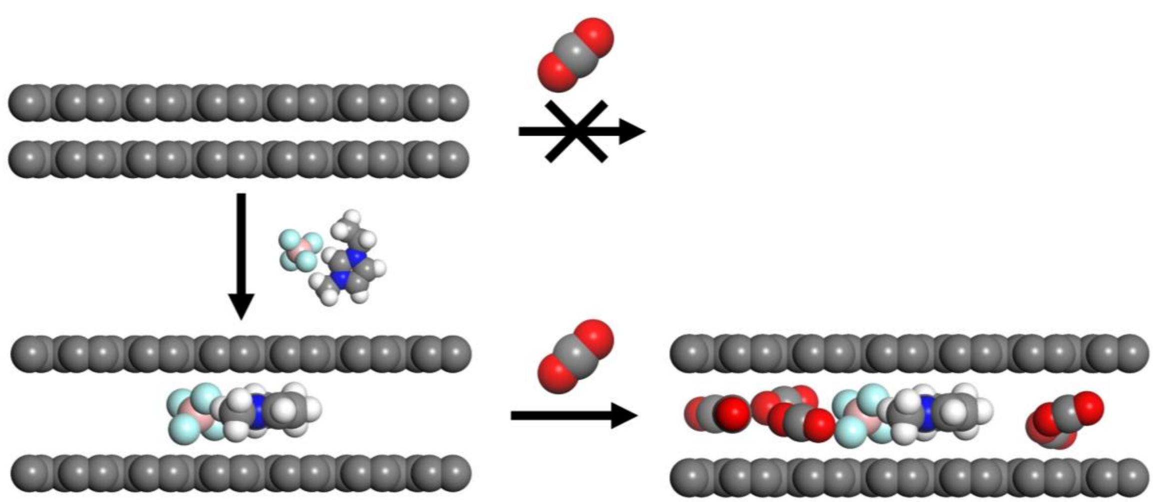

Figure 7-1. Schematic of the design of a composite material of graphene and an ionic liquid for gas adsorption. Ionic liquid is used to as a pillar to open up the space between graphene layers.

7.3 Computational Method

Density function theory (DFT) calculations were performed using the Vienna Ab initio Simulation Package (VASP).[15-17] The generalized gradient approximation (GGA) of Perdew-Burke-Ernzerhof (PBE) was used for electron exchange-correlation.[18] The D3 correction method of Grimme et al. was used for the van der Waals interaction.[19] The projector-augmented wave (PAW) method was used to describe the electron-core interaction.[20] The cutoff energy of 450 eV was applied for the plane-wave basis set. A hexagonal lateral cell of 24.6×24.6 $Å^2$ with a *c* parameter (varying from 7 to 10 Å) was used to simulate the composite material (including a graphene layer and a pair of cation and anion). A 1×1×6 Monkhorst-Pack k-point grid was chosen for sampling the Brillouin zone. The convergence threshold for geometry relaxation was set to 0.025 eV/Å in force.

The grand canonical Monte Carlo (GCMC) method at constant chemical potential μ, volume V, and temperature T was used to simulate the uptakes of pure gases and selectivities of mixed gases at close to the experimental conditions. The periodic boundary conditions in all three dimensions and the generic Dreiding force-field parameters were used.[21] The cutoff of the interatomic interactions was 12.5 Å. The temperature was fixed at 298 K. All GCMC simulations ran 10^7 steps.

7.4 Results and discussion

7.4.1 Composite design and control of the pore size

Figure 7-2 shows the composite material with a layer-by-layer stacked structure of an ionic liquid pillar in between graphene layers. By varying the cation and anions of the room-temperature ionic liquids (Figure 7-3), one can control the size of the slit-like pores.

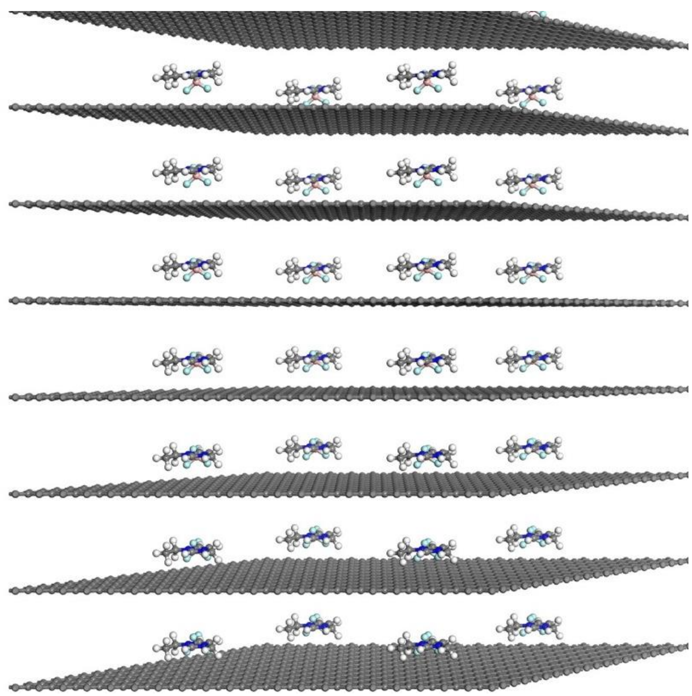

Figure 7-2. Construction of graphene/IL composites via a layer-by-layer structure (coverage: 0.19 ion pair per nm^2).

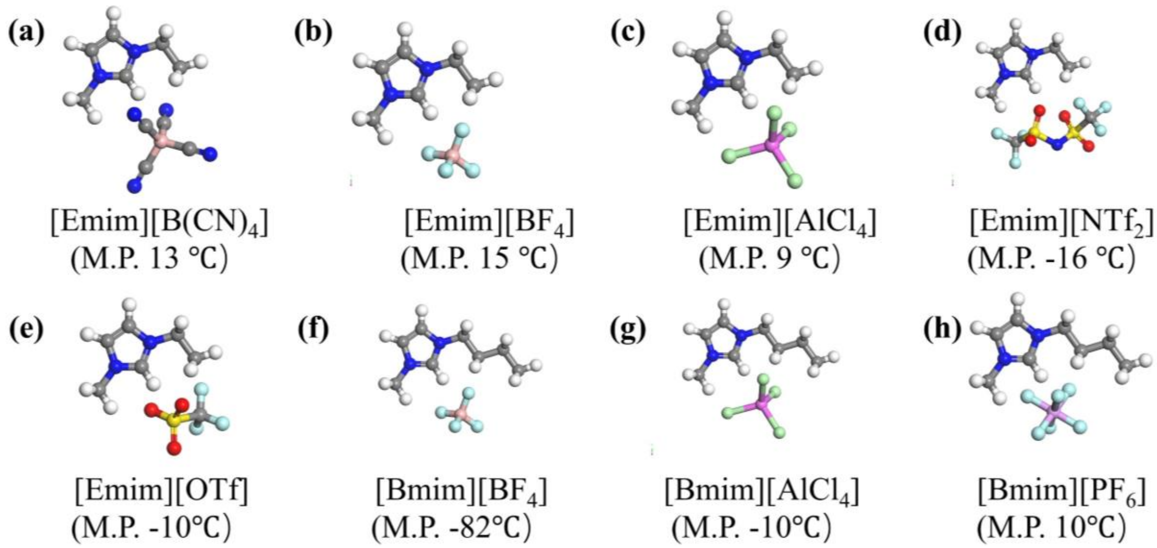

Figure 7-3. Eight room-temperature ionic liquids in our work and their melting points.

To determine the pore size for the different ionic liquid pillars, we optimized the structure of the composite material by DFT-D3 calculations. After optimization, the graphene is still quite flat and only slightly distorted around the ionic liquid. The optimized c parameter represents the interlayer distance between adjacent two layers of graphene. Subtracting the vdW diameter of a carbon atom (3.4 Å; namely, the thickness of the wall), one obtains the accessible pore size. As shown in Table 7-1, the pore sizes are mainly determined by the anion because the two imidazolium cations are similar in size lying flat between graphene layers. As the anion varies from [BF_4] to [$B(CN)_4$], the interlayer distance increases from 6.8 to 9.4 Å while the accessible pore size from 3.4 to 6.0 Å.

Table 7-1. The interlayer distance (D) and accessible pore size (σ) of the graphene/ionic-liquid (IL) composite for different ionic liquids (see Figure 7-3 for their molecular structures).

IL	[Emim][BF_4]	[Bmim][BF_4]	[Bmim][PF_6]	[Emim][OTf]
D (Å)	6.8	6.9	7.2	8.2
σ (Å)	3.4	3.5	3.8	4.8
IL	[Emim][NTf_2]	[Emim][$AlCl_4$]	[Bmim][$AlCl_4$]	[Emim][$B(CN)_4$]
D (Å)	8.9	9.3	9.3	9.4
σ (Å)	5.5	5.9	5.9	6.0

7.4.2 GCMC simulations of pure gas uptakes

We simulated pure-gas uptakes of CO_2, N_2, and CH_4 at 1 bar and 298 K. As shown in Figure 7-4, CO_2 uptakes vary between 8 and 9 mmol/g with the interlayer spacing, which is greatly higher than other state-of-the-art materials. As a comparation, the CO_2 uptake of an excellent porous carbon material is 5.56 mmol/g at the same condition.[22] The slightly increase of CO_2 uptake with the increase of accessible pore size mainly due to the increase of absorption interlayered space. On the other hand, the interaction between N_2 and graphene is weaker than CO_2, so the uptakes are lower than CO_2. Moreover, according to our previous work, the potential energy surface overlap effect plays a dominant role for N_2 uptakes.[11] With the decrease of slit pore size, overlap effect becomes stronger, which causes the increase of N_2 uptakes. Only when the accessible pore size had been reduced to 3.5 Å, the uptake no longer increased. Too small pore size (less than N_2 kinetic diameter of 3.64 Å) will weaken the interaction between N_2 and graphene due to more repulsions. Similarly,

CH_4 uptake curve has the similar trend when accessible pore size decreased from 6 Å. The adsorption energy of CH_4 lies between CO_2 and N_2, so the uptakes are also higher than N_2 but lower than CO_2. However, due to the larger kinetic diameter of CH_4 than N_2, when pore size is equal to or less than 3.5 Å, CH_4 uptakes dramatically decreased and presents an inversed N_2/CH_4 uptake abilities.

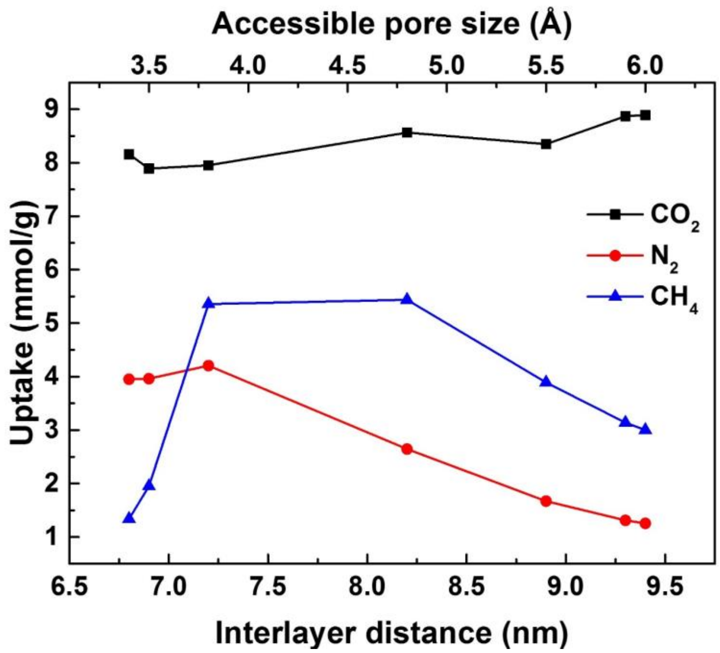

Figure 7-4. Uptakes of pure gas molecules (CO_2 – black, N_2 – red, CH_4 – blue) at 298K and 1 bar by different GIL composites.

7.4.3 GCMC Simulations of Mixed Gas Selectivities

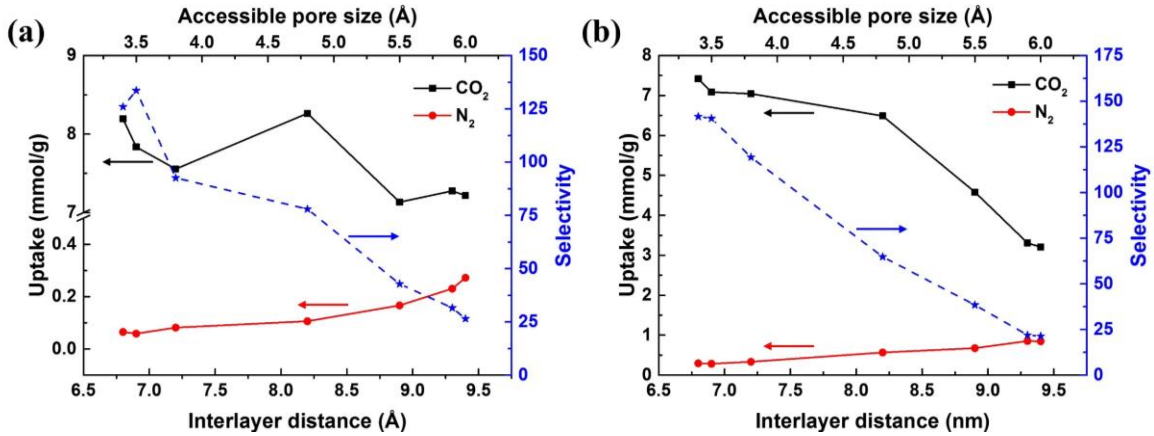

Figure 7-5. Uptakes of CO_2 (black) and N_2 (red) by different GIL composites of (a) 50/50 and (b) 15/85 CO_2/N_2 gas mixtures at 298K and 1 bar and corresponding selectivities (blue).

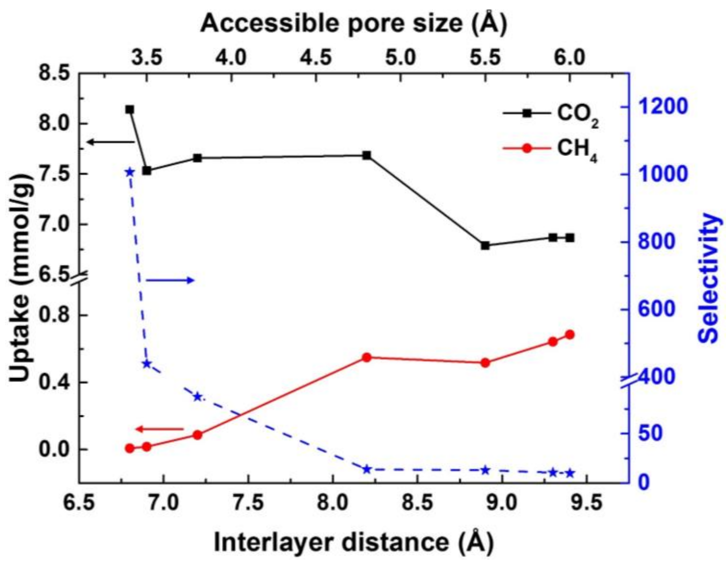

Figure 7-6. Uptakes of CO_2 (black) and CH_4 (red) by different GIL composites of 50/50 CO_2/CH_4 gas mixtures at 298K and 1 bar and corresponding selectivities (blue).

To be relevant to the experimental conditions, we further performed GCMC simulations for gas uptakes and selectivities of a 50%/50% molar ratio mixture of CO_2/N_2

or CO_2/CH_4 and a 15%/85% molar ratio mixture of CO_2/N_2 at 1 bar and 298 K. The selectivity is defined as $S_{i/j} = (x_i/x_j)(y_j/y_i)$, where x_i and y_i are the mole fractions of component i in absorbed and bulk phases, respectively. For the CO_2/N_2 mixture (Figure 7-5), one can see that CO_2 uptakes at partial pressure of 0.5 bar are similar to that in the pure gas at 1 bar. When partial pressure is 0.15 bar, the CO_2 uptakes are still not reduced largely until accessible pore size is larger than 5.0 Å. By contrast, compared with that in the pure gas, N_2 uptakes are significantly decreased, especially when the pore size is small, which leads to an opposite trend between N_2 uptakes and pore size. According to our previous work, when accessible pore size is less than 4.4 Å, the adsorption energy difference between CO_2 and N_2 is the highest and absorbed CO_2 molecules will further block the absorption of N_2.[11] Thus, with the contributions of energy difference and competitive exclusion, the selectivity is increased with the decrease of pore size. For the CO_2/CH_4 mixture (Figure 7-6), competitive exclusion is also proved to play an important role, because of the dramatically reduction of CH_4 uptakes. When the pore size is less than the kinetic diameter of CH_4, the size exclusion effect causes CH_4 uptakes to be closed to zero. So, the CO_2/CH_4 selectivity achieves a pretty high level.

7.4.4 Implications

By GCMC simulations of GIL composite materials, we found that high CO_2 uptakes were achieved at room temperature even compared with other cutting-edge materials. Besides, the composites also possessed satisfactory adsorption selectivities at the actual experimental conditions. A huge selection of ionic liquid suggests diversity of multilayer graphene with different slit pore size for the requirements of absorption of different objective adsorbates.

To experimentally realize the GIL composites, the following steps are briefly suggested below. First, large area graphene layer is grown on a copper substrate,[23] following by a serial of processes to transfer graphene layer to a porous substrate.[24] Next, the nanopores are generated by oxygen plasma etching or ion bombardment of chemical etching.[25-27] Then, low-density ionic liquid pillars are introduced by spin coating.[28] And another layer of graphene is stacked through a polymer transfer layer like PMMA, which can be removed later. By repeating the above steps, the GIL composites can be used for gas absorption.

7.5 Summary and conclusions

In summary, we presented a layer-by-layer graphene/ILs composite material. The interlayer distances were calculated by first-principle DFT-D3 method. We further used GCMC to simulate CO_2/N_2/CH_4 adsorption capacities and selectivities at experimental conditions. The CO_2 uptakes are significantly high than current gas absorbing materials. We also found that high CO_2/N_2 selectivity and CO_2/CH_4 selectivity are achieved for gas mixtures when accessible slit pore size is less than 5 Å and 4 Å separately. This type of composite with high selective absorption ability is an application of many theoretical effects, such as potential energy difference, size exclusion, and competitional exclusion. This work suggests a novel strategy to achieve tunable slit pore size of graphene/ILs composite for high selective carbon capture.

References

(1) D'Alessandro, D. M.; Smit, B.; Long, J. R. Carbon dioxide capture: Prospects for new materials. *Angew. Chem. Int. Ed.* **2010**, *49*, 6058-6082.

(2) Zhang, X.; Zhang, X.; Dong, H.; Zhao, Z.; Zhang, S.; Huang, Y. Carbon capture with ionic liquids: Overview and progress. *Energ. Environ. Sci.* **2012**, *5*, 6668-6681.

(3) Samanta, A.; Zhao, A.; Shimizu, G. K.; Sarkar, P.; Gupta, R. Post-combustion CO_2 capture using solid sorbents: A review. *Ind. Eng. Chem. Res.* **2012**, *51*, 1438-1463.

(4) Bae, Y. S.; Snurr, R. Q. Development and evaluation of porous materials for carbon dioxide separation and capture. *Angew. Chem. Int. Ed.* **2011**, *50*, 11586-11596.

(5) Zhang, Z.; Zhao, Y.; Gong, Q.; Li, Z.; Li, J. MOFs for CO_2 capture and separation from flue gas mixtures: The effect of multifunctional sites on their adsorption capacity and selectivity. *Chem. Commun.* **2013**, *49*, 653-661.

(6) Mason, J. A.; Sumida, K.; Herm, Z. R.; Krishna, R.; Long, J. R. Evaluating metal–organic frameworks for post-combustion carbon dioxide capture via temperature swing adsorption. *Energ. Environ. Sci.* **2011**, *4*, 3030-3040.

(7) Zeng, Y.; Zou, R.; Zhao, Y. Covalent organic frameworks for CO_2 capture. *Adv. Mater.* **2016**, *28*, 2855-2873.

(8) Banerjee, R.; Phan, A.; Wang, B.; Knobler, C.; Furukawa, H.; O'Keeffe, M.; Yaghi, O. M. High-throughput synthesis of zeolitic imidazolate frameworks and application to CO_2 capture. *Science* **2008**, *319*, 939-943.

(9) Singh, G.; Lakhi, K. S.; Sil, S.; Bhosale, S. V.; Kim, I.; Albahily, K.; Vinu, A. Biomass derived porous carbon for CO_2 capture. *Carbon* **2019**.

(10) Wang, W.; Zhou, M.; Yuan, D. Carbon dioxide capture in amorphous porous organic polymers. *J. Mater. Chem. A* **2017**, *5*, 1334-1347.

(11) Wang, S.; Tian, Z.; Dai, S.; Jiang, D.-e. Optimal size of a cylindrical pore for post-combustion CO_2 capture. *J. Phys. Chem. C* **2017**, *121*, 22025-22030.

(12) Shekhah, O.; Belmabkhout, Y.; Chen, Z.; Guillerm, V.; Cairns, A.; Adil, K.; Eddaoudi, M. Made-to-order metal-organic frameworks for trace carbon dioxide removal and air capture. *Nature Comm.* **2014**, *5*, 1-7.

(13) Hansen, J.-P.; McDonald, I. R. *Theory of simple liquids*; Elsevier, 1990.

(14) Tian, Z.; Mahurin, S. M.; Dai, S.; Jiang, D.-e. Ion-gated gas separation through porous graphene. *Nano Lett.* **2017**, *17*, 1802-1807.

(15) Kresse, G.; Furthmüller, J. Efficient iterative schemes for ab initio total-energy calculations using a plane-wave basis set. *Phys. Rev. B* **1996**, *54*, 11169.

(16) Klimeš, J.; Bowler, D. R.; Michaelides, A. Van der waals density functionals applied to solids. *Phys. Rev. B* **2011**, *83*, 195131.

(17) Román-Pérez, G.; Soler, J. M. Efficient implementation of a van der waals density functional: Application to double-wall carbon nanotubes. *Phys. Rev. Lett.* **2009**, *103*, 096102.

(18) Perdew, J. P.; Burke, K.; Ernzerhof, M. Generalized gradient approximation made simple. *Phys. Rev. Lett.* **1996**, *77*, 3865.

(19) Grimme, S.; Antony, J.; Ehrlich, S.; Krieg, H. A consistent and accurate ab initio parametrization of density functional dispersion correction (dft-d) for the 94 elements h-pu. *J. Chem. Phys.* **2010**, *132*, 154104.

(20) Blöchl, P. E. Projector augmented-wave method. *Phys. Rev. B* **1994**, *50*, 17953.

(21) Mayo, S. L.; Olafson, B. D.; Goddard, W. A. Dreiding: A generic force field for molecular simulations. *J. Phys. Chem.* **1990**, *94*, 8897-8909.

(22) Lee, S.-Y.; Park, S.-J. Determination of the optimal pore size for improved CO_2 adsorption in activated carbon fibers. *J. Colloid Interface Sci.* **2013**, *389*, 230-235.

(23) Li, X.; Colombo, L.; Ruoff, R. S. Graphene films: Synthesis of graphene films on copper foils by chemical vapor deposition (adv. Mater. 29/2016). *Adv. Mater.* **2016**, *28*, 6264-6264.

(24) Surwade, S. P.; Smirnov, S. N.; Vlassiouk, I. V.; Unocic, R. R.; Veith, G. M.; Dai, S.; Mahurin, S. M. Water desalination using nanoporous single-layer graphene. *Nat. Nanotechnol.* **2015**, *10*, 459-464.

Chapter 8. Insights into CO_2/N_2 Selectivity in Porous Carbons from Deep Learning

8.1 Abstract

Porous carbons are an important class of porous material for carbon capture. The textural properties of porous carbons greatly influence their CO_2 adsorption capacities. But it is still unclear what features are most conductive to achieve high CO_2/N_2 selectivity. Here, we trained deep neural networks from the experimental data of CO_2 and N_2 uptakes in porous carbons, based on textural features of micropore volume, mesopore volume, and BET surface area. We then used the model to screen porous carbons and to predict CO_2 and N_2 uptakes as well as CO_2/N_2 selectivity. We found that the highest CO_2/N_2 selectivity can be achieved not at the regions of highest CO_2 uptake but at the regions of lowest N_2 uptake where mesopores disrupt N_2 adsorption. This insight will help guide experiment to synthesize better porous carbons for post-combustion CO_2 capture.

8.2 Introduction

Post-combustion CO_2 capture from flue gas (composed mainly of N_2) is an important approach to reduce the CO_2 emissions.[1-3] A range of porous materials for CO_2 capture have been developed, including zeolites,[4] metal-organic frameworks (MOFs),[5-7] covalent-organic frameworks (COFs),[8-10] porous organic polymers,[11] porous carbons,[12-14] ionic liquids,[15-16] advanced solvents,[17-19] and membranes.[20-22]

Porous carbons are versatile due to their tunable pore size, pore shape, and electronic conductivity.[23] An empirical relation for CO_2 adsorption capacity as a function of mesopore (V_{meso}) and micropore (V_{micro}) volumes has been proposed for porous carbons: $M_{ads}^{CO_2} = 0.095 + 2.10 \times V_{micro} + 3.51 \times V_{micro} \times V_{meso}$.[24] Although this relationship can be used to predict CO_2 uptake, it will have difficulty in predicting CO_2/N_2 selectivity, since it does not apply to other gases such as N_2. In addition, it is often very difficult to measure accurately the low N_2 uptakes in materials with high CO_2/N_2 selectivity, so it is desirable to predict N_2 uptakes to guide synthesis.

To establish the complex relationship between the textural properties of porous carbons and the desired CO_2/N_2 selectivity, machine learning is a powerful tool to build a mathematical model based on sample data.[25] As a popular ML method based on artificial neural networks (ANNs), deep learning employs is an ANN with multiple hidden layers, so that it can build a complex non-linear model. The applications of deep learning in chemistry are increasing quickly in recent years.[25-29]

One application of machine learning is to rapidly screen materials,[28] predict properties,[25] and suggest promising candidates for synthesis.[30] Recently, deep learning was for the first time applied to predict CO_2 adsorption in porous carbons.[25] It was found that besides micropore volume, mesopore volume and BET surface area (S_{BET}) are also important in dictating CO_2 uptake.[25] Inspired by this work and moving beyond CO_2 uptake, herein we use deep learning to evaluate another important factor in using porous carbons for post-combustion carbon capture, namely, CO_2/N_2 selectivity.

To achieve our goal, we built two deep NNs (DNNs) for adsorption capacities of CO_2 and N_2, respectively. Each DNN is composed of two hidden layers (Figure 8-1). After training on experimental data, the DNNs were used to make predictions of CO_2 and N_2 uptakes and then the CO_2/N_2 selectivity (as a ratio of the uptakes) for porous carbons of broader feature space. Finally, by analyzing the results, we discuss the desired textual features for the porous carbons to yield high CO_2/N_2 selectivity.

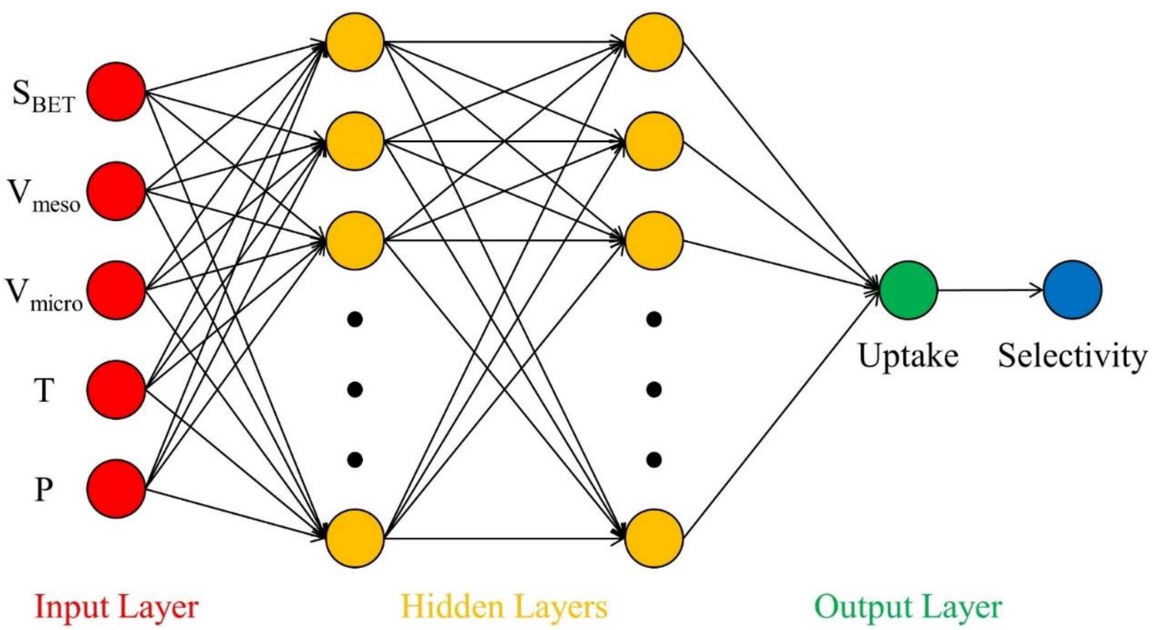

Figure 8-1. The deep neural networks (DNNs) used in the present work to predict gas uptake in porous carbons based on inputs from BET surface area (S_{BET}), mesopore volume (V_{meso}), micropore volume (V_{micro}), temperature (T), and pressure (P).

8.3 Computational Method

All deep neural networks (DNNs) were created by using the MATLAB R2018a environment. The DNNs consist of an input layer, two hidden layers (each having 7 neurons), and an output layer. When training the DNNs, the weights and biases were adjusted according to the gradient descent with momentum and adaptive learning rate backpropagation algorithm. The maximum number of training epochs was 100000 and the performance goal was 0.001.[25] We totally collected 1138 data points of CO_2 uptake[25, 34-38] and 314 data points of N_2 uptake[12, 24, 37-45] in various porous carbons. All screened porous carbons almost have no heteroatom, especially no nitrogen atom, since the amount of N is an important influence factor for the CO_2 adsorption capacity. We used the BET surface area (S_{BET}), micropore volume (V_{micro}), mesopore volume (V_{meso}), temperature (T), and pressure (P) as five input neurons. Gas uptake was used as the output neuron. Both inputs and outputs were normalized in the range of 0 to 1.[46] The leave-one-out method was applied for cross-validation and to avoid overfitting: one data point was used as the validation set and the remaining data points were used as the training set; this process was repeated for each data point.[25]

8.4 Results and discussion

8.4.1 Training neural networks for CO_2 and N_2 uptakes in porous carbons

1138 CO_2 adsorption data points were collected with five varying input parameters

(S_{BET}, V_{meso}, V_{micro}, T, and P). Among them, 1118 random data points were chosen for training a neural network via deep learning (DNN-1). The remaining 20 data points were used to test the trained neural network. As shown in Figure 8-2a, the predicted values and the experimental values are in good agreement, indicating that the trained neural network should be useful for predicting CO_2 uptakes. To check our model accuracy and avoid overfitting, we further did leave-one-out cross-validation.[31] As shown Figure 8-2b, very good linear relationship is found between experimental values and DNN-1 predicted values.

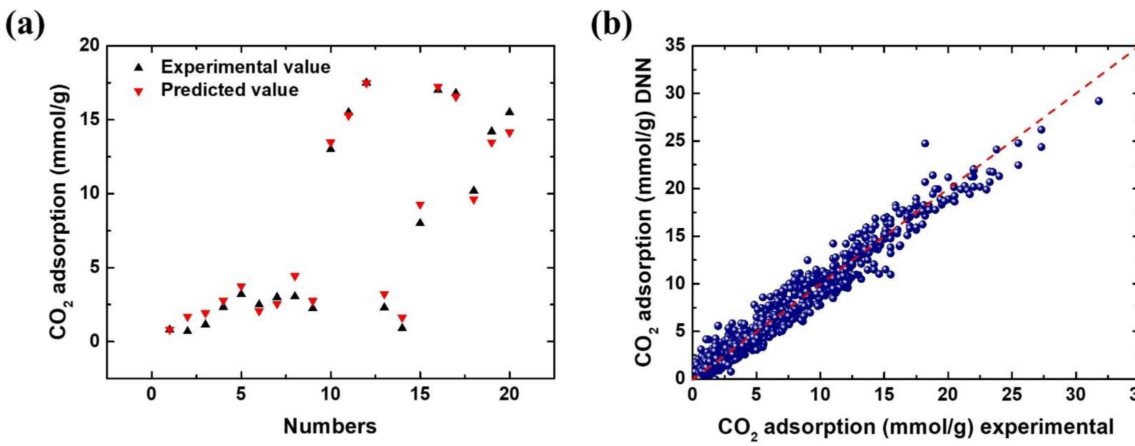

Figure 8-2. Results of predicted CO_2 uptakes. (a) Comparison between experiment and DNN-1 prediction for 20 pairs of CO_2 adsorption values. (b) The correlation between experiment and DNN-1 prediction for CO_2 uptakes by the leave-one-out method ($R^2 = 0.96$).

Likewise, we trained a neural network for N_2 adsorption capacity (DNN-2). 314 N_2 adsorption data points were used: 294 in the training set and 20 in the test set. The training set is smaller than that of CO_2 because most studies reported the N_2 adsorption data only when the porous carbon materials have good selectivity. Nevertheless, a good prediction of the test set is also made by the trained neural network (Figure 8-3a); cross-validation of the training set shows good agreement between experimental values and predicted values (Figure 8-3b).

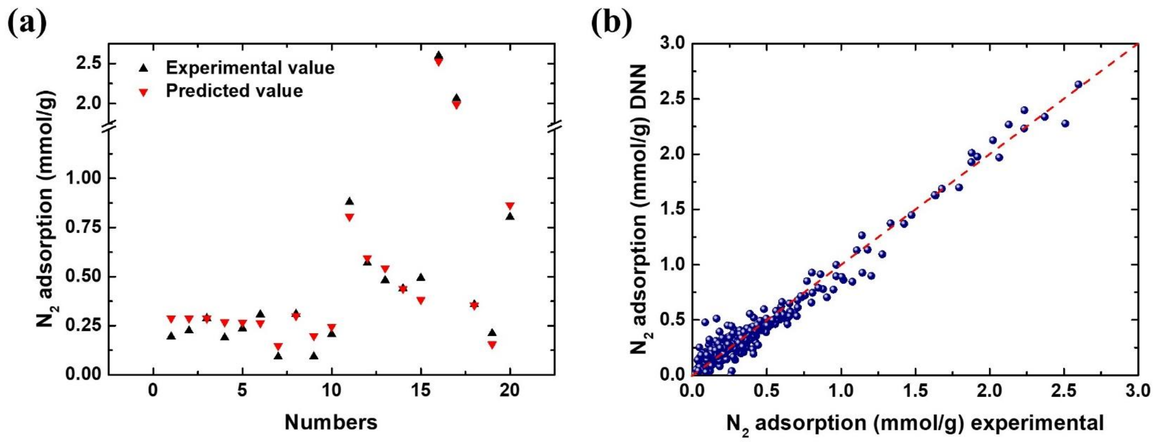

Figure 8-3. Results of predicted N_2 uptakes. (a) Comparison between experiment and DNN-2 prediction for 20 pairs of N_2 adsorption values. (b) The correlation between experiment and DNN-2 prediction for N_2 uptakes by the leave-one-out method ($R^2 = 0.96$).

8.4.2 Exploration of the porous carbon space

With the help of above two well-trained neural networks for CO_2 and N_2 adsorptions (DNN-1 and DNN-2), we can now explore the space of porous carbons. Here, we fixed temperature at 298 K and pressure at 1 bar. By varying S_{BET}, V_{meso}, and V_{micro}, we created 125000 hypothetical data points. From the contour maps, we can pinpoint the regions of highest CO_2 and/or lowest N_2 uptake, to yield highest CO_2/N_2 selectivity. Figure 8-4a shows that the region of $V_{micro} \sim 1.0$ cm^3/g and $S_{BET} \sim 1250$ m^2/g has higher CO_2 uptake. On the other hand, Figure 8-4b shows that porous carbon materials with large S_{BET} and large V_{micro} will have high N_2 uptake, negatively impacting CO_2/N_2 selectivity. Thus, to obtain high selectivity, high CO_2 uptake and low N_2 uptake are necessary.

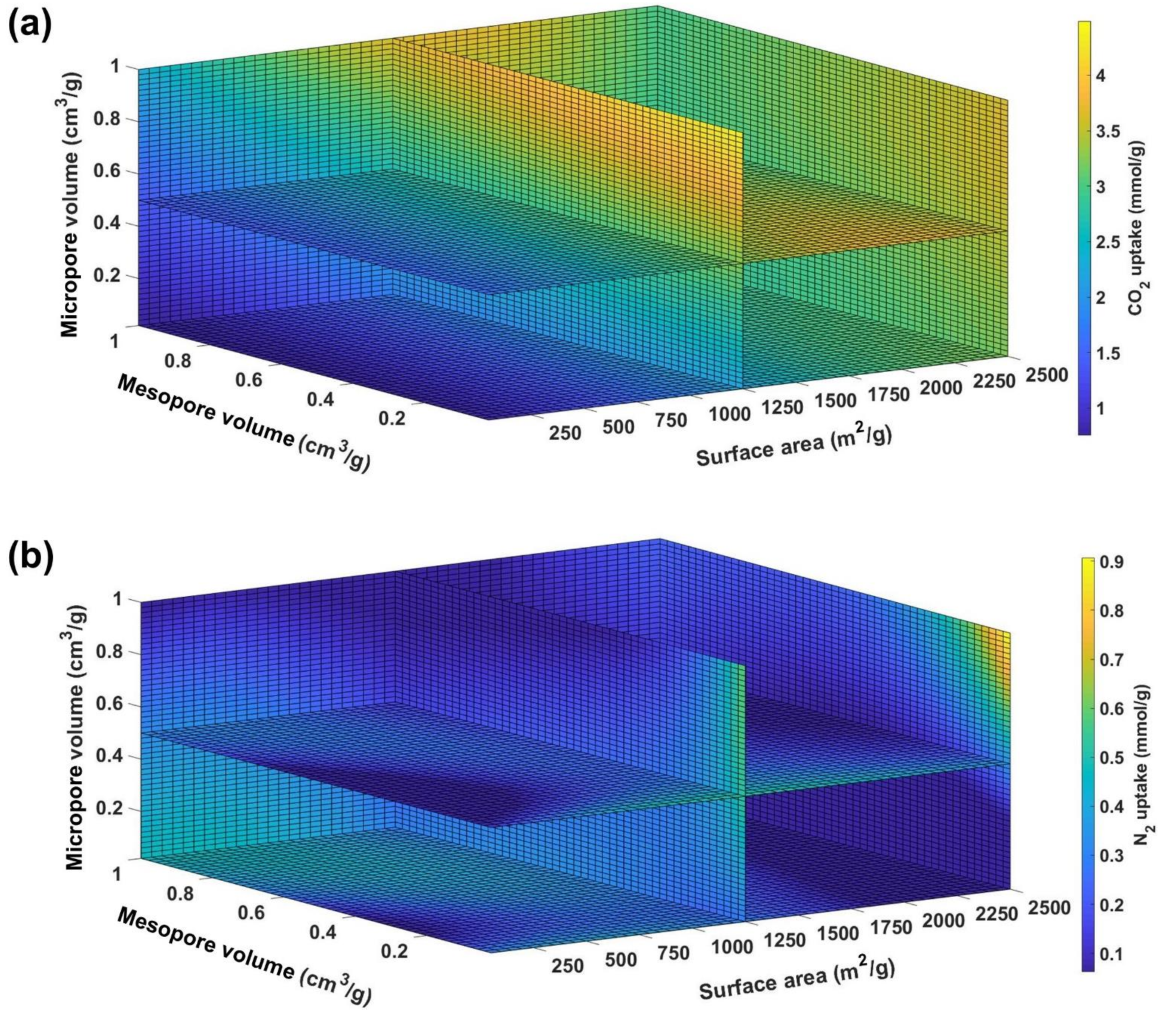

Figure 8-4. The 3D contour maps of (a) CO_2 and (b) N_2 pure-gas adsorption capacities at 298 K and 1 bar in 125000 hypothetical porous carbons predicted from DNN-1 and DNN-2, respectively.

To determine the textural features that can yield high CO_2/N_2 selectivity for realistic porous carbons, we need to reduce the three descriptors to two, since S_{BET} are related to V_{micro} and V_{meso}. By doing this, we can avoid hypothetical carbons that cannot exist (such as a high S_{BET} with close-to-zero V_{micro} and V_{meso}). Toward this end, we trained another neural network (DNN-3) to predict S_{BET} from V_{micro} and V_{meso}. As shown in Figure 8-5, DNN-3 provides a reasonably good model to correlate V_{micro} and V_{meso} to S_{BET}.

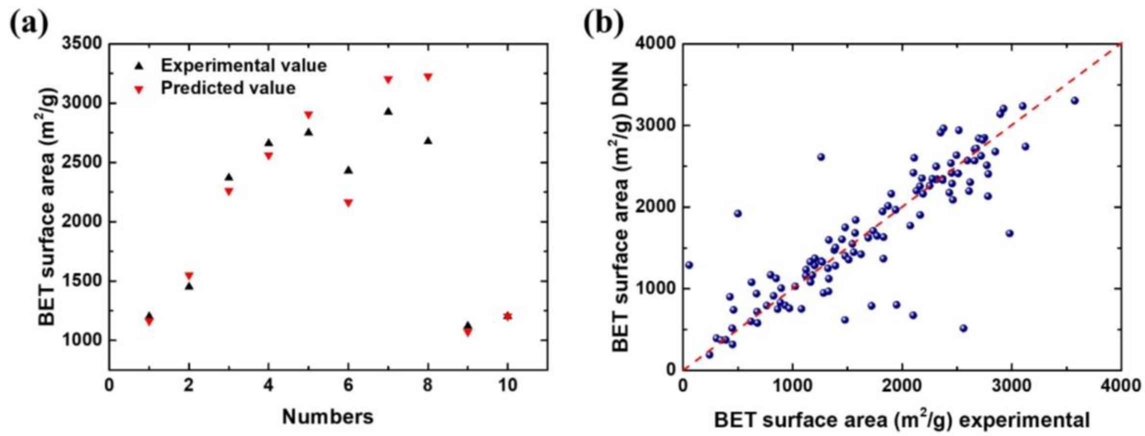

Figure 8-5. Results of predicted BET surface area. (a) Comparison between experiment and DNN-3 prediction for 10 pairs of BET surface area values. (b) The correlation between experiment and DNN-3 prediction for BET surface area by the leave-one-out method ($R^2 = 0.70$).

8.4.3 2D maps of adsorption uptakes and selectivity

With the reduced dimensions, we can now determine the features of porous carbons in terms of V_{micro} and V_{meso} for high CO_2/N_2 selectivity. First, we created 2500 different hypothetical combinations of V_{micro} and V_{meso} ranging from 0.02 to 1.00 cm^3/g. Then, the trained DNN-3 was applied to predict their S_{BET}. As shown in Figure 8-6a, V_{micro} plays a dominating role in S_{BET}: $V_{micro} > 0.5$ cm^3/g generally leads to a larger S_{BET}; for $V_{micro} \sim 0.55$ cm^3/g, V_{meso} can greatly promote S_{BET} by increasing from 0.5 cm^3/g to 1.0 cm^3/g. V_{micro} and V_{meso} as well as S_{BET} from DNN-3 were used as inputs to predict CO_2 and N_2 uptakes at 1 bar and 298 K from DNN-1 and DNN-2, respectively. As shown in Figure 8-6b, there are two regions of high CO_2 uptake (> 4 mmol/g): Region I – high V_{micro} (~ 0.85

cm^3/g) and close-to-zero V_{meso}, where S_{BET} is moderately high (2000 m^2/g); Region II – medium V_{micro} (~ 0.5 cm^3/g) and high V_{meso} (~ 1.0 cm^3/g), where S_{BET} is very high (4000 m^2/g). Interestingly, N_2 uptake is also highest at Region I (Figure 8-6c), leading to moderate CO_2/N_2 selectivity ~ 10 (Figure 8-6d). In contrast, the narrow band from V_{micro} ~ 0.6 cm^3/g and V_{meso} ~ 0.4 cm^3/g to V_{micro} ~ 0.4 cm^3/g and V_{meso} ~ 1.0 cm^3/g has the lowest N_2 uptake (Figure 8-6c) and the highest CO_2/N_2 selectivity ~ 60 (Figure 8-6d). Interestingly, there is another region of low N_2 uptake with V_{micro} ~ 0.7 cm^3/g and V_{meso} ~ 1.0 cm^3/g (Figure 8-6c), leading to moderately high CO_2/N_2 selectivity ~ 30 (Figure 8-6d). Figure 8-6 suggests that inducing more mesopores in microporous carbons disrupts and decreases N_2 adsorption, hence benefiting CO_2/N_2 selectivity. This concept was proposed in 2015 by Choi et al.[32] It's based on their observation that the CO_2/N_2 selectivity actually increases from 273 K to 298 K in ordered mesoporous carbons of 2.9 nm in size, due to a greater decrease in N_2 uptake from 273 K to 298 K. In other words, mesopores are much less attractive to N_2 than to CO_2 at ambient conditions, thereby "disrupting N_2 adsorption".

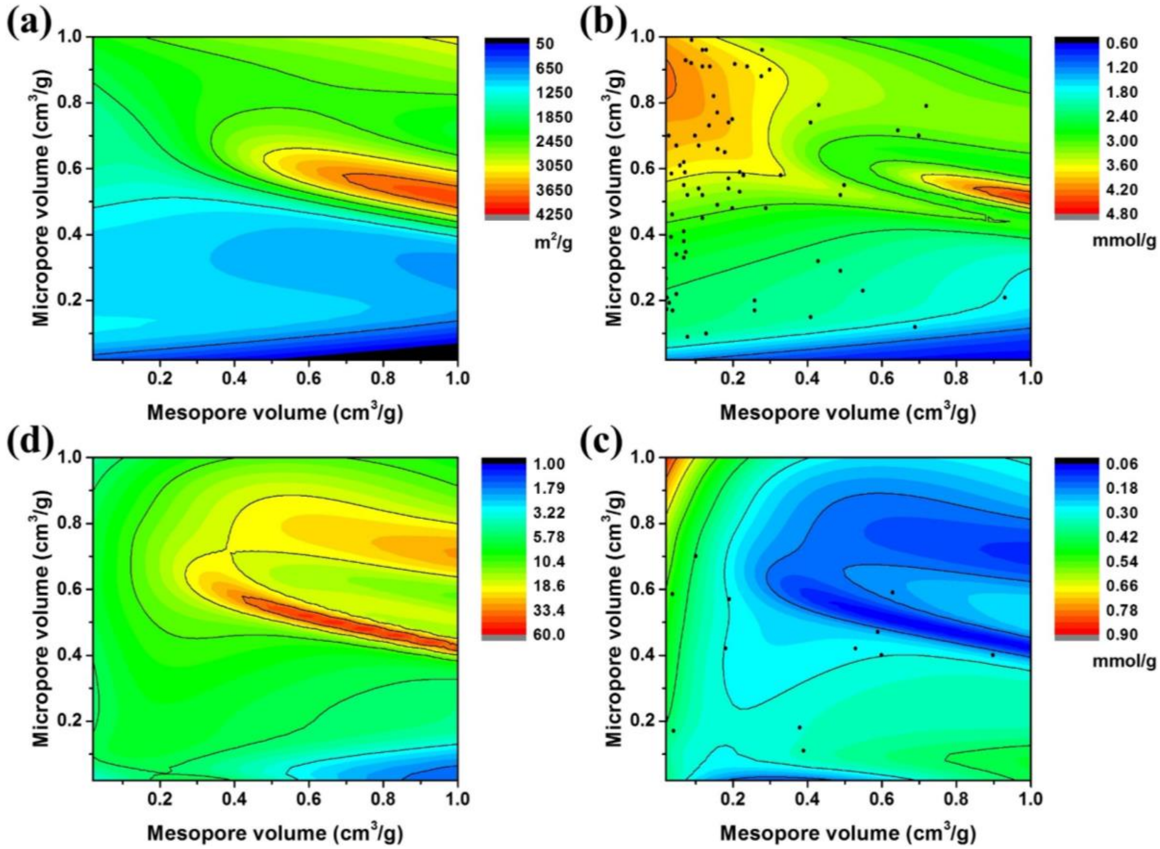

Figure 8-6. The 2D contour maps of (a) BET surface areas (m^2/g), (b) CO_2 and (c) N_2 adsorption capacities (mmol/g), and (d) CO_2/N_2 selectivity for 2500 hypothetical porous carbons at 298 K and 1 bar. The black dots in (b) and (c) represent the experimental data points at the same condition.

To be relevant to the experimental conditions, we further calculated the CO_2/N_2 selectivity for 0.15 bar CO_2 vs 0.85 bar N_2 at 298 K. The CO_2 uptake is shown in Figure 8-7a, while the CO_2/N_2 selectivity is shown in Figure 8-7b. The high selectivity region is similar to that in Figure 8-6d. The available experimental data points in the space of the textual features of porous carbons examined are shown as black dots in Figure 8-6b,c and Figure 8-7a for comparison. One can see that there is very little data at the religions of predicted high CO_2/N_2 selectivity. This could be areas of potential interest for future experimental synthesis.

The selectivity in this work is simply defined as the ratio of pure-component CO_2 and N_2 uptakes at the corresponding gas-phase pressures ($S_{CO_2/N_2} = (n_{CO_2}/p_{CO_2})/(n_{N_2}/p_{N_2})$, where n is the adsorbed amount and p is the gas-phase pressure), which are predicted from neural networks. To predict IAST or Henry's Law selectivity, we need to predict the whole isotherms which is much more time-demanding and difficult to do for N_2 due to the limited data available. We plan to address this issue in the future by directly predicting CO_2 and N_2 adsorption isotherms at ambient conditions and then IAST selectivity from the commonly used experimental measurement of N_2 adsorption isotherm at 77 K.

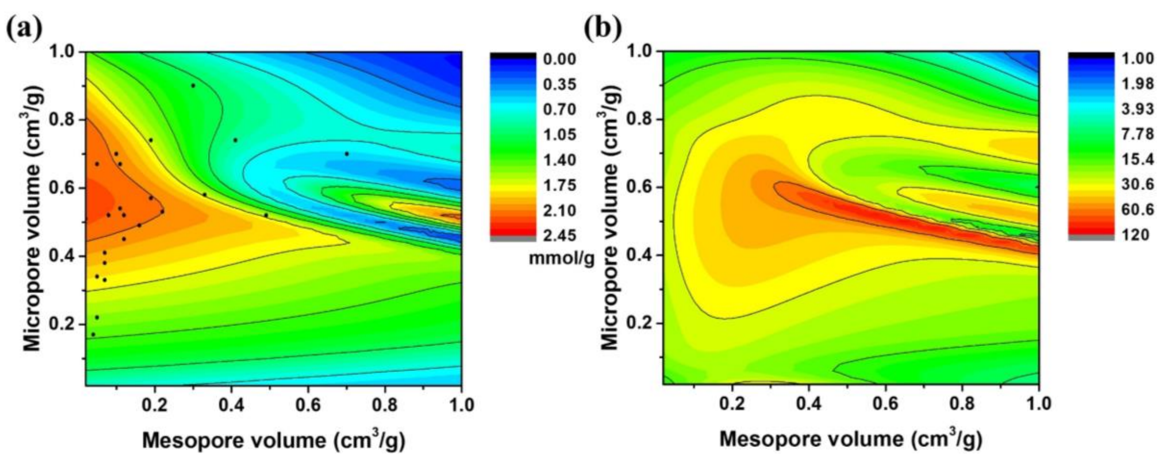

Figure 8-7. The 2D contour maps of (a) CO_2 adsorption capacity at 298K and 0.15 bar, and (b) CO_2/N_2 selectivity for 0.15 bar CO_2 vs 0.85 bar N_2 at 298 K. The black dots in (a) represent the experimental data points.

8.5 Summary and conclusions

In summary, we have trained deep neural networks to predict N_2 uptakes and CO_2/N_2 selectivity for post-combustion CO_2 capture by porous carbons, using three features (micropore volume, mesopore volume, and BET surface area). In this work, all screened porous carbons have approximately nonpolar surface. But it would be interesting to include the polarity of the surface together with the doping of heteroatoms as an additional feature or descriptor in our deep-learning model. This is indeed what we plan to do next. We found that the best features for high CO_2 uptake may not be optimal for CO_2/N_2 selectivity. Instead, focusing on the lowest N_2-uptake regions of moderate micropore and mesopore volumes is a better strategy to achieve highest CO_2/N_2 selectivity. The predicted selectivity maps show promising regions for experimental realization. Pore size is also an important factor for CO_2 adsorption and CO_2/N_2 selectivity.[33] In experiment, the textural features of pore volume, surface area, as well as pore size distribution are all derived from N_2 adsorption isotherms at 77 K. In the future, we hope to directly use N_2 adsorption isotherm at 77 K to predict CO_2 and N_2 adsorption isotherms at ambient conditions.

References

(1) Samanta, A.; Zhao, A.; Shimizu, G. K.; Sarkar, P.; Gupta, R. Post-Combustion CO_2 Capture Using Solid Sorbents: A Review. *Ind. Eng. Chem. Res.* **2011**, *51*, 1438-1463.

(2) Wang, M.; Lawal, A.; Stephenson, P.; Sidders, J.; Ramshaw, C. Post-Combustion CO_2 Capture with Chemical Absorption: A State-of-the-Art Review. *Chem. Eng. Res. Des.* **2011**, *89*, 1609-1624.

(3) Goto, K.; Yogo, K.; Higashii, T. A Review of Efficiency Penalty in a Coal-Fired Power Plant with Post-Combustion CO_2 Capture. *Appl. Energy* **2013**, *111*, 710-720.

(4) Choi, S.; Drese, J. H.; Jones, C. W. Adsorbent Materials for Carbon Dioxide Capture from Large Anthropogenic Point Sources. *ChemSusChem* **2009**, *2*, 796-854.

(5) Sumida, K.; Rogow, D. L.; Mason, J. A.; McDonald, T. M.; Bloch, E. D.; Herm, Z. R.; Bae, T.-H.; Long, J. R. Carbon Dioxide Capture in Metal-Organic Frameworks. *Chem. Rev.* **2011**, *112*, 724-781.

(6) McDonald, T. M.; Lee, W. R.; Mason, J. A.; Wiers, B. M.; Hong, C. S.; Long, J. R. Capture of Carbon Dioxide from Air and Flue Gas in the Alkylamine-Appended Metal-Organic Framework mmen-Mg_2(dobpdc). *J. Am. Chem. Soc.* **2012**, *134*, 7056-7065.

(7) Huang, R.; Hill, M. R.; Babarao, R.; Medhekar, N. V. CO_2 Adsorption in Azobenzene Functionalized Stimuli Responsive Metal-Organic Frameworks. *J. Phys. Chem. C* **2016**, *120*, 16658-16667.

(8) Zeng, Y.; Zou, R.; Zhao, Y. Covalent Organic Frameworks for CO_2 Capture. *Adv. Mater.* **2016**, *28*, 2855-2873.

(9) Huang, N.; Krishna, R.; Jiang, D. Tailor-Made Pore Surface Engineering in Covalent Organic Frameworks: Systematic Functionalization for Performance Screening. *J. Am. Chem. Soc.* **2015**, *137*, 7079-7082.

(10) Ullah, R.; Atilhan, M.; Anaya, B.; Al-Muhtaseb, S.; Aparicio, S.; Patel, H.; Thirion, D.; Yavuz, C. T. Investigation of Ester-and Amide-Linker-Based Porous Organic Polymers for Carbon Dioxide Capture and Separation at Wide Temperatures and Pressures. *ACS Appl. Mater. Inter.* **2016**, *8*, 20772-20785.

(11) Xie, L. H.; Suh, M. P. High CO_2-Capture Ability of a Porous Organic Polymer Bifunctionalized with Carboxy and Triazole Groups. *Chem. Eur. J.* **2013**, *19*, 11590-11597.

(12) Hao, G. P.; Li, W. C.; Qian, D.; Lu, A. H. Rapid Synthesis of Nitrogen-Doped Porous Carbon Monolith for CO_2 Capture. *Adv. Mater.* **2010**, *22*, 853-857.

(13) Sevilla, M.; Parra, J. B.; Fuertes, A. B. Assessment of the Role of Micropore Size and N-Doping in CO_2 Capture by Porous Carbons. *ACS Appl. Mater. Inter.* **2013**, *5*, 6360-6368.

(14) Chen, J.; Yang, J.; Hu, G.; Hu, X.; Li, Z.; Shen, S.; Radosz, M.; Fan, M. Enhanced CO_2 Capture Capacity of Nitrogen-Doped Biomass-Derived Porous Carbons. *ACS Sustain. Chem. Eng.* **2016**, *4*, 1439-1445.

(15) Mahurin, S. M.; Lee, J. S.; Baker, G. A.; Luo, H.; Dai, S. Performance of Nitrile-Containing Anions in Task-Specific Ionic Liquids for Improved CO_2/N_2 Separation. *J. Membr. Sci.* **2010**, *353*, 177-183.

(16) Tian, Z.; Mahurin, S. M.; Dai, S.; Jiang, D.-e. Ion-Gated Gas Separation through Porous Graphene. *Nano Lett.* **2017**, *17*, 1802-1807.

(17) Zhang, K.; Li, X. S.; Chen, H.; Singh, P.; King, D. L. Molten Salt Promoting Effect in Double Salt CO_2 Absorbents. *J. Phys. Chem. C* **2015**, *120*, 1089-1096.

(18) Giri, N.; Del Pópolo, M. G.; Melaugh, G.; Greenaway, R. L.; Rätzke, K.; Koschine, T.; Pison, L.; Gomes, M. F. C.; Cooper, A. I.; James, S. L. Liquids with Permanent Porosity. *Nature* **2015**, *527*, 216-220.

(19) Zhang, J. S.; Chai, S. H.; Qiao, Z. A.; Mahurin, S. M.; Chen, J. H.; Fang, Y. X.; Wan, S.; Nelson, K.; Zhang, P. F.; Dai, S. Porous Liquids: A Promising Class of Media for Gas Separation. *Angew. Chem. Int. Ed.* **2015**, *54*, 932-936.

(20) Koros, W. J.; Zhang, C. Materials for Next-Generation Molecularly Selective Synthetic Membranes. *Nat. Mater.* **2017**, *16*, 289-297.

(21) Jiang, D. E.; Cooper, V. R.; Dai, S. Porous Graphene as the Ultimate Membrane for Gas Separation. *Nano Lett.* **2009**, *9*, 4019-4024.

(22) Pera-Titus, M. Porous Inorganic Membranes for CO_2 Capture: Present and Prospects. *Chem. Rev.* **2014**, *114*, 1413-1492.

(23) Lee, J.; Kim, J.; Hyeon, T. Recent Progress in the Synthesis of Porous Carbon Materials. *Adv. Mater.* **2006**, *18*, 2073-2094.

(24) Dura, G.; Budarin, V. L.; Castro-Osma, J. A.; Shuttleworth, P. S.; Quek, S. C. Z.; Clark, J. H.; North, M. Importance of Micropore-Mesopore Interfaces in Carbon Dioxide Capture by Carbon-Based Materials. *Angew. Chem. Int. Ed.* **2016**, *55*, 9173-9177.

(25) Zhang, Z. H.; Schott, J. A.; Liu, M. M.; Chen, H.; Lu, X. Y.; Sumpter, B. G.; Fu, J.; Dai, S. Prediction of Carbon Dioxide Adsorption Via Deep Learning. *Angew. Chem. Int. Ed.* **2019**, *58*, 259-263.

(26) Ryan, K.; Lengyel, J.; Shatruk, M. Crystal Structure Prediction Via Deep Learning. *J. Am. Chem. Soc.* **2018**, *140*, 10158-10168.

(27) Wei, J. N.; Duvenaud, D.; Aspuru-Guzik, A. Neural Networks for the Prediction of Organic Chemistry Reactions. *ACS Cent. Sci.* **2016**, *2*, 725-732.

(28) Xie, T.; Grossman, J. C. Crystal Graph Convolutional Neural Networks for an Accurate and Interpretable Prediction of Material Properties. *Phys. Rev. Lett.* **2018**, *120*, 145301.

(29) Cao, B.; Adutwum, L. A.; Oliynyk, A. O.; Luber, E. J.; Olsen, B. C.; Mar, A.; Buriak, J. M. How to Optimize Materials and Devices Via Design of Experiments and Machine Learning: Demonstration Using Organic Photovoltaics. *ACS nano* **2018**, *12*, 7434-7444.

(30) Shafiei, A.; Ahmadi, M. A.; Zaheri, S. H.; Baghban, A.; Amirfakhrian, A.; Soleimani, R. Estimating Hydrogen Sulfide Solubility in Ionic Liquids Using a Machine Learning Approach. *J. Supercrit. Fluids* **2014**, *95*, 525-534.

(31) Toyao, T.; Suzuki, K.; Kikuchi, S.; Takakusagi, S.; Shimizu, K.; Takigawa, I. Toward Effective Utilization of Methane: Machine Learning Prediction of Adsorption Energies on Metal Alloys. *J. Phys. Chem. C* **2018**, *122*, 8315-8326.

(32) Lee, J. H.; Lee, H. J.; Lim, S. Y.; Kim, B. G.; Choi, J. W. Combined CO_2-Philicity and Ordered Mesoporosity for Highly Selective CO_2 Capture at High Temperatures. *J. Am. Chem. Soc.* **2015**, *137*, 7210-7216.

(33) Wang, S.; Tian, Z.; Dai, S.; Jiang, D.-e. Optimal Size of a Cylindrical Pore for Post-Combustion CO_2 Capture. *J. Phys. Chem. C* **2017**, *121*, 22025-22030.

(34) Aleghafouri, A.; Mohsen-Nia, M.; Mohajeri, A.; Mahdyarfar, M.; Asghari, M. Micropore Size Analysis of Activated Carbons Using Nitrogen, Carbon Dioxide and Methane Adsorption Isotherms: Experimental and Theoretical Studies. *Adsorpt. Sci. Technol.* **2012**, *30*, 307-316.

(35) Zhuo, H.; Hu, Y. J.; Tong, X.; Zhong, L. X.; Peng, X. W.; Sun, R. C. Sustainable Hierarchical Porous Carbon Aerogel from Cellulose for High-Performance Supercapacitor and CO_2 Capture. *Ind. Crop. Prod.* **2016**, *87*, 229-235.

(36) Xu, C.; Ruan, C. Q.; Li, Y. X.; Lindh, J.; Stromme, M. High-Performance Activated Carbons Synthesized from Nanocellulose for CO_2 Capture and Extremely Selective Removal of Volatile Organic Compounds. *Adv. Sustain. Syst.* **2018**, *2*, 1700147.

(37) Chang, B.; Sun, L.; Shi, W.; Zhang, S.; Yang, B. Cost-Efficient Strategy for Sustainable Cross-Linked Microporous Carbon Bead with Satisfactory CO_2 Capture Capacity. *ACS Omega* **2018**, *3*, 5563-5573.

(38) Heo, Y.-J.; Park, S.-J. A Role of Steam Activation on CO_2 Capture and Separation of Narrow Microporous Carbons Produced from Cellulose Fibers. *Energy* **2015**, *91*, 142-150.

(39) Hong, S.-M.; Choi, S. W.; Kim, S. H.; Lee, K. B. Porous Carbon Based on Polyvinylidene Fluoride: Enhancement of CO_2 Adsorption by Physical Activation. *Carbon* **2016**, *99*, 354-360.

(40) Hao, G.-P.; Li, W.-C.; Qian, D.; Wang, G.-H.; Zhang, W.-P.; Zhang, T.; Wang, A.-Q.; Schüth, F.; Bongard, H.-J.; Lu, A.-H. Structurally Designed Synthesis of Mechanically Stable Poly(benzoxazine-co-resol)-Based Porous Carbon Monoliths and Their Application as High-Performance CO_2 Capture Sorbents. *J. Am. Chem. Soc.* **2011**, *133*, 11378-11388.

(41) Balahmar, N.; Al-Jumialy, A. S.; Mokaya, R. Biomass to Porous Carbon in One Step: Directly Activated Biomass for High Performance CO_2 Storage. *J. Mater. Chem. A* **2017**, *5*, 12330-12339.

(42) Mahurin, S. M.; Górka, J.; Nelson, K. M.; Mayes, R. T.; Dai, S. Enhanced CO_2/N_2 Selectivity in Amidoxime-Modified Porous Carbon. *Carbon* **2014**, *67*, 457-464.

(43) Yuan, B.; Wu, X.; Chen, Y.; Huang, J.; Luo, H.; Deng, S. Adsorption of CO_2, CH_4, and N_2 on Ordered Mesoporous Carbon: Approach for Greenhouse Gases Capture and Biogas Upgrading. *Environ. Sci. Technol.* **2013**, *47*, 5474-5480.

(44) Sun, N.; Sun, C.; Liu, J.; Liu, H.; Snape, C. E.; Li, K.; Wei, W.; Sun, Y. Surface-Modified Spherical Activated Carbon Materials for Pre-Combustion Carbon Dioxide Capture. *RSC Adv.* **2015**, *5*, 33681-33690.

(45) Ghosh, S.; Sarathi, R.; Ramaprabhu, S. Magnesium Oxide Modified Nitrogen-Doped Porous Carbon Composite as an Efficient Candidate for High Pressure Carbon Dioxide Capture and Methane Storage. *J. Colloid Interface Sci.* **2019**, *539*, 245-256.

(46) Shakeri, S.; Ghassemi, A.; Hassani, M.; Hajian, A. Investigation of Material Removal Rate and Surface Roughness in Wire Electrical Discharge Machining Process for Cementation Alloy Steel Using Artificial Neural Network. *Int. J. Adv. Manuf. Tech.* **2016**, *82*, 549-557

Chapter 9. Prediction of CO_2/N_2 Selectivity in Porous Carbons from N_2 Adsorption Isotherm at 77 K via Convolutional Neural Networks

9.1 Abstract

Porous carbons are an important class of porous materials with many applications including gas separation, while N_2 adsorption isotherm at 77 K is the most widely used approach to characterize porosity. Conventionally, textual properties such as surface area and pore volumes are derived from the N_2 adsorption isotherm at 77 K via fitting to an adsorption theory and then correlated to gas separation performance (uptake and selectivity). Here we use the N_2 isotherm at 77 K directly as input (representing feature descriptors for the porosity) to train convolutional neural networks that predict gas separation performance (using CO_2/N_2 as a test case) for porous carbons more accurately. We then explore the porosity space for porous carbons for higher CO_2/N_2 selectivity. We find that porous carbons with a bimodal pore-size distribution of well-separated mesopores (3 – 7 nm) and micropores (< 2 nm) are most promising. This work will be useful in guiding experimental research of porous carbons with desired porosity for gas separation and other applications.

9.2 Introduction

Due to their low cost, large surface area, fast adsorption-desorption kinetics, and tunable porosity,[1,2] porous carbons are widely used as separation media for gases, ions, and large molecules[3-7] as well as electrodes for supercapacitors[8-10] and other electrochemical applications.[11,12] However, their amorphous nature impedes our understanding of their structure-property relationship at the atomic level. As a comprise, researchers have used textural properties such as surface area and pore volumes as structural descriptors to establish correlation with properties such as uptakes of CO_2 and N_2 for post-combustion carbon capture.[13-15] To this end, an empirical function for predicting CO_2 uptake ($M_{ads}^{CO_2}$) was proposed based on fitting the experimental data of CO_2 uptakes to the textural properties of porous carbons: $M_{ads}^{CO_2} = 0.095 + 2.10 \times V_{micro} + 3.51 \times V_{micro} \times V_{meso}$, where V_{micro} is micropore volume and V_{meso} is mesopore volume.[13] Going beyond the empirical relationship, Zhang et al. employed a deep learning neural network approach based on the same experimental database and trained a model that uses the BET surface area S_{BET} in addition to V_{micro} and V_{meso} as input parameters to predict CO_2 uptake.[14] More recently, a similar deep learning method was used to predict N_2 uptakes at ambient conditions as well as CO_2/N_2 selectivity.[15]

Despite the insights from these data-driven, machine-learning (ML) approaches using textural features of porous carbons as input, important information such as pore size distribution (PSD) has not been explicitly used in the ML models. PSD and textural features are most commonly obtained from N_2 adsorption isotherm at 77 K fitted to a theoretical model such as BET[16] or non-local density functional theory (NL-DFT).[17] In other words, N_2 adsorption isotherm at 77 K contains rich information about the porosity of a porous carbon that could be harvested for a ML model directly, to establish a mapping between porosity and gas-separation performance for porous carbons, bypassing the BET or NL-DFT theory. To this end, this paper aims to demonstrate such a ML model by using the convolutional neural networks (CNNs)[18] that directly take as input the experimental 77K-N_2-adsorption isotherms of porous carbons.

9.3 Results and discussion

9.3.1 Prediction of CO_2 and N_2 uptakes

CNNs are an important deep learning algorithm most commonly applied to analyze images, because they are good at extracting features and handling high-dimensional inputs.[19] There are already a few applications of CNNs in chemistry, such as crystal symmetry determination and molecular fingerprinting.[20-22] Figure 9-1a shows a typical architecture of our CNNs. Each 77K-N_2-adsorption curve as a 1D image is represented by an array of 200 pressure points and their corresponding adsorbed volumes, which is fed into five convolutional layers that automatically extract features from the image. Then, these features as representations of porosity, together with temperature (T: 273 ~ 323 K) and pressure (P: 0 ~ 1 bar) inputs, are fed into three fully connected layers and one regression layer to an output neuron that is the gas uptake (see Supporting Information and

Figure S9-1 for details). 111 different experimental 77K-N_2-adsorption curves corresponding to 111 different porous carbons were used as input. Their gas-adsorption performances at ambient conditions were collected (679 uptake data points for CO_2 and 291 for N_2) and each partitioned into 3 sets: 70% of data as training set, 15% as validation set, and 15% as test set. As shown in Figure 9-1b and c, after training both models of CNN-1 (for prediction of CO_2 adsorption capacity) and CNN-2 (for N_2) show excellent agreement with the experimental values for not only training and validation sets but also test sets. This indicates that CNN-1 and CNN-2 can reliably predict CO_2 and N_2 uptakes at ambient conditions directly using 77K-N_2-adsorption isotherm as input.

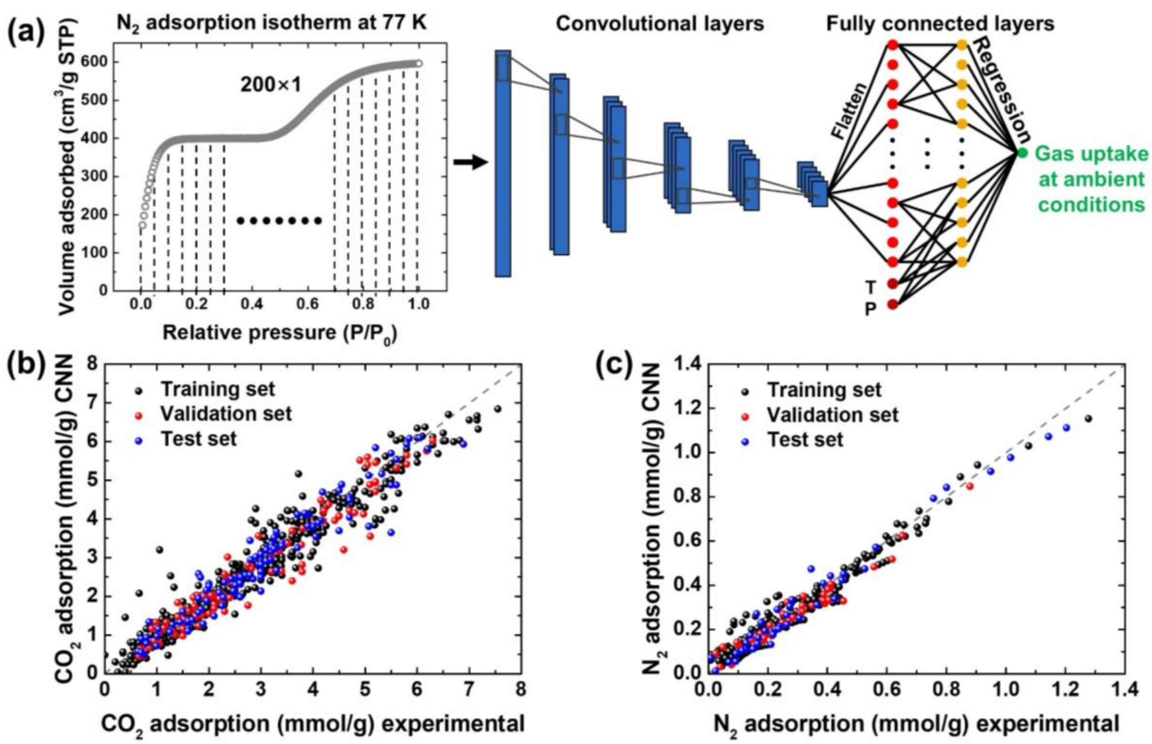

Figure 9-1. Results of predicted gas uptakes. (a) Architecture of the convolutional neural networks (CNN) used in this work: input, N_2 adsorption at 77 K; output, gas uptakes at ambient temperature

(T) and pressure (P). The correlation between experimental and CNN-predicted gas uptakes: (b) CO_2 by CNN-1; (c) N_2 by CNN-2.

Armed with the two CNNs, we can now explore the much wider space of porous carbons with different porosity as characterized by their 77K-N_2-adsorption isotherms, to find the promising ones with high CO_2 uptakes and/or high CO_2/N_2 selectivity around 298 K and 1 bar, conditions relevant to post-combustion CO_2 capture. We generated 1 million 77K-N_2-adsorption isotherms corresponding to 1 million hypothetical porous carbons by using an analytical function with six varying parameters (see SI and Figure S9-2 for details). We divided the isotherms into four groups (see Figure S9-3 for 10 examples for each group). Groups 1 and 4 are mainly type I isotherms representing microporous carbons, while groups 2 and 3 are mainly type IV isotherms representing mesoporous carbons.

The 1 million 77K-N_2-adsorption isotherms in four groups are fed into CNN-1 and CNN-2 to predict their CO_2 and N_2 uptakes (at 298 K and 1 bar), respectively. Figure 9-2 shows the results for each group. One can see that some porous carbons belong to groups 2 and 3 can achieve CO_2 uptake above 5 mmol/g at 298 K and 1 bar. More interestingly, some porous carbons of groups 2 and 3 have very low N_2 uptakes. In other words, some mesopore structures in groups 2 and 3 offer great opportunity in controlling CO_2/N_2 selectivity than the micropore-dominated groups 1 and 2.

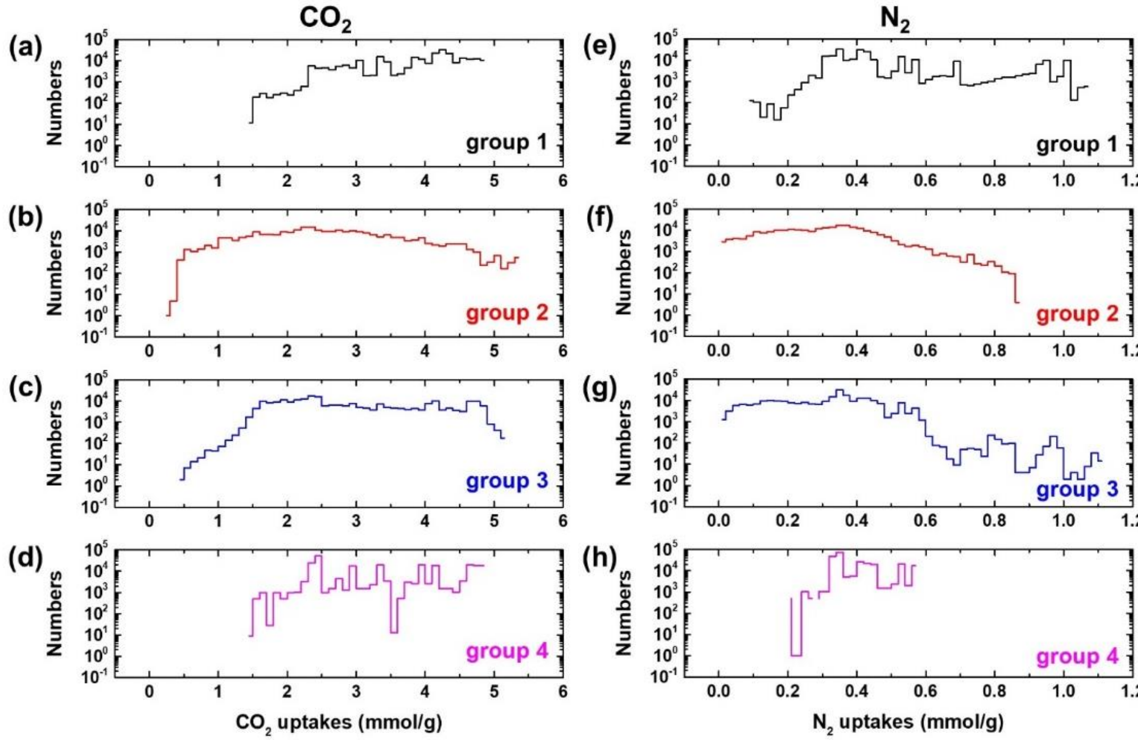

Figure 9-2. Statistical distribution of gas uptakes at 298 K and 1 bar in each of the four groups of hypothetical porous carbons: (a-d) CO_2; (e-h) N_2.

9.3.2 Prediction of CO_2/N_2 IAST selectivity

To quantify the CO_2/N_2 selectivity relevant to post-combustion carbon capture and to compare with experimental values, we applied the Ideal Adsorbed Solution Theory (IAST),[23] a thermodynamic theory which predicts mixed-gas selectivity from a set of pure gas adsorption isotherms at ambient conditions. Here, we first used CNN-1 and CNN-2 to predict CO_2 and N_2 uptakes at 298 K for 20 different pressures (from 0.05 bar to 1 bar) for each hypothetical porous carbon, to obtain pure-gas adsorption isotherms at 298 K. Then we applied the IAST theory to our CNN-predicted pure-gas isotherms and obtained the predicted CO_2/N_2 selectivity for a mixed gas of 90 mol% N_2 and 10 mol% CO_2 at 298 K and 1 bar (total pressure). See SI for details of our prediction of IAST selectivity. The results are analyzed as follows.

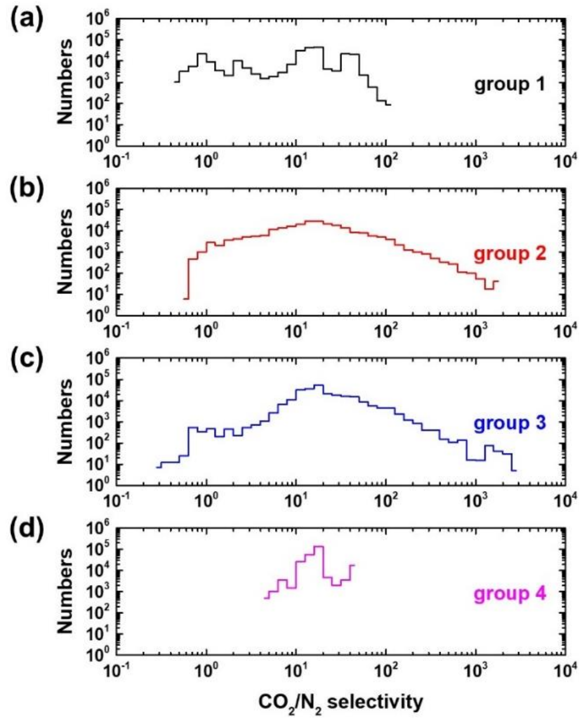

Figure 9-3. Statistical distribution of CO_2/N_2 IAST selectivity for 90 mol% N_2 and 10 mol% CO_2 at 298 K and total pressure of 1 bar for the four groups of hypothetical porous carbons.

The distributions of IAST selectivity for four groups of hypothetical porous carbons are shown in Figure 9-3. The highest selectivity is about 100 for group 1 and 40 for group 4, similar to the experimental selectivity of common microporous carbons.[24-26] In contrast, the highest selectivity is about 2000 for group 2 and 3000 for group 3, two groups where mesopores are predominant.

9.3.3 Optimal pore size distribution

To further understand the origin of the highest selectivity, the best-performing ones in each group are singled out and their 77K-N_2-adsorption isotherms and corresponding pore-size distributions are shown in Figure 9-4 (see SI for details of how the pore-size distributions are obtained). One can see that porous carbons with gapped (or well-separated) bimodal distributions of distinct micropores and mesopores have the highest selectivity: the case from group 2 has a peak around 1.5 nm and another around 4.0 nm, while the case from group 3 has peaks around 0.5 nm and 6.5 nm. The two cases from groups 1 and 4 resemble conventional activated carbons with a continuous (or not well-separated) distribution of micropores (predominant) to mesopores up to 5 nm, which have a much lower selectivity than the two cases from groups 2 and 3. Hence, our finding points out a design strategy for porous carbons in terms of post-combustion carbon capture: creating a porous carbon with nonoverlapping, distinct micropores (< 2 nm) and mesopores (3 – 7 nm). This conclusion echoes a few recent studies[13-15,27] in emphasizing the importance of mesopores in porous carbons for CO_2 uptake and gas separation. More important, we provide a target porosity to guide synthesis. In the future, we hope to further incorporate defects and functional groups in our training models to predict their effects in addition to porosity.

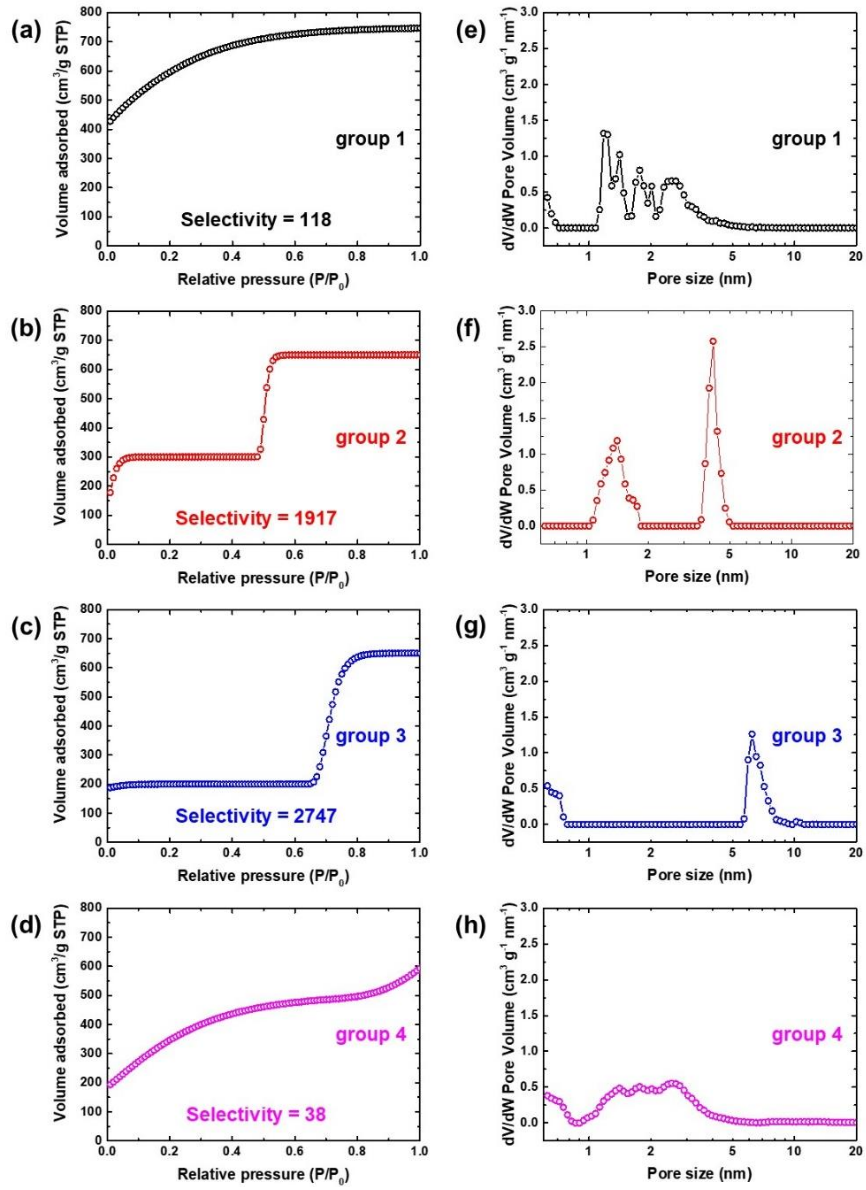

Figure 9-4. (a-d) N_2 adsorption isotherm at 77 K and (e-h) the corresponding pore size distribution of the hypothetical porous carbon with the highest IAST CO_2/N_2 selectivity in each group for 90 mol% N_2 and 10 mol% CO_2 at 298 K and total pressure of 1 bar.

9.4 Summary and conclusions

In sum, to understand and predict how the porosity of porous carbons impacts their

CO_2/N_2 separation performance, we have used their N_2 adsorption isotherms at 77 K as direct input to train convolutional neural networks (CNN) to predict their CO_2 and N_2 uptakes and CO_2/N_2 selectivity at ambient conditions. Excellent agreement between experimental and CNN-predicted values was achieved. We then explored one million hypothetical porous carbons of varying 77K-N_2-adsorption isotherms and predicted their CO_2/N_2 separation performance. From the predicted IAST selectivity of a CO_2-N_2 mixture, we found that the highest selectivity on the order of 2000 – 3000 can be achieved for porous carbons that have bimodal distributions of well-separated micropores (< 2 nm) and mesopores (3 – 7 nm).

References

(1) Lee, J.; Kim, J.; Hyeon, T. Recent progress in the synthesis of porous carbon materials. *Adv. Mater*. **2006**, *18*, 2073-2094.

(2) Liang, C.; Li, Z.; Dai, S. Mesoporous carbon materials: Synthesis and modification. *Angew. Chem. Int. Ed.* **2008**, *47*, 3696-3717.

(3) Richter, H.; Voss, H.; Kaltenborn, N.; Kämnitz, S.; Wollbrink, A.; Feldhoff, A.; Caro, J.; Roitsch, S.; Voigt, I. High-flux carbon molecular sieve membranes for gas separation. *Angew. Chem. Int. Ed.* **2017**, *56*, 7760-7763.

(4) Chen, W.; Chen, S.; Liang, T.; Zhang, Q.; Fan, Z.; Yin, H.; Huang, K.-W.; Zhang, X.; Lai, Z.; Sheng, P. High-flux water desalination with interfacial salt sieving effect in nanoporous carbon composite membranes. *Nat. Nanotechnol.* **2018**, *13*, 345-350.

(5) Merchant, C. A.; Healy, K.; Wanunu, M.; Ray, V.; Peterman, N.; Bartel, J.; Fischbein, M. D.; Venta, K.; Luo, Z.; Johnson, A. C. DNA translocation through graphene nanopores. *Nano Lett.* **2010**, *10*, 2915-2921.

(6) Guo, L. P.; Hu, Q. T.; Zhang, P.; Li, W. C.; Lu, A. H. Polyacrylonitrile-derived sponge-like micro/macroporous carbon for selective CO_2 separation. *Chem. Eur. J.* **2018**, *24*, 8369-8374.

(7) Hao, G. P.; Li, W. C.; Qian, D.; Lu, A. H. Rapid synthesis of nitrogen-doped porous carbon monolith for CO_2 capture. *Adv. Mater.* **2010**, *22*, 853-857.

(8) Zhai, Y.; Dou, Y.; Zhao, D.; Fulvio, P. F.; Mayes, R. T.; Dai, S. Carbon materials for chemical capacitive energy storage. *Adv. Mater.* **2011**, *23*, 4828-4850.

(9) Lobato, B.; Suárez, L.; Guardia, L.; Centeno, T. A. Capacitance and surface of carbons in supercapacitors. *Carbon* **2017**, *122*, 434-445.

(10) Wang, D. W.; Li, F.; Liu, M.; Lu, G. Q.; Cheng, H. M. 3d aperiodic hierarchical porous graphitic carbon material for high-rate electrochemical capacitive energy storage. *Angew. Chem. Int. Ed.* **2008**, *47*, 373-376.

(11) Hou, Y.; Wen, Z.; Cui, S.; Ci, S.; Mao, S.; Chen, J. An advanced nitrogen-doped graphene/cobalt-embedded porous carbon polyhedron hybrid for efficient catalysis of oxygen reduction and water splitting. *Adv. Funct. Mater.* **2015**, *25*, 872-882.

(12) Chen, Y.; Ji, S.; Wang, Y.; Dong, J.; Chen, W.; Li, Z.; Shen, R.; Zheng, L.; Zhuang, Z.; Wang, D. Isolated single iron atoms anchored on n-doped porous carbon as an efficient electrocatalyst for the oxygen reduction reaction. *Angew. Chem. Int. Ed.* **2017**, *56*, 6937-6941.

(13) Durá, G.; Budarin, V. L.; Castro-Osma, J. A.; Shuttleworth, P. S.; Quek, S. C.; Clark, J. H.; North, M. Importance of micropore–mesopore interfaces in carbon dioxide capture by carbon-based materials. *Angew. Chem. Int. Ed.* **2016**, *55*, 9173-9177.

(14) Zhang, Z.; Schott, J. A.; Liu, M.; Chen, H.; Lu, X.; Sumpter, B. G.; Fu, J.; Dai, S. Prediction of carbon dioxide adsorption via deep learning. *Angew. Chem. Int. Ed.* **2019**, *58*, 259-263.

(15) Wang, S.; Zhang, Z.; Dai, S.; Jiang, D.-e. Insights into CO_2/N_2 selectivity in porous carbons from deep learning. *ACS Mater. Lett.* **2019**, *1*, 558-563.

(16) Brunauer, S.; Emmett, P. H.; Teller, E. Adsorption of gases in multimolecular layers. *J. Am. Chem. Soc.* **1938**, *60*, 309-319.

(17) Ravikovitch, P. I.; Haller, G. L.; Neimark, A. V. Density functional theory model for calculating pore size distributions: Pore structure of nanoporous catalysts. *Adv. Colloid Interface Sci.* **1998**, *76*, 203-226.

(18) Lawrence, S.; Giles, C. L.; Tsoi, A. C.; Back, A. D. Face recognition: A convolutional neural-network approach. *IEEE T. Neural Networ.* **1997**, *8*, 98-113.

(19) Masci, J.; Meier, U.; Cireşan, D.; Schmidhuber, J. In *International conference on artificial neural networks*; Springer: 2011, p 52-59.

(20) Kaufmann, K.; Zhu, C.; Rosengarten, A. S.; Maryanovsky, D.; Harrington, T. J.; Marin, E.; Vecchio, K. S. Crystal symmetry determination in electron diffraction using machine learning. *Science* **2020**, *367*, 564-568.

(21) Lee, J.-W.; Park, W. B.; Lee, J. H.; Singh, S. P.; Sohn, K.-S. A deep-learning technique for phase identification in multiphase inorganic compounds using synthetic xrd powder patterns. *Nat. Commum.* **2020**, *11*, 1-11.

(22) Ziletti, A.; Kumar, D.; Scheffler, M.; Ghiringhelli, L. M. Insightful classification of crystal structures using deep learning. *Nat. Commum.* **2018**, *9*, 1-10.

(23) Myers, A. L.; Prausnitz, J. M. Thermodynamics of mixed-gas adsorption. *AlChE J.* **1965**, *11*, 121-127.

(24) Hong, S.-M.; Choi, S. W.; Kim, S. H.; Lee, K. B. Porous carbon based on polyvinylidene fluoride: Enhancement of CO_2 adsorption by physical activation. *Carbon* **2016**, *99*, 354-360.

(25) Balahmar, N.; Al-Jumialy, A. S.; Mokaya, R. Biomass to porous carbon in one step: Directly activated biomass for high performance CO_2 storage. *J. Mater. Chem. A* **2017**, *5*, 12330-12339.

(26) Chang, B.; Sun, L.; Shi, W.; Zhang, S.; Yang, B. Cost-efficient strategy for sustainable cross-linked microporous carbon bead with satisfactory CO_2 capture capacity. *ACS Omega* **2018**, *3*, 5563-5573.

(27) Lee, J. H.; Lee, H. J.; Lim, S. Y.; Kim, B. G.; Choi, J. W. Combined CO_2-philicity and ordered mesoporosity for highly selective CO_2 capture at high temperatures. *J. Am. Chem. Soc.* **2015**, *137*, 7210-7216.

Supporting Information

1. Details of the neural networks and training methods used: The convolutional neural networks CNN-1 and CNN-2 were created in the MATLAB R2019b environment using the stochastic gradient descent with momentum (SGDM) optimizer. The CNNs included one input layer, five convolutional layers, three fully connected dense layers, and one output layer (Figure S9-1).

From each N_2 adsorption isotherm, 200 adsorbed volume values at different relative pressures were extracted as an input layer of size 200×1. After each convolutional layer, a batch normalization (BN) layer was used to speed up training and one rectified linear unit (ReLU) layer and one average pooling layer (Avpool) was employed to perform down-sampling. Flatten layer (Flat) transformed multi-channel output of convolutional layers into a single long feature vector that can be fed into a fully connected layer. Concatenation layer (Concat) was used to concatenate features from convolutional layers and other input features (temperature and pressure) together. Dense layers were the fully connected layers, which multiplied the input by a weight matrix and then adds a bias vector. After each dense layer, a BN layer, a leaky ReLU layer (Leaky), and a dropout layer with dropout probability 0.125 (Dropout) were applied to avoid overfitting. The filter sizes of five convolutional layers were [9,1], [7,1], [7,1], [5,1], [3,1], the number of filters were 2, 3, 4, 5, 5, and the neuron numbers of three dense layers were 1024, 256, and 1. During the training process, the parameters in convolutional filters as well as weights and biases were adjusted to improve the performance. The maximum number of training epochs was 3000. The initial learning rate was 0.01 and reduced by a factor 0.99 every 10 epochs. The training data was shuffled before each training epoch. The 111 different experimental 77K-N_2-adsorption curves and their gas-adsorption performances at ambient conditions (679 uptake data points for CO_2[1-19] and 291 for N_2[3,10,12,13,16,19-22]) were collected from the literature.

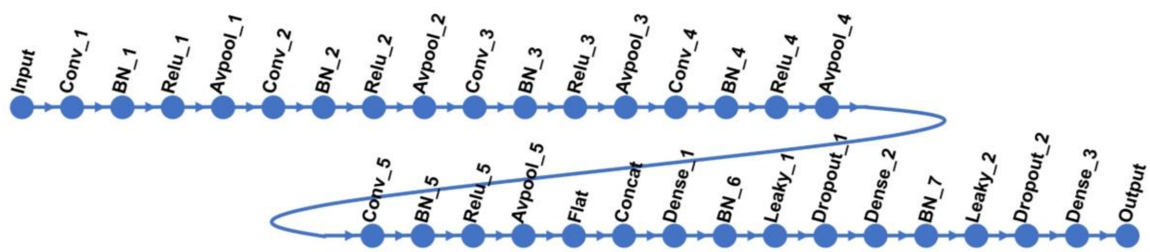

Figure S9-1. The detailed architecture of the convolutional neural networks used in this work. The layer names represent different types of layer. "Input": image input layer; "Conv": convolutional layer; "BN": batch normalization layer; "Relu": rectified linear unit activation layer; "Avpool": average pooling layer; "Flat": flatten layer; "Concat": concatenation layer; "Dense": fully connected layer; "Leaky": leaky ReLU activation layer; "Dropout": dropout layer; "Output": regression output layer.

2. Generating 1 million 77K-N_2-adsorption isotherms: 1 million 77K-N_2-adsorption isotherms corresponding to 1 million hypothetical porous carbons were generated by a function: $y = a_1 e^{-e^{-b_1(x-c_1)}} + a_2 e^{-e^{-b_2(x-c_2)}}$, where y is N_2 adsorption value at 77 K, x is the adsorption pressure, parameter a_1 and a_2 control the equilibrium values of isotherm curve, parameter b_1 and b_2 control the slope of steps, and parameter c_1 and c_2 control the position of steps (Figure S9-2). The range of each parameter: $a_1 = 50 \sim 500$, $a_2 = 50 \sim 500$, $b_1 = 5 \sim 95, b_2 = 5 \sim 95, c_1 = -0.4 \sim 0, c_2 = -0.4 \sim 1.5$. The increments of these variables are 50 for a_1 and a_2, 10 for b_1 and b_2, 0.1 for c_1 and c_2. We further divide the 1million isotherms into four groups (see Figure S9-3 for some examples in each group).

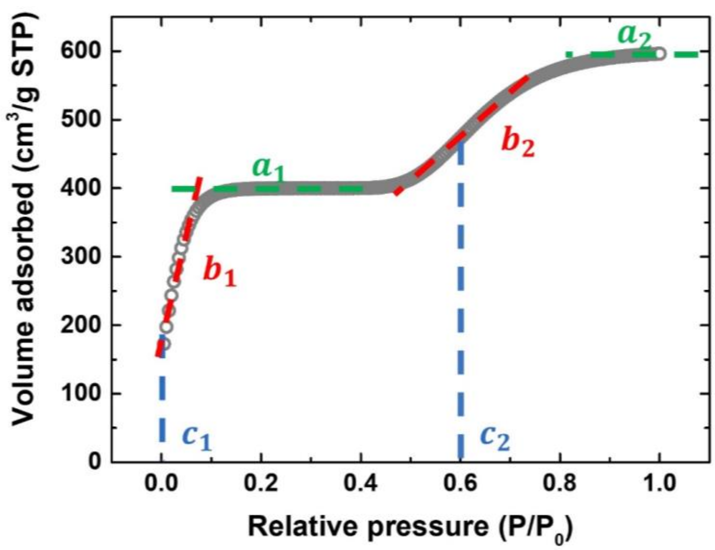

Figure S9-2. An N_2 adsorption isotherm at 77 K created by generation function ($y = 400e^{-e^{-35(x-0)}} + 200e^{-e^{-10(x-0.6)}}$).

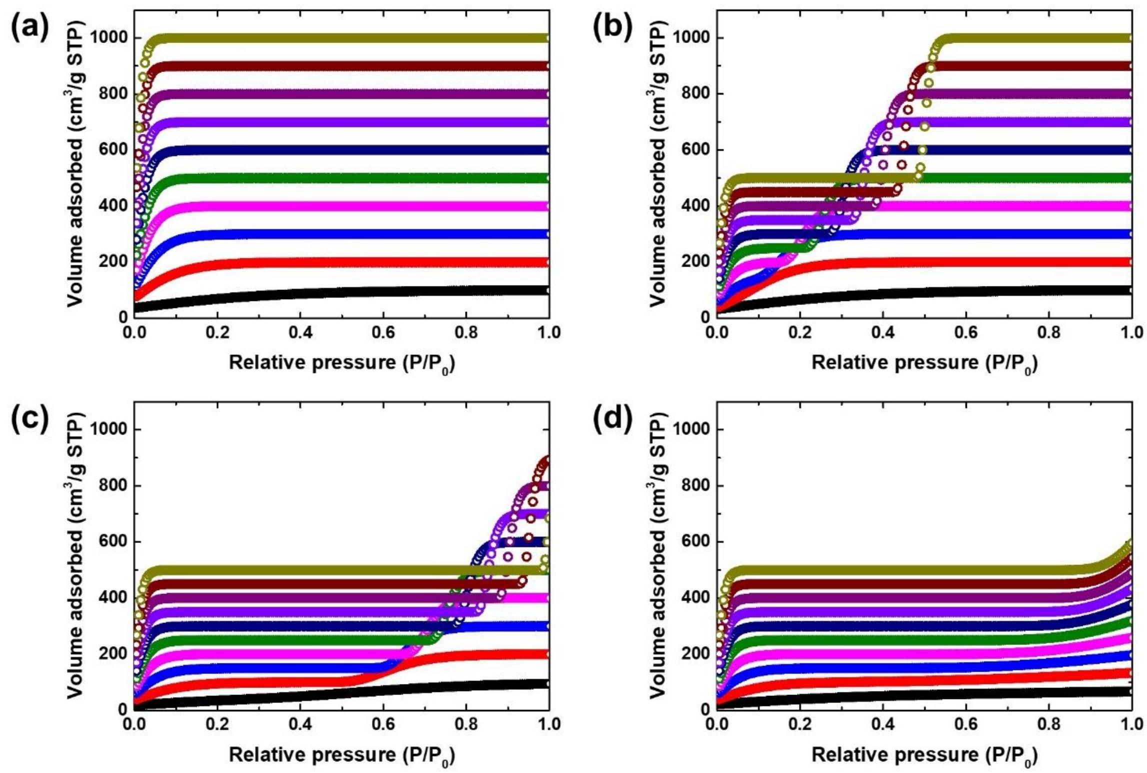

Figure S9-3. The N_2 adsorption isotherm examples from (a) group 1 ($c_2 = -0.4 \sim 0.0$), (b) group 2 ($c_2 = 0.1 \sim 0.5$), (c) group 3 ($c_2 = 0.6 \sim 1.0$), and (d) group 4 ($c_2 = 1.1 \sim 1.5$).

3. Prediction of Ideal Adsorbed Solution Theory (IAST) selectivity: The IAST selectivity was calculated by using the pyIAST code.[23] Each pure-gas adsorption isotherm at 298 K was fit to the Langmuir model. These fitting parameters were provided as input to calculate the adsorption values of CO_2 and N_2 for a mixed gas of 90 mol% N_2 and 10 mol% CO_2 at 298 K and 1 bar (total pressure). Finally, the IAST selectivity was calculated by the following function: $S = (q_1/q_2)/(p_1/p_2)$, where q_1 and q_2 are the uptakes of CO_2 and N_2, and p_1 and p_2 are the partial pressures of CO_2 and N_2.

4. Plotting pore size distribution: The pore size distribution was plotted by using an experimental software QuadraWin. It was obtained from N_2 adsorption isotherm at 77 K using non-local density functional theory (NLDFT) method.

References

(1) Hirst, E. A.; Taylor, A.; Mokaya, R. A simple flash carbonization route for conversion of biomass to porous carbons with high CO_2 storage capacity. *J. Mater. Chem. A* **2018**, *6*, 12393-12403.

(2) Parshetti, G. K.; Chowdhury, S.; Balasubramanian, R. Biomass derived low-cost microporous adsorbents for efficient CO_2 capture. *Fuel* **2015**, *148*, 246-254.

(3) Balahmar, N.; Al-Jumialy, A. S.; Mokaya, R. Biomass to porous carbon in one step: Directly activated biomass for high performance CO_2 storage. *J. Mater. Chem. A* **2017**, *5*, 12330-12339.

(4) Sevilla, M.; Fuertes, A. B. CO_2 adsorption by activated templated carbons. *J. Colloid Interface Sci.* **2012**, *366*, 147-154.

(5) Lee, S.-Y.; Park, S.-J. Determination of the optimal pore size for improved CO_2 adsorption in activated carbon fibers. *J. Colloid Interface Sci.* **2013**, *389*, 230-235.

(6) Casco, M. E.; Martínez-Escandell, M.; Silvestre-Albero, J.; Rodríguez-Reinoso, F. Effect of the porous structure in carbon materials for CO_2 capture at atmospheric and high-pressure. *Carbon* **2014**, *67*, 230-235.

(7) Estevez, L.; Barpaga, D.; Zheng, J.; Sabale, S.; Patel, R. L.; Zhang, J.-G.; McGrail, B. P.; Motkuri, R. K. Hierarchically porous carbon materials for CO_2 capture: The role of pore structure. *Ind. Eng. Chem. Res.* **2018**, *57*, 1262-1268.

(8) Wahby, A.; Ramos-Fernández, J. M.; Martínez-Escandell, M.; Sepúlveda-Escribano, A.; Silvestre-Albero, J.; Rodríguez-Reinoso, F. High-surface-area carbon molecular sieves for selective CO_2 adsorption. *ChemSusChem* **2010**, *3*, 974-981.

(9) Sevilla, M.; Al-Jumialy, A. S. M.; Fuertes, A. B.; Mokaya, R. Optimization of the pore structure of biomass-based carbons in relation to their use for CO_2 capture under low- and high-pressure regimes. *ACS Appl. Mater. Inter.* **2018**, *10*, 1623-1633.

(10) Hong, S.-M.; Choi, S. W.; Kim, S. H.; Lee, K. B. Porous carbon based on polyvinylidene fluoride: Enhancement of CO_2 adsorption by physical activation. *Carbon* **2016**, *99*, 354-360.

(11) Ludwinowicz, J.; Jaroniec, M. Potassium salt-assisted synthesis of highly microporous carbon spheres for CO_2 adsorption. *Carbon* **2015**, *82*, 297-303.

(12) Hao, G. P.; Li, W. C.; Qian, D.; Lu, A. H. Rapid synthesis of nitrogen-doped porous carbon monolith for CO_2 capture. *Adv. Mater.* **2010**, *22*, 853-857.

(13) Hao, G.-P.; Li, W.-C.; Qian, D.; Wang, G.-H.; Zhang, W.-P.; Zhang, T.; Wang, A.-Q.; Schüth, F.; Bongard, H.-J.; Lu, A.-H. Structurally designed synthesis of mechanically stable poly (benzoxazine-co-resol)-based porous carbon monoliths and their application as high-performance CO_2 capture sorbents. *J. Am. Chem. Soc.* **2011**, *133*, 11378-11388.

(14) Travis, W.; Gadipelli, S.; Guo, Z. Superior CO_2 adsorption from waste coffee ground derived carbons. *RSC Adv.* **2015**, *5*, 29558-29562.

(15) Sevilla, M.; Fuertes, A. B. Sustainable porous carbons with a superior performance for CO_2 capture. *Energ. Environ. Sci.* **2011**, *4*, 1765-1771.

(16) Heo, Y.-J.; Park, S.-J. A role of steam activation on CO_2 capture and separation of narrow microporous carbons produced from cellulose fibers. *Energy* **2015**, *91*, 142-150.

(17) Xu, C.; Ruan, C. Q.; Li, Y.; Lindh, J.; Strømme, M. High-performance activated carbons synthesized from nanocellulose for CO_2 capture and extremely selective removal of volatile organic compounds. *Adv. Sustain. Syst.* **2018**, *2*, 1700147.

(18) Zhuo, H.; Hu, Y.; Tong, X.; Zhong, L.; Peng, X.; Sun, R. Sustainable hierarchical porous carbon aerogel from cellulose for high-performance supercapacitor and CO_2 capture. *Ind. Crop. Prod.* **2016**, *87*, 229-235.

(19) Chang, B.; Sun, L.; Shi, W.; Zhang, S.; Yang, B. Cost-efficient strategy for sustainable cross-linked microporous carbon bead with satisfactory CO_2 capture capacity. *ACS Omega* **2018**, *3*, 5563-5573.

(20) Yuan, B.; Wu, X.; Chen, Y.; Huang, J.; Luo, H.; Deng, S. Adsorption of CO_2, CH_4, and N_2 on ordered mesoporous carbon: Approach for greenhouse gases capture and biogas upgrading. *Environ. Sci. Technol.* **2013**, *47*, 5474-5480.

(21) Mahurin, S. M.; Górka, J.; Nelson, K. M.; Mayes, R. T.; Dai, S. Enhanced CO_2/N_2 selectivity in amidoxime-modified porous carbon. *Carbon* **2014**, *67*, 457-464.

(22) Durá, G.; Budarin, V. L.; Castro-Osma, J. A.; Shuttleworth, P. S.; Quek, S. C.; Clark, J. H.; North, M. Importance of micropore–mesopore interfaces in carbon dioxide capture by carbon-based materials. *Angew. Chem. Int. Ed.* **2016**, *55*, 9173-9177.

(23) Simon, C. M.; Smit, B.; Haranczyk, M. Pyiast: Ideal adsorbed solution theory (IAST) python package. *Comput. Phys. Commun.* **2016**, *200*, 364-380.

Chapter 10. Prediction of Hydride Location in Copper Clusters by Deep Learning

10.1 Abstract

The location of hydrides in copper clusters is hard to be determined. Here, we present a rapid approach to help us predict the hydride location by deep learning. The input feature of this network only has the coordinates of "heavy atoms", which are accessible from single-crystal X-ray diffraction. Then, two copper clusters with undetermined hydride location were used to verify the predictive ability of this neural network.

10.2 Introduction

Since the first copper hydride CuH was reported in 1844 by Wirtz,[1] there is already a long time to study it. Recent years, with the advances in synthetic technology, a serial of copper hydride clusters have been presented.[2] And the research of their applications such as hydrogen storage and catalytic activity are also carrying out in full swing.[3-8] The hydrogen atoms as an important part of these copper clusters, heavily depend on neutron diffraction to determine their locations, and cannot be localized from common single-crystal X-ray diffraction (SXRD).[2] But sometimes growing a larger crystal (1 mm^3) suitable for neutron diffraction is hard to be successful for many novel copper hydride clusters, especially for those with complex structures.[9] For them, nowadays, people usually have to hypothesize the hydride locations according to their own chemical knowledge and experience. Then, to make verification, the hypothesized structures need to be optimized by density functional theory (DFT) calculation.[9-13] If the hydride locations are wrong, the whole cluster structures will collapse. If not, the hypothesized hydride locations might be reasonable. However, the making hypothesis process is always time-consuming because no one can guarantee success on their very first attempt. The hypothesis might be also not the most stable structure because of the possibility of energy local minimum. And the difficulty will even multiply with the increasing number of copper and hydrogen atoms. So, how to quickly and accurately locate all hydrides is still a challenge. Here, we describe a rapid and universal approach to predict the hydride locations in copper clusters by deep learning.

10.3 Computational Method

10.3.1 Rebuilding copper clusters in MATLAB

Firstly, the experimental cif files for all copper cluster crystals were download from CCDC database. They were imported into software Materials Studio. Secondly, a single cluster structure from each crystal was selected and put into a large box (25.5×25.5×25.5 Å^3), which is large enough for all collected clusters. Then, the coordinates of "heavy atoms" were used to rebuild the structures in MATLAB. The resolution was 0.1 Å, so the size of 3D image in MATLAB is 256×256×256. The size of atoms was Van der Waals radius, and the grey level of each atom was quadratically declined from the atom's center, which can help the network easily recognize the atom's position. Since there are seven different "heavy atoms": C, N, O, P, S, Se, Cu, seven channels were applied for each element, analogous to red, green, blue channels in color images. So, the size of rebuilt structures in MATLAB was 256×256×256×7.

10.3.2 Generation of input dataset

Because one cluster might have more than 1 hydride, above large boxes was further divided to many small boxes, which can make sure there is no more than one hydride in each small box. This process is shown in Figure S10-1. The size of small red boxes in each channel was 32×32×32, while a smaller green box (24×24×24) in the center of each red box was set to be predicted whether it possesses a hydride or not. The green boxes could help us pinpoint the hydride location more precisely and the red boxes could contain more surrounding information around a potential hydride location. The sampling step's length was equal to 24 to avoid omission or repetition.

10.3.3 Training 3D-CNN

Figure S10-2 shows the detailed architecture of 3D-CNN. It was created in MATLAB R2019b environment using the stochastic gradient descent with momentum (SGDM) optimizer. After each convolutional layer, there were one batch normalization layer to speed up training, one ReLU layer, and one average pooling layer to perform down-sampling. Two dropout layers with dropout probability 0.3 were used to avoid overfitting. The filter sizes of three convolutional layers were [3,3,3,7], [3,3,3,8], [3,3,3,16], the number of filters were 8, 16, 16, and the neuron numbers of three dense layers were 1024, 256, 2. During the training process, the parameters in convolutional filters as well as weights and biases were adjust to improve the performance. The maximum number of training epochs was 100. The initial learing rate was 0.01 and it was reduced by a factor 0.9 every epoch. The training data was shuffled before each training epoch.

10.3.4 Optimization of copper hydrides

The density functional theory (DTF) calculations were performed with the Vienna ab initio simulation package (VASP) to optimize the structures of copper hydride clusters.[26-28] The Perdew–Burke–Ernzerhof (PBE) form of the generalized-gradient approximation (GGA) was used for electron exchange and correlation.[29] The projector-augmented-wave (PAW) method[30] was used to describe the electron-core interaction with the cutoff energy of 450 eV for the planewave bases. To reduce computational cost, the outer groups like phenyl and tert-butyl were replaced by methyl. All atoms were allowed to relax.

10.4 Results and discussion

We collected 21 different copper clusters which have been determined exact hydride locations by neutron diffraction as benchmark.[14-25] The coordinates of “heavy atoms” (excluding hydrogen atom) in copper clusters which can be measured by SXRD were selected as the input. They were not directly delivered to the input layer but converted into 595 small three-dimensional images (or called boxes) as the input dataset. Because there are seven different “heavy atoms” among the collected copper clusters, seven input channels were created for each element. Then, a three-dimensional convolutional neural network (3D-CNN) was applied for classification, as shown in Figure 10-1 and Figure S10-2. In this network architecture, there are three convolutional layers to automatically extract features and three fully connected layers to classify input data to two classes: boxes with hydride or boxes without hydride.

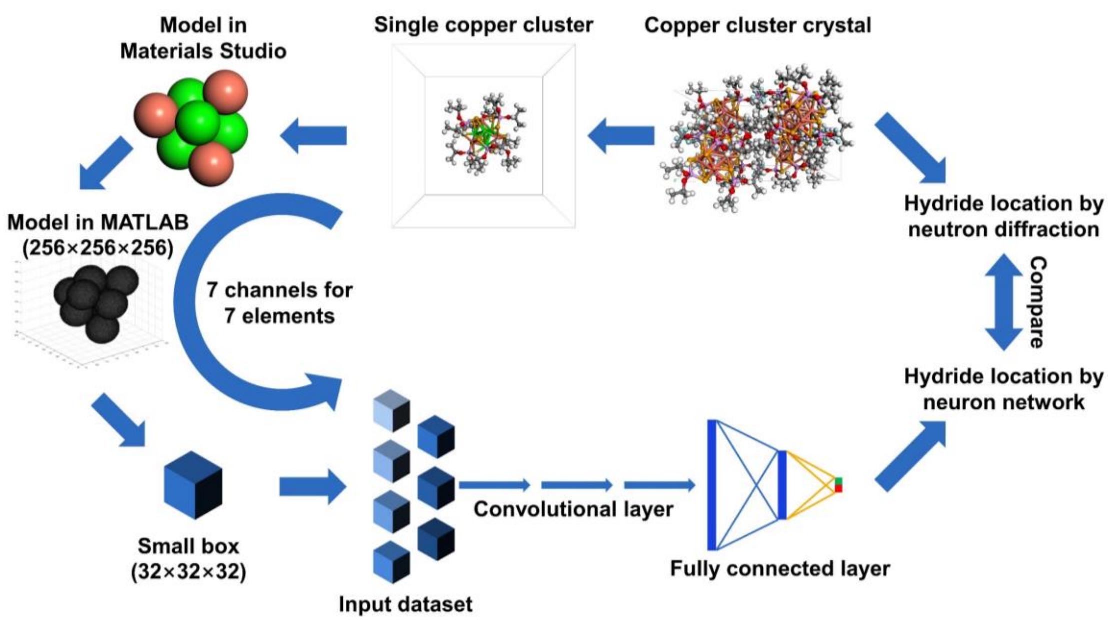

Figure 10-1. The process of generating input dataset and the sample architecture of 3D-CNN.

There are 85% input data as training set and 15% input data as validation set. The prediction results by 3D-CNN were compared with the benchmark from neutron diffraction in Figure 10-2a. The accuracies of 3D images with hydride and without hydride are both around 95%. The consistency of accuracy between training set and validation set indicates no overfitting.

Then, another two new copper hydride clusters without neutron diffraction measurement were used to proof the predictability of above well-trained 3D-CNN. The first example includes 25 copper atoms and 10 hydrides (Figure 10-2b).[12] Because it is not a very complicated structure, the hydride locations have been obtained by DFT calculation, shown in the third column of Figure 10-2d. Then, a serial of small boxes from the whole structure were put into the 3D-CNN, and the number of boxes with different probability of having hydride are shown in Figure 10-2c. They were approximatively divided into two sides, and just few boxes have an ambiguous probability. Then, we further considered the number of hydrides according to the experimental chemical formula $[Cu_{25}H_{10}(SPhCl_2)_{18}]^{3-}$, and preferentially paid attention to the boxes with higher probability of having hydride (Figure 10-2d). In the top 10, nine of them agree with the DFT results, while the last right location also ranks higher.

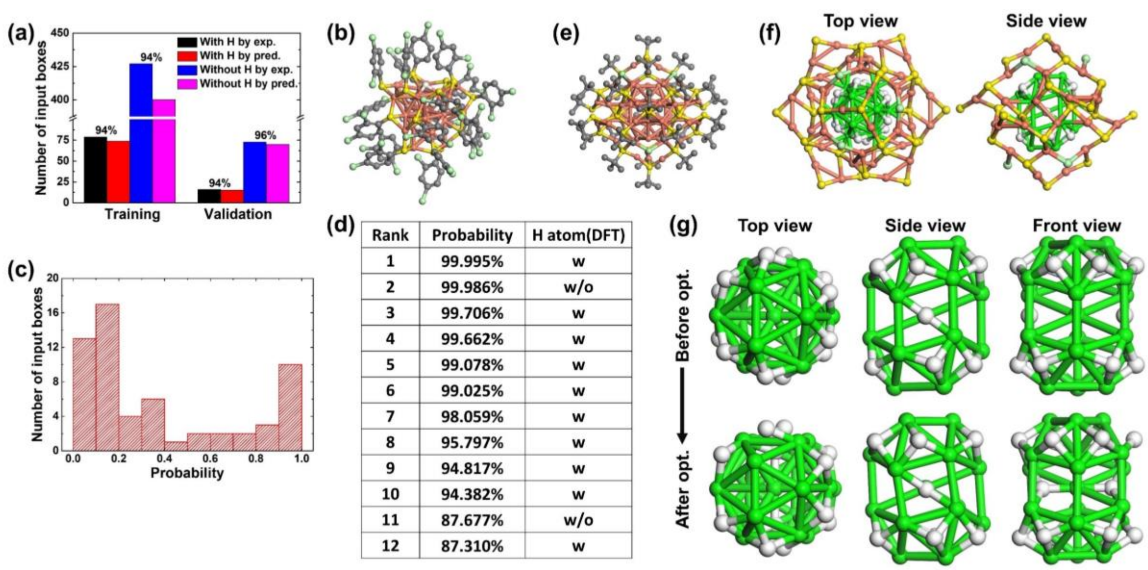

Figure 10-2. The prediction results of 3D-CNN. (a) The statistical number of input boxes with or without hydride according to the experimental neutron diffraction or the prediction of 3D-CNN. (b) The SXRD structure of $[Cu_{25}H_{10}(SPhCl_2)_{18}]^{3-}$. (c) The predicted probability distribution for the boxes extracted from $[Cu_{25}H_{10}(SPhCl_2)_{18}]^{3-}$. (d) The comparation between predicted and DFT calculated results. (e) The SXRD structure of $[Cu_{61}(StBu)_{26}S_6Cl_6H_{14}]^{+}$. (f) The top and side view of copper cluster part with predicted hydride locations. (g) The comparation between core copper hydride clusters before and after DFT optimization.

The second example is more complex including 61 copper atoms and 14 hydrides (Figure 10-2e),[13] so the hydride locations are still undetermined in experiment. But the XRD measurement has already been done, so the chemical formula $[Cu_{61}(StBu)_{26}S_6Cl_6H_{14}]^{+}$, the crystal symmetry, and the cluster structure without hydrogen atom could be obtained. The prediction process was similar to that for the first example. The XRD structure was divided to many small 3D boxes as input. Then, from high to low probability, and also considering the symmetry (space group C2/c),[13] 14 boxes were selected to possess a hydride, and the structure with 14 hydrides are shown in Figure 10-

2f. All hydrides are around the core copper cluster. Then, the whole structure was optimized by DFT calculation to check its stability. As shown in Figure 10-2g, the copper atoms have almost no change, and the hydrogen atoms are also fine-tuned slightly. The absence of collapse proves the structure's stability and the hydride location's reasonability. As comparation, several hydrides were moved to other locations, and the structure was also optimized in the same way. But this time a structure distortion was observed (Figure S10-5).

10.5 Summary and conclusions

In summary, we have trained a 3D-CNN from the experimental copper hydride clusters based on the coordinates of "heavy atoms". Then, the well-trained network successfully predicted hydride locations for two complicated copper clusters which cannot be measured by neutron diffraction in experiment. This deep learning approach can help researches rapidly pinpoint the hydride locations for increasing number of novel copper hydride clusters. Furthermore, the neural network is possible to be transferred for prediction of other metal clusters like silver hydride if enough clusters are reported in future.

References

(1) Wurtz, A. Sur l̀hydrure de. *Ann. Chim. Phys* **1844**, *11*, 250-251.

(2) Dhayal, R. S.; van Zyl, W. E.; Liu, C. Polyhydrido copper clusters: Synthetic advances, structural diversity, and nanocluster-to-nanoparticle conversion. *Acc. Chem. Res.* **2016**, *49*, 86-95.

(3) Dhayal, R. S.; van Zyl, W. E.; Liu, C. Copper hydride clusters in energy storage and conversion. *Dalton T.* **2019**, *48*, 3531-3538.

(4) Lee, B.-H.; Wu, C.-C.; Fang, X.; Liu, C.; Zhu, J.-L. $[Cu_8(\mu_4\text{-}H)\{S_2P(OEt)_2\}_6](PF_6)$: A novel catalytic hydride-centered copper cluster for azide-alkyne cycloaddtion. *Catal. Lett.* **2013**, *143*, 572-577.

(5) Zhang, M. M.; Dong, X. Y.; Wang, Z. Y.; Li, H. Y.; Li, S. J.; Zhao, X.; Zang, S. Q. Aie triggers the circularly polarized luminescence of atomically precise enantiomeric copper (i) alkynyl clusters. *Angew. Chem. Int. Ed.* **2019**.

(6) Jordan, A. J.; Lalic, G.; Sadighi, J. P. Coinage metal hydrides: Synthesis, characterization, and reactivity. *Chem. Rev.* **2016**, *116*, 8318-8372.

(7) Nakajima, T.; Kamiryo, Y.; Hachiken, K.; Nakamae, K.; Ura, Y.; Tanase, T. Tri- and tetranuclear copper hydride complexes supported by tetradentate phosphine ligands. *Inorg. Chem.* **2018**, *57*, 11005-11018.

(8) Pirnot, M. T.; Wang, Y. M.; Buchwald, S. L. Copper hydride catalyzed hydroamination of alkenes and alkynes. *Angew. Chem. Int. Ed.* **2016**, *55*, 48-57.

(9) Huertos, M. A.; Cano, I.; Bandeira, N. A.; Benet-Buchholz, J.; Bo, C.; van Leeuwen, P. W. Phosphinothiolates as ligands for polyhydrido copper nanoclusters. *Chem. Eur. J.* **2014**, *20*, 16121-16127.

(10) Nguyen, T. A. D.; Goldsmith, B. R.; Zaman, H. T.; Wu, G.; Peters, B.; Hayton, T. W. Synthesis and characterization of a Cu_{14} hydride cluster supported by neutral donor ligands. *Chem. Eur. J.* **2015**, *21*, 5341-5344.

(11) Nakajima, T.; Nakamae, K.; Hatano, R.; Imai, K.; Harada, M.; Ura, Y.; Tanase, T. Tetra-, hexa-and octanuclear copper hydride complexes supported by tridentate phosphine ligands. *Dalton T.* **2019**, *48*, 12050-12059.

(12) Sun, C.; Mammen, N.; Kaappa, S.; Yuan, P.; Deng, G.; Zhao, C.; Yan, J.; Malola, S.; Honkala, K.; Häkkinen, H. Atomically precise, thiolated copper–hydride nanoclusters as single-site hydrogenation catalysts for ketones in mild conditions. *ACS nano* **2019**, *13*, 5975-5986.

(13) Ghosh, A.; Huang, R.-W.; Alamer, B.; Abou-Hamad, E.; Hedhili, M. N.; Mohammed, O. F.; Bakr, O. M. $[Cu_{61}(S^tBu)_{26}S_6Cl_6H_{14}]^+$: A core–shell superatom nanocluster with a Quasi-J_{36} Cu_{19} core and an "18-crown-6" metal-sulfide-like stabilizing belt. *ACS Mater. Lett.* **2019**, *1*, 297-302.

(14) Liu, C.; Sarkar, B.; Huang, Y.-J.; Liao, P.-K.; Wang, J.-C.; Saillard, J.-Y.; Kahlal, S. Octanuclear copper (i) clusters inscribed in a Se_{12} icosahedron: Anion-induced modulation of the core size and symmetry. *J. Am. Chem. Soc.* **2009**, *131*, 11222-11233.

(15) Liao, P.-K.; Sarkar, B.; Chang, H.-W.; Wang, J.-C.; Liu, C. Facile entrapment of a hydride inside the tetracapped tetrahedral Cu^{I}_{8} cage inscribed in a S_{12} icosahedral framework. *Inorg. Chem.* **2009**, *48*, 4089-4097.

(16) Liao, P.-K.; Liu, K.-G.; Fang, C.-S.; Liu, C.; Fackler Jr, J. P.; Wu, Y.-Y. A copper (i) homocubane collapses to a tetracapped tetrahedron upon hydride insertion. *Inorg. Chem.* **2011**, *50*, 8410-8417.

(17) Liao, P.-K.; Fang, C.-S.; Edwards, A. J.; Kahlal, S.; Saillard, J.-Y.; Liu, C. Hydrido copper clusters supported by dithiocarbamates: Oxidative hydride removal and neutron diffraction analysis of [Cu7(H){S_2C(aza-15-crown-5)}$_6$]. *Inorg. Chem.* **2012**, *51*, 6577-6591.

(18) Latouche, C.; Kahlal, S.; Lin, Y.-R.; Liao, J.-H.; Furet, E.; Liu, C.; Saillard, J.-Y. Anion encapsulation and geometric changes in hepta-and hexanuclear copper (i) dichalcogeno clusters: A theoretical and experimental investigation. *Inorg. Chem.* **2013**, *52*, 13253-13262.

(19) Dhayal, R. S.; Liao, J.-H.; Hou, H.-N.; Ervilita, R.; Liao, P.-K.; Liu, C. Copper (i) diselenocarbamate clusters: Synthesis, structures and single-source precursors for Cu and Se composite materials. *Dalton T.* **2015**, *44*, 5898-5908.

(20) Liao, J.-H.; Dhayal, R. S.; Wang, X.; Kahlal, S.; Saillard, J.-Y.; Liu, C. Neutron diffraction studies of a four-coordinated hydride in near square-planar geometry. *Inorg. Chem.* **2014**, *53*, 11140-11145.

(21) Edwards, A. J.; Dhayal, R. S.; Liao, P. K.; Liao, J. H.; Chiang, M. H.; Piltz, R. O.; Kahlal, S.; Saillard, J. Y.; Liu, C. Chinese puzzle molecule: A 15 hydride, 28 copper atom nanoball. *Angew. Chem. Int. Ed.* **2014**, *53*, 7214-7218.

(22) Dhayal, R. S.; Liao, J. H.; Kahlal, S.; Wang, X.; Liu, Y. C.; Chiang, M. H.; van Zyl, W. E.; Saillard, J. Y.; Liu, C. [$Cu_{32}(H)_{20}\{S_2P(OiPr)_2\}_{12}$]: The largest number of hydrides recorded in a molecular nanocluster by neutron diffraction. *Chem. Eur. J.* **2015**, *21*, 8369-8374.

(23) Dhayal, R. S.; Liao, J. H.; Wang, X.; Liu, Y. C.; Chiang, M. H.; Kahlal, S.; Saillard, J. Y.; Liu, C. Diselenophosphate-induced conversion of an achiral [$Cu_{20}H_{11}\{S_2P(OiPr)_2\}_9$] into a chiral [$Cu_{20}H_{11}\{Se_2P(OiPr)_2\}_9$] polyhydrido nanocluster. *Angew. Chem. Int. Ed.* **2015**, *54*, 13604-13608.

(24) Stevens, R. C.; McLean, M. R.; Bau, R.; Koetzle, T. F. Neutron diffraction structure analysis of a hexanuclear copper hydrido complex, $H_6Cu_6[P(p\text{-tolyl})_3]_6$: An unexpected finding. *J. Am. Chem. Soc.* **1989**, *111*, 3472-3473.

(25) Lemmen, T. H.; Folting, K.; Huffman, J. C.; Caulton, K. G. Copper polyhydrides. *J. Am. Chem. Soc.* **1985**, *107*, 7774-7775.

(26) Román-Pérez, G.; Soler, J. M. Efficient implementation of a van der waals density functional: Application to double-wall carbon nanotubes. *Phys. Rev. Lett.* **2009**, *103*, 096102.

(27) Kresse, G.; Furthmüller, J. Efficient iterative schemes for ab initio total-energy calculations using a plane-wave basis set. *Phys. Rev. B* **1996**, *54*, 11169.

(28) Klimeš, J.; Bowler, D. R.; Michaelides, A. Van der waals density functionals applied to solids. *Phys. Rev. B* **2011**, *83*, 195131.

(29) Perdew, J. P.; Burke, K.; Ernzerhof, M. Generalized gradient approximation made simple. *Phys. Rev. Lett.* **1996**, *77*, 3865.

(30) Blöchl, P. E. Projector augmented-wave method. *Phys. Rev. B* **1994**, *50*, 17953.

Supporting information

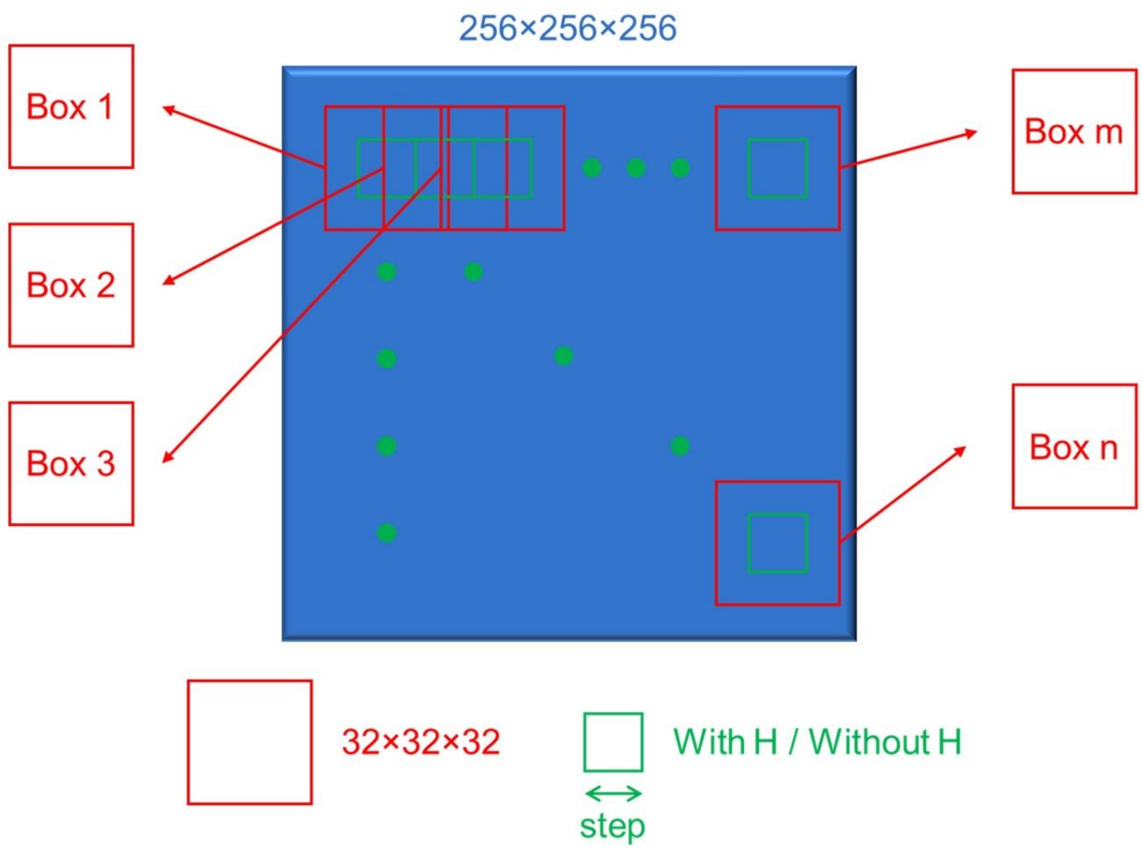

Figure S10-1. The process of generating input dataset.

The large blue box (256×256×256) contained the copper hydride cluster. The middle red boxes, which included enough information around a potential hydride location, formed the input dataset. The 3D-CNN would predict whether there is a hydride in each small green box or not.

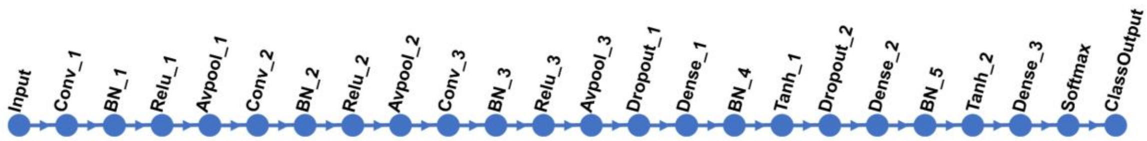

Figure S10-2. The detailed architecture of 3D-CNN.

The layer names represent different types of layer. “Input”: 3D image input layer; “Conv”: 3D convolutional layer; “BN”: batch normalization layer; “Relu”: ReLU layer; “Avpool”: average pooling layer; “Dropout”: dropout layer; “Dense”: fully connected layer; “Tanh”: hyperbolic tangent activation layer; “Softmax”: softmax layer; “ClassOutput”: classification layer.

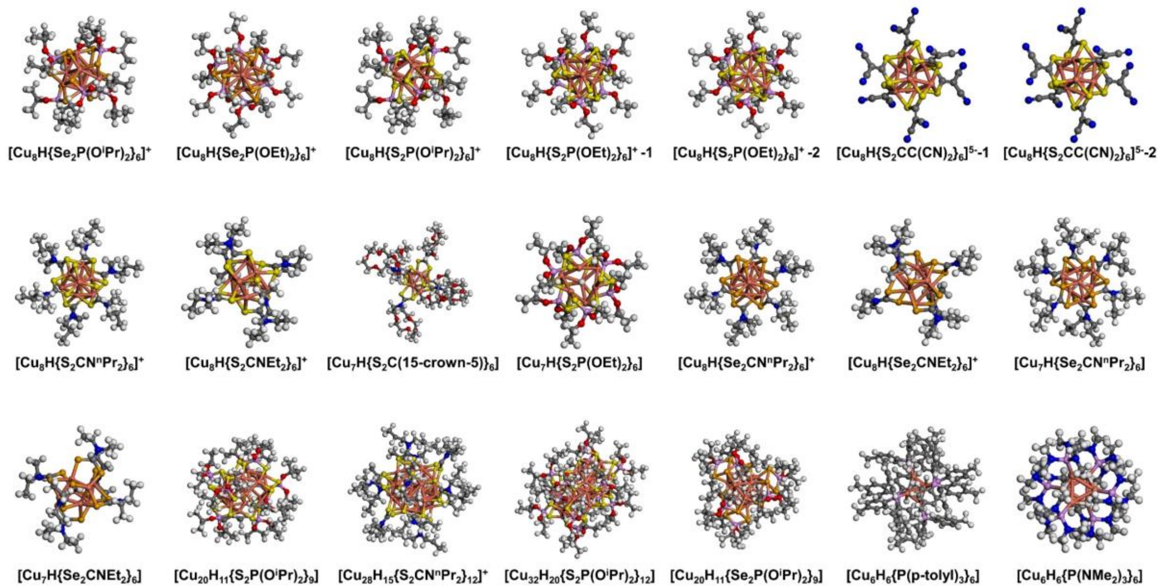

Figure S10-3. The structures and chemical formulas of 21 copper hydride clusters for training 3D-CNN.

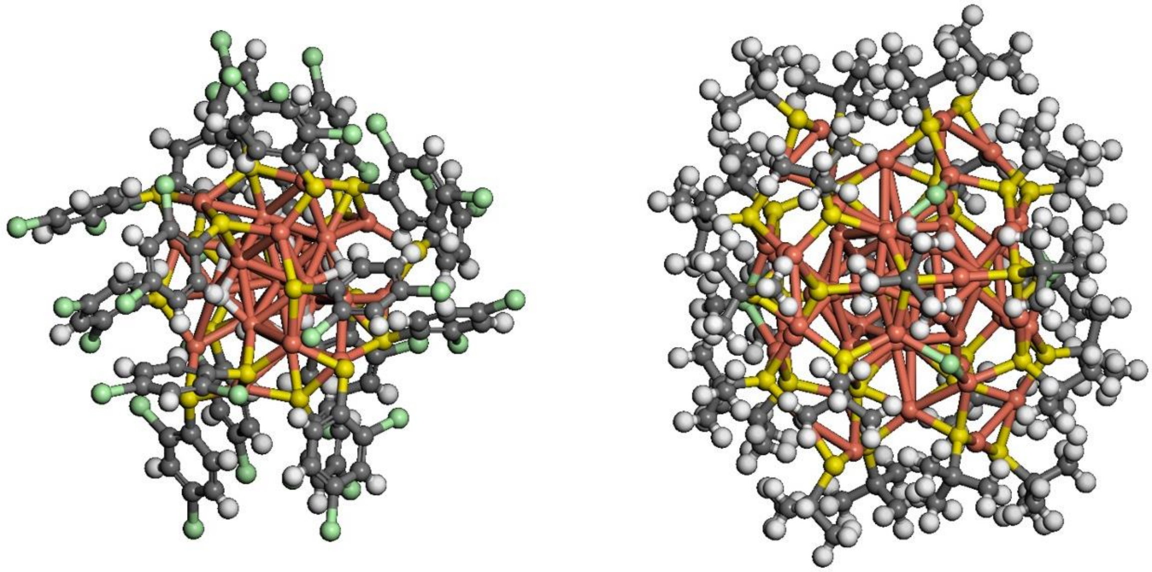

$[Cu_{25}H_{10}(SPhCl_2)_{18}]^{3-}$ $[Cu_{61}(StBu)_{26}S_6Cl_6H_{14}]^{+}$

Figure S10-4. The structures and chemical of 2 copper hydride clusters for checking predictability of 3D-CNN.

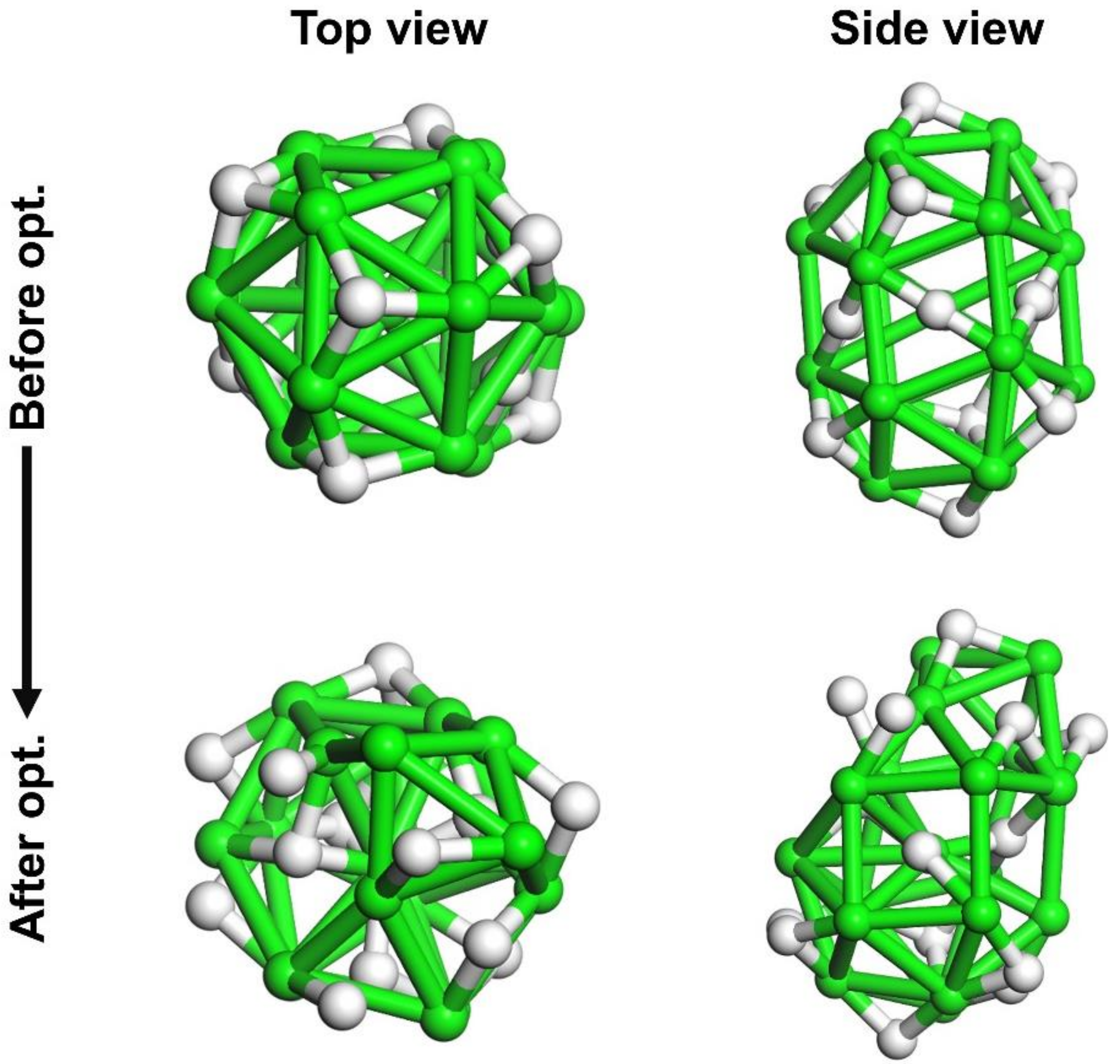

Figure S10-5. The comparation between core copper hydride clusters with unreasonable hydride locations before and after DFT optimization.

Chapter 11. Summary and Outlook

In this dissertation, we studied the ultrathin nanoporous materials for gas separation by using different computational approaches including DFT, GCMC, CMD, and machine learning. The effect of several factors has been studied, such as pore size, pore density, pore shape, surface area, et al.

In Chapter 3, we studied the pore-size effect on CO_2 uptake and CO_2/N_2 selectivity according to the overlap of potential energy surface of gas molecules in carbon nanotubes. GCMC simulations were applied to quantify the values of uptake and selectivity. We found that cylindrical pores of 7 to 8 Å (or accessible pores of 3.4 to 4.4 Å) in size are promising for post-combustion CO_2 capture.

In Chapter 4, we studied another important factor pore density dictating gas separations through ultrathin nanoporous membranes. By CMD simulations, we found that higher pore density would yield higher permeation rate for gas molecules. We also found that for weakly adsorbing gas such as He, its permeation is dominated by direct flux. In contrast, for strongly adsorbing gas such as CO_2, its permeation is dominated by surface flux. This work suggested that making the membranes asymmetric by creating dissimilar surfaces could lead to more interesting permeation and separation behaviors.

In Chapter 5 and 6, we presented a design of bilayer nanoporous graphene membranes to continuously tune the effective pore size. With suitable effective pore size, high selectivities of CO_2/CH_4, N_2/CH_4, and O_2/N_2 can be achieved, while CO_2, N_2, and O_2 permeances remain on the order of 10^5 GPU. By tracking trajectories of gas molecules, we found extra tumbling motion of gas molecule through the elliptical-shaped pore would yield high entropic selectivity. This design can be also extended to more membranes with larger pore size. These works suggested a promising direction to tune the effective pore size for selective gas separation.

In Chapter 7, we presented another design to tune pore size through combination of graphene and ionic liquid. The layer-by-layer graphene/ILs composite materials were optimized by DFT calculation. Then, they were simulated by GCMC to calculate their $CO_2/N_2/CH_4$ adsorption capacities and selectivities at experimental conditions. This work shows an easily way to tune slit pore size for high selective carbon capture.

In Chapter 8 and 9, we presented how to use machine learning to rapidly predict the uptakes and selectivities for large numbers of porous carbon material. In Chapter 8, we chose micropore volume, mesopore volume, and BET surface area as input features. Further, in Chapter 9, we chose N_2 adsorption isotherm at 77 K, which is an ultimate input feature. By exploring hypothetical porous carbons space, we found the best features for high CO_2 uptake are not the same with the best features for CO_2/N_2 selectivity. Focusing on the lowest N2-uptake regions is a better strategy. The region should have bimodal distributions of well-separated micropores (< 2 nm) and mesopores (3 – 7 nm).

In Chapter 10, we extended the application of deep learning to predict the location of hydrides in copper clusters. This work presented how to transfer crystal structures of copper cluster to a serial of 3D images as input dataset and how to train a 3D-CNN model to predict the hydride location. The accuracy of this model was proved by DFT calculation for two complicated copper clusters whose hydride locations have not been measured by neutron diffraction in experiment. This work provides a useful tool to rapidly pinpoint the hydride locations in novel copper clusters, even in other metal clusters by transfer learning in future.

In conclusion, we have studied various factors which are relevant to gas separation via ultrathin membrane materials by several computational methods. Our works are important for exploring novel materials for different gas separation systems. However, with the increasing numbers of new materials, there is still room for further research in this area. First, beside carbon based membrane materials, which are mainly considered in this dissertation, there are many other 2D porous materials which are promising for forming gas separation membranes. They need more researches in future. Second, some functional groups like nitrogen, oxygen, and fluorine are significantly influence the separation ability of membrane materials. The effects of them need more studies. Third, this dissertation only considered physisorption. Chemisorption is another important branch. Many ionic liquids belong to this aspect. Reactive force fields need to be developed for them for molecular dynamics simulations. Fourth, traditional computational methods like DFT and CMD are usually time-consuming. For exploring large material database to find novel membrane materials for gas separation, high throughput methods will be more and more important. As one of these methods, machine learning applications in chemical area are still limited. In future, machine learning will be benefit for every aspect of chemistry.